

**A FORCE-MEDIATED CONFORMATIONAL CHANGE IN
FIBRONECTIN'S INTEGRIN BINDING DOMAIN IS
ASSOCIATED WITH FIBROTIC REMODELING AND
DRIVES FIBROBLAST ACTIVATION**

A Thesis
Presented to
The Academic Faculty

By

Leandro Moretti

In Partial Fulfillment
of the Requirements for the Degree
Doctorate of Philosophy in
Biomedical Engineering

University of Virginia
June 2021

COPYRIGHT© 2021 BY LEANDRO MORETTI

**A FORCE-MEDIATED CONFORMATIONAL CHANGE IN
FIBRONECTIN'S INTEGRIN BINDING DOMAIN IS
ASSOCIATED WITH FIBROTIC REMODELING AND
DRIVES FIBROBLAST ACTIVATION**

Approved by:

Dr. Brent French, Chair
Department of Biomedical Engineering
University of Virginia

Dr. Thomas Barker, Advisor
Department of Biomedical Engineering
University of Virginia

Dr. James Hagood
Department of Pulmonology
University of North Carolina

Dr. Kristen Naegle
Department of Biomedical Engineering
University of Virginia

Dr. James Casanova
Department of Cell Biology
University of Virginia

Date Approved:

“Le brutte intenzioni la maleducazione,
La tua brutta figura di ieri sera,
La tua ingratitudine, la tua ignoranza,
Fai ciò che vuoi mettendo i piedi in testa!
Certo il disordine è una forma d’arte,
ma tu sai solo coltivare invidia!
Ringrazia il cielo sei su questo palco,
Rispetta chi ti ci ha portato dentro.”

Morgan, Sanremo February 2020

ACKNOWLEDGEMENTS

I would like to acknowledge the numerous people who welcomed and supported me during my time at the University of Virginia. First and foremost, I would like to thank my advisor Dr. Thomas Barker, for choosing me as his next student almost 6 years ago, and for believing in me so much that he uprooted me from Atlanta to keep me at his side. His guidance and (cautious) optimism made even the longest working hours enjoyable. I would also like to thank Drs. Brent French, Kristen Naegle, Jim Hagood, and Jim Casanova for not only agreeing to be part of my committee without hesitation, but also for being flexible and understanding as circumstances evolved.

I am thankful for Kim Fitzhugh-Higgins, who helped me navigate the complexity of the PhD program requirements. The accomplishments reported here could not have been possible without the scientific and moral support of Barker lab members, past and present. Dr. Dwight Chambers has been an incredible mentor in matters inside and outside the lab. Dr. Vicky Stefanelli has been the model of work ethic I try to replicate. Dr. Riley Hannan has endured the ups and downs of grad school with me, while trading technical advice when needed. Drew Miller was a most welcome addition to the group, enabling new methods and keeping the whole enterprise down-to-earth. Sue Landes and Dr. Vincent Yeh, who made all the mice studies in here happen. I must also acknowledge the parallel effort of Dr. Wei Li that will lead to my first high impact publication. Overall, they all contributed to a productive but light hearted work environment, a rare finding from which I benefitted greatly and will miss moving forward.

Grad students shall not live by experiments alone, but by divertissement as well. I want to thank the D&D™ crew, Lee Talman, Riley Hannan, Anthony Bruce, and Chris Waters, for providing the right dose of fun and escapism during all these years.

I would also like to thank my best friend Matteo Diddi, who keeps cheering me on even if separated by miles of land and ocean. I am especially grateful for my girlfriend, Amber Goad, and her beloved dog Kai, who have been my emotional support throughout this uncertain time, helping me overcome bumps and larger obstacles along the road with kindness, tenderness and unconditional love. It is now time to reap the fruits of all that labor.

Last but not least, I would like to acknowledge my family, who never doubted my ability to succeed. I have been fortunate to have parents willing to make sacrifices in order for me to achieve the best possible future, even if at the cost of proximity. Without love and support in their own ways, I would not have all of my successes.

TABLE OF CONTENTS

ACKNOWLEDGEMENTS	iv
LIST OF TABLES	ix
LIST OF FIGURES	x
LIST OF ABBREVIATIONS	xi
SUMMARY	xiii
CHAPTER 1	1
INTRODUCTION	1
IDIOPATHIC PULMONARY FIBROSIS AND USUAL INTERSTITIAL PNEUMONIA.....	1
Glutathionylation in lung cancer and disease	7
Remodeling by fibroblasts	8
RELEVANCY OF FIBRONECTIN CONFORMATION.....	9
INTEGRINS BINDING FIBRONECTIN	12
$\alpha v\beta 3$ and $\alpha 5\beta 1$	14
$\alpha 4\beta 1$ and $\alpha 9\beta 1$	15
MYOFIBROBLASTIC MARKERS	16
Integrins of (Myo)Fibroblasts	18
$\alpha 1\beta 1$, $\alpha 2\beta 1$, and $\alpha 11\beta 1$	19
HYPOTHESIS AND SUMMARY.....	21
CHAPTER 2	23
IN VIVO DETECTION AND BIOLOGICAL RELEVANCE OF THE INTEGRIN SWITCH	23
INTRODUCTION	23
EXPERIMENTAL SETUP.....	26
Bleomycin model	27
Inducible model of integrin $\alpha 5$ knock out	29
Naïve mouse lung fibroblasts	29
Functionalizing glass with Fn fragments.....	30
Single cell Force Spectroscopy	30
Luminex assay	32
Mass spectroscopy of the adhesome.....	33
Functionalizing soft PDMS gels with Fn fragments.....	34

RNAseq experiment.....	35
RESULTS	38
The Fn Integrin Switch is activated and detectable in in vivo models of lung fibrosis.....	38
Fibroblasts develop lower adhesion forces on the activated Integrin Switch due to predominant integrin $\alpha v \beta 3$ engagement.....	42
The activated Integrin Switch promotes cytosolic protein signaling and clustering that enhance proliferation, survival, and secretory pathways within 30 minutes.....	45
Transcriptome of fibroblasts engaging the activated Integrin Switch significantly diverges from baseline at 24 hours	50
DISCUSSION	54
FIGURES	59
CHAPTER 3	77
POST TRANSLATIONAL MODIFICATIONS' ROLE IN PRIMING THE INTEGRIN SWITCH IN HUMAN LUNG DISEASES	77
INTRODUCTION	77
EXPERIMENTAL SETUP.....	79
Cell culture.....	79
Single fiber deposition and decellularized matrix formation	79
AFM manipulation.....	80
Immunofluorescence imaging	81
Human Tissue Staining	83
Mutant Fibronectin.....	84
RESULTS AND DISCUSSION.....	85
CONCLUSION.....	99
CHAPTER 4	100
IMPACT AND FUTURE DIRECTIONS	100
APPENDIX A: SUPPLEMENTAL DATA.....	107
Adhesome Data.....	107
RNAseq Data	109
APPENDIX B: PROTOCOLS.....	115
ANTIBODY PRODUCTION.....	115
Day 1.....	115
Day 2.....	115
Day 3.....	115

Buffers	115
Setting up the HPLC	116
NAÏVE MOUSE LUNG FIBROBLASTS	119
Harvesting mouse lungs	119
Preparation of cell stocks:	120
Excellness Plate preparation.....	120
Making cells naïve again.....	120
Functionalizing glass (or silica) with fibronectin fragments	122
Materials:	122
Functionalizing the glass (inside a chemical hood)	122
Reducing dimers in Fn fragments (start along with the next section to try and sync the incubations).....	122
Maleimide activation of the modified surface	123
Crosslink fragments to activated surface	123
CHAPTER 5	125
REFERENCES	125

LIST OF TABLES

Table 1: Names and sequences of DNA primers used for genotyping	29
Table 2: Experimental conditions for Luminex Cell Signaling assay	32
Table 3: submitted RNAseq samples.....	36
Table 4: Lists of transcription factors predicted to explain DEGs in our RNAseq experiment.	53

LIST OF FIGURES

Figure 1: Tomography scan showing classic features of IPF.	2
Figure 2: Classification of ILDs.	3
Figure 3: Pentachrome (Movat) -stained section.....	5
Figure 4: Structure of fibronectin	9
Figure 5: Cartoon showing the structure of one Fibronectin monomer.....	13
Figure 6: Fn integrin switch activation is detected by scFv and it correlates with lung fibrosis in vivo.	59
Figure 7: Integrin Switch activation favors $\alpha v \beta 3$ engagement and lowers attachment forces, below 2 minutes.	62
Figure 8: The Integrin Switch upregulates proliferation, survival, and secretory pathways within 30 minutes.....	64
Figure 9: Activated Integrin Switch substrates upregulate mesenchymal genes at 24 h. .	66
Figure 10: Normalized blood distribution for E3 (FnEDA) and H5 scFvs.....	67
Figure 11: Loss of integrin alpha5, equivalently to activation of the Integrin Switch, significantly increases lung fibrosis mortality.	69
Figure 12: Fn 9-4G-10III reduces $\alpha 5 \beta 1$ integrin mediated spreading of fibroblasts compared to Fn 9*10III	71
Figure 13: Adhesion strengthening dynamics of pKO- $\beta 1$ and pKO- αV or pKO- $\alpha V / \beta 1$ and pKO fibroblasts to Fn 9-4G-10III or Fn 9*10III.	72
Figure 14: KEGG pathway map of Akt populated with Luminex data at 30 minutes.....	74
Figure 15: Bulk RNAseq heat maps for 4G/9*10 and 50:50/9*10 (data from Fig. 4)	76
Figure 16: Crystal structure of fibronectin type III 7th – 10th repeat.....	78
Figure 17: Schematic setup and bright field image of AFM tip pulling on single fibronectin fiber.	80
Figure 18: Stress-strain plot shows glutathionylated fibronectin fibers	85
Figure 19: Cryptic cysteines in the 7 th and 15 th type III repeats are essential for glutathionylation impacts on fiber modulus.	87
Figure 20: Glutathionylated fibers are less stiff, a property not recovered	88
Figure 21: Cryptic cysteines in the 7 th and 15 th type III repeats are essential for glutathionylation impacts on fiber elasticity.....	90
Figure 22: Glutathionylation of Fn lowers the force threshold necessary to unfold the IBD and cause the integrin switch (cartoon).	93
Figure 23: Glutathionylation of Fn lowers the stress (force) threshold.....	94
Figure 24: Glutathionylation of dECM enables integrin switch activation.	95
Figure 25: Step by step image analysis performed by ratiometric algorithm.	96
Figure 26: Glutathionylation of Fn is significantly increased	98

LIST OF ABBREVIATIONS

10III	fibronectin 10th type III repeat
15III	fibronectin 15th type III repeat
7III	fibronectin 7th type III repeat
9III	fibronectin 9th type III repeat
AFM	atomic force microscopy
APTES	3-Aminopropyltriethoxysilane
DMEM	Dulbecco's modified Eagle's medium
ECM	extra cellular matrix
ELISA	enzyme-linked immunosorbent assay
FBS	fetal bovine serum
Fn	fibronectin
FTY720	fingolimod
GluFn	glutathionylated fibronectin
GSH	reduced glutathione
GSSG	dimerized and oxidized glutathione
IBD	integrin binding domain
IntSw	integrin switch
IPF	idiopathic pulmonary fibrosis
KEGG	Kyoto Encyclopedia of Genes and Genomes
MLF	mouse lung fibroblast
mRNA	messenger ribonucleic acid
MS	mass spectroscopy

PBS/T	phosphate buffer saline / with Tween20
PCR	polymerase chain reaction
PDMS	polydimethylsiloxane
PelB	pectate lyase B of <i>Erwinia carotovora</i>
PTM	post-translational modification
RGD	arginine, glycine, aspartic acid
RNAseq	ribonucleic acid sequencing
scFS	single-cell force spectroscopy
scFv	single chain variable fragment
Sulfo-SMCC	sulfosuccinimidyl-4-(N-maleimidomethyl)cyclohexane-1-carboxylate
TCEP	tris(2-carboxyethyl)phosphine
TGF β	transforming growth factor beta
UIP	usual interstitial pneumonia

SUMMARY

Fibronectin (Fn) is a major component of the extracellular matrix during homeostatic conditions, wound healing, and is enriched in diseases like pulmonary fibrosis and cancer. Fn provides binding for growth factors and cells' physical tethers, integrins. It has been theorized that small, cell-generated forces unfold Fn's integrin binding domain (IBD). Fibroblasts, the effectors of fibrosis, express integrins $\alpha\beta3$ and $\alpha5\beta1$, that is susceptible to the IBD switching between the regular and unfolded state. Specifically, integrin $\alpha5\beta1$ requires the physiological, folded (closed) conformation of Fn's IBD, while $\alpha\beta3$ can also bind the unfolded, open conformation. Since increased $\alpha\beta3$ signaling has been associated with fibrosis, further understanding the downstream effects of this differential integrin binding could elucidate several unresolved diseases' mechanisms. We hypothesized that this change in Fn conformation affects lung fibroblasts by guiding integrin enrichment, pushing them towards a secretory and pro-fibrotic phenotype.

What follows is the recollection of a multi-pronged attempt to first find the Integrin Switch (IntSw) in mouse models of lung fibrosis *in vivo*. I rediscovered an antibody that can target the Fn IBD, with increased specificity towards its unfolded, pathologically associated conformation where it outcompetes integrin $\alpha\beta3$. The antibody was labelled with VivoTag dyes and used to first monitor lung fibrosis development in live mice that received intratracheal bleomycin after 2 weeks. I also developed a novel triple-transgenic mouse line in order to test whether affecting the IntSw by conditionally knocking out the other integrin involved, $\alpha5\beta1$, aggravates lung fibrosis.

In my single cell force spectroscopy experiments I observed that $\alpha 5\beta 1$ engagement was needed to generate high adhesion forces even at short time points (<120s), in accordance with previous literature. Luminex analysis highlighted increased activity in Rac, Akt pathways over Ras signaling for fibroblasts seeded on the open IBD conformation fragment. My mass spectroscopy work indicated that pro-fibrotic pathways and, particularly, collagen XIIa, Integrin-Linked Kinase, Rap1B, and tubulin beta3 appeared to be enriched upon increased $\alpha \nu \beta 3$ binding at 30'.

After culturing for 24h on soft substrates (5 kPa representing healthy lung tissue), lung fibroblasts plated on the open IBD Fn fragment predominantly engaged $\alpha \nu \beta 3$ and displayed increased nuclear translocation of transcription factors associated with a secretory and contractile phenotype. More than 9000 genes with significantly different expression were discovered by bulk RNAseq assays with fibroblasts seeded on the open Fn fragment, compared to the closed fragment.

In conclusion, these data support that differential integrin engagement due to Fn IBD unfolding appears to affect cell phenotype in both the short and long run. This work contributes to understanding the link between changes in the ECM and cell behavior in the context of fibroproliferative diseases.

CHAPTER 1

INTRODUCTION

IDIOPATHIC PULMONARY FIBROSIS AND USUAL INTERSTITIAL PNEUMONIA

Respiration at the pulmonary stage is enabled gas exchange taking place in the alveoli. These sacs are inflated by air of different composition from the one surrounding our bodies, and are surrounded in turn a network of capillary blood vessels. Driven by concentration gradients, carbon dioxide in oxygen-poor venous blood diffuses towards the air and the environment, while oxygen diffuses in, to be distributed by blood towards peripheral tissues. Diffusion takes place across the blood-air barrier, which can be as thin as 0.4 microns¹ and made up by the membrane of the capillary endothelium, the basement membrane of the epithelial cells and the latter cells themselves. Impaired gas exchange becomes a self-evident consequence of increased blood-air barrier thickness, whether it is momentary or due to a disease. Pathologies affecting the blood-air barrier and the space surrounding the alveoli are categorized as Interstitial Lung Disease (ILD), sharing many of their symptoms and presentation.

Within ILDs, the most common form is called Idiopathic Pulmonary Fibrosis (IPF)². According to Olson and Sprunger, as of 2012 this lungs disease has a prevalence of 125.2 per 100,000 people³ in the United States alone, which will increase due to the progressive aging of the population. The disease typically affects older people, preferentially male (1.5 to 1 ratio with females), with 66 being the median age of diagnosis ⁴. IPF is a scarring, progressive pathology with a 5-

year survival rate of 20% ⁵. Early symptoms of the disease include breathlessness upon exertion and dry cough that interferes with the patient's daily activities ⁶. Given the patient's age, these traits are often attributed to aging or other syndromes, thus delaying the diagnosis. Clinically, IPF is characterized by inspiratory crackles during auscultation, often along with clubbing. Patients also suffer from decreased forced vital capacity and forced expiratory volume, coupled with impaired gas exchange, which can be demonstrated by measuring the diffusion capacity ⁶.



Figure 1: Tomography scan showing classic features of IPF. Arrowheads illustrate honeycomb structural changes, while arrow shows traction bronchiectasis. ⁶

Guidelines for diagnosis from the American Thoracic and European Respiratory Societies (ATS/ERS) recommend a combined clinical exam plus high-resolution computer tomography. Unless the scan returns a pattern of Usual Interstitial Pneumonia (UIP), an additional surgical lung biopsy is recommended⁷.

UIP is not only a detectable computer tomography pattern, but also a histological one. Typical patterns of fibrosis visible through high resolution computer tomography consist of evident bilateral, peripheral and subpleural reticular infiltrates. Often, the presence of advanced fibrosis is indicated by honeycomb changes and traction bronchiectasis⁶, as shown in Figure 1.

Potential etiologies for histologic UIP include systemic autoimmune/connective tissue diseases, familial pulmonary fibrosis, pneumoconiosis (e.g., asbestosis), fibrotic phase of chronic hypersensitivity

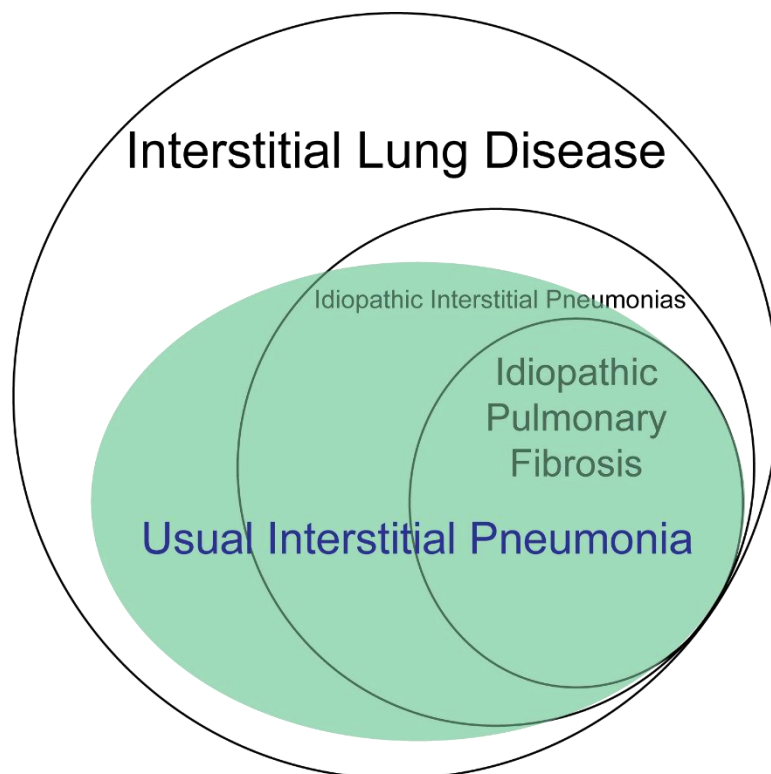


Figure 2: Classification of ILDs. The set of diseases characterized by the histological pattern of UIP is in green. Adapted from Huie and Frankel³

pneumonitis, and possible drug toxicity. All must be clinically excluded before diagnosing IPF in a patient with histologic UIP³. Thus, UIP is a histological pattern more widespread than merely IPF, suggesting that the characteristics about to be described may have a mechanistic impact in a panoply of ILDs, as depicted in Figure 2.

In tomography-detected patterns of probable, indeterminate, or alternative UIP⁷, lung biopsies allow detection of histopathological lesions and structures like fibroblastic foci, which are pale-staining whirls of loose extracellular matrix molecules (ECM, a.k.a. ‘the matrix’), interspersed with numerous fibroblasts ⁶. The latter cells typically contribute to wound repair, but in UIP they contribute to the spatial heterogeneity of the disease because they remodel the pulmonary interstitial tissue architecture, as shown in Figure 3 ³.

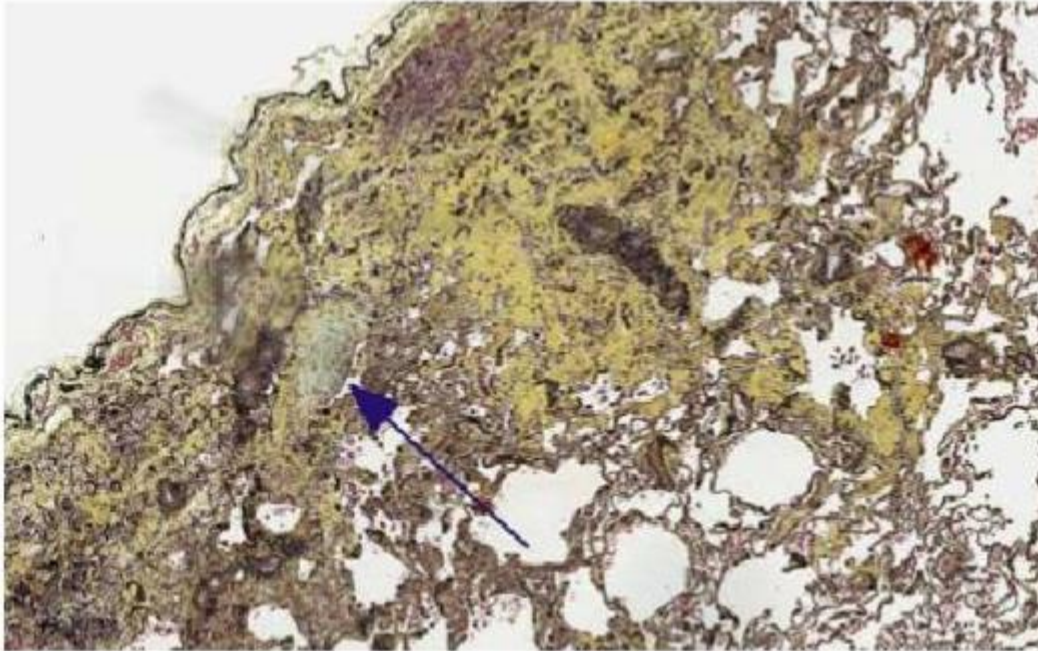


Figure 3: Pentachrome (Movat) -stained section, showing morphological heterogeneity and a fibroblastic focus in green (arrow)

The yellow features and portions in Figure 3 are ECM proteins excessively and uncontrollably secreted by fibroblasts. ECM proteins have highly important functions in physiological conditions, thus it is an appropriate moment to describe them in depth, along with their interplay with oxidative stress and reactive oxygen species, which do have a role in UIP as well.

ECM is the three-dimensional polymeric network of macromolecules essential for all multicellular organisms existing outside of cells. It supports their attachment, organization, and functions within tissues. The ECM not only provides physical scaffolding for cells, but it also acts as a complex biochemical and biophysical stimulus; it represents a complex, fundamental mechanism regulating cellular behavior and phenotype⁸. ECM not only directly binds cells through integrin receptors, it orchestrates the action of a host of growth factors and

cytokines by their selective, local accumulation and release. The critical importance of ECM is best demonstrated by the fact that selected removal of many ECM components at the genetic level leads to the loss of life at some of the earliest developmental stages^{9,10}.

ECM is also highly dynamic. When an injury occurs, specific ECM proteins, such as fibronectin, are secreted and assembled into a fibrillar ‘provisional matrix’ that acts as a potent biochemical and biophysical stimulator of tissue remodeling. This matrix promotes new blood vessel formation and instructs immune cell and fibroblast responses¹¹. The ECM not only supports these cellular functions but is also modified by the cells it supports, thus establishing a ‘dynamic reciprocity’ between the ECM and cells¹². This ability to support and yet be modified by the temporal cellular events occurring within the matrix hints at a potentially greater function for ECM - information recording and storage¹³. Here, we posed a unique hypothesis that the matrix protein fibronectin is able to record its force loading history in ways that significantly impact how cells sense and respond to the matrix, with particular relevance in ECM-centric diseases like fibrosis and cancer. Fibronectin, like other elastic proteins (e.g. Titin), contains specific repeating domains called type-III repeats that are stabilized by van der Waals forces and hydrogen bonding. These noncovalent bonds can be temporally broken and reformed in response to force application and release¹⁴. Buried within two of fibronectin’s many type-III repeats (repeat 7 & 15) exists a ‘free’ cysteine, a precious thiol-containing amino acid, rarely unmodified in the highly oxidizing extracellular environment^{15,16}.

Oxidant stress (a.k.a. reactive oxygen species; ROS), the natural product of aerobic metabolism, consists of radical and non-radical species produced by the partial reduction of oxygen¹⁷. Elevated systemic oxidative stress is strongly associated with obesity and metabolic disorders¹⁸, inflammatory diseases like arthritis, interstitial lung disease, and cardiovascular disease¹⁹, and cancer²⁰. The lung, in particular, is the organ most highly exposed to oxidative stress through direct contact to the external environment²⁰. The lung displays more antioxidant activity than any other organ and disruptions in the oxidant/antioxidant balance have long been linked to pathological disorders in the lung²¹; disruptions in the oxidative balance in lung is a fundamental hallmark of lung fibrosis and cancer.

Glutathionylation in lung cancer and disease

ROS is capable of inducing both reversible and irreversible oxidative post-translational modification (Ox-PTM) of cysteine and methionine on many different proteins²². Glutathione, a prominent antioxidant, reacts with partially oxidized cysteines resulting in S-glutathionylation. The addition of glutathione to cysteine is reversible and prevents irreversible hyper-oxidation of cysteine thiol side chains²³. Elevated S-glutathionylation has been reported in idiopathic pulmonary fibrosis patients, linked to decreased enzymatic activity of glutaredoxin-1 (GLRX); reducing protein oxidation reverses lung fibrosis²⁴. While the bulk of research efforts in pathological ROS are focused on intracellular signaling, post-translational modifications including glutathionylation are emerging as key regulatory events in the ECM²⁵.

Remodeling by fibroblasts

As mentioned earlier, a major pathological process in UIP is the deposition of provisional matrix, made up by fibrinogen and Fn, in the alveolar spaces following lung injury. Evidence suggests that this provisional matrix could stimulate epithelial to mesenchymal transition even without TGF β stimulation⁴. Persistence of such matrix leads to the activation and differentiation of fibroblasts to myofibroblasts which organize in fibroblastic foci and release excessive amounts of ECM⁴. Fibroblasts that have differentiated down a contractile, myofibroblastic pathway are known to exhibit significant contractile force. Such cell-derived forces are capable of stressing the surrounding ECM, possibly leading to increased microenvironmental strain, including Fn²⁶. Myofibroblast presence and the related strain increase of fibrillar ECM proteins could become a significant UIP marker to facilitate diagnosis.

Our lab and others have shown that mature, fibrotic lung ECM is significantly stiffer compared to normal ECM²⁶, while the fibroblastic foci are just as soft²⁷, using atomic force spectroscopy. Thus, it is theorized that the mechanical changes to the Fn matrix may be a molecular signature for progression of the disease. It is high time to fully introduce the titular protein, Fn.

RELEVANCY OF FIBRONECTIN CONFORMATION

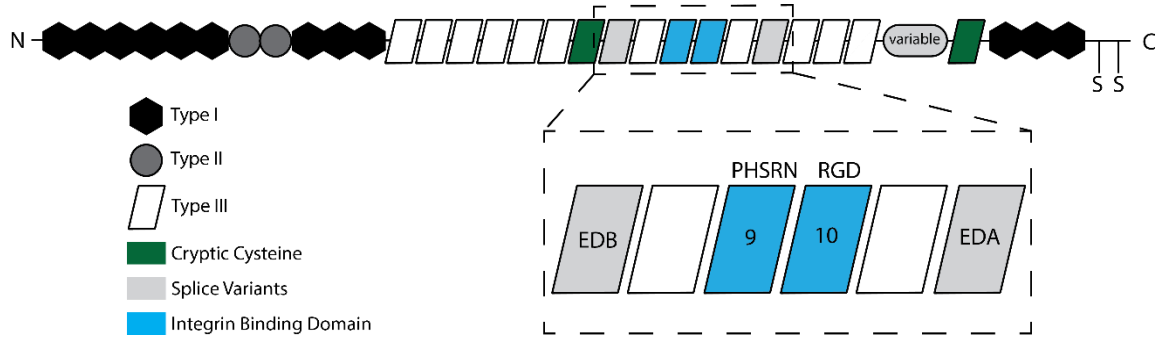


Figure 4: Structure of fibronectin, with detail on Integrin Binding Domain

Fn is a glycoprotein formed by two identical subunits weighing 220 kDa each that are covalently linked by two disulfide bonds towards the C-termini. Each subunit is composed of three repeated domain types: Type I, Type II and Type III²⁸. Among ECM fibular proteins, Fn is of particular importance to the pursuit of scarless healing because of its presence in the provisional matrix of remodeling tissues [1], its effects on cell behavior through specific integrin interactions [2], its high degree of spatial flexibility [3], and its unfolding response to force [4].

While Types I and II are set in a rigid conformation because of internal disulfide bonds, Type III domains completely lack this feature. Specifically, Type III domains consist of antiparallel β sheets connected by flexible loops and held together by hydrogen bonds^{29,30}. Consequently, Type III repeats are highly susceptible to force-induced unfolding³¹. The 10th Type III repeat in Fn (10III) was determined to be the Type III repeat with the lowest threshold for deformation with both steered molecular dynamics and atomic force microscopy¹⁴, implying that it will be one of the first domains to unfold under force. This property of 10III can affect its integrin binding domains (IBD) and the canonical RGDS sequence,

which are both used for cellular attachment to Fn. The 9th Type III repeat (9III) contains a synergistic site with sequence PSHRN that provides domain recognition and mediates cell adhesion and cytoskeletal organization^{32,33}. The proximity of these two sites has been the object of several studies because of the importance of physical coupling between extracellular domains and integrin selectivity. Indeed, RGD peptides by themselves are not enough to select specific integrin binding, since they are ubiquitous in other ECM proteins and ligate several kinds of integrin³³. On the other hand, integrin $\alpha 5\beta 1$ binding requires RGD and the PSHRN sequence on 9III³⁴ to be about 32 Å apart. However, when a force of just 10 pN is applied, the 10III partially unfolds and the RGD domain is removed from the synergy site, so that the distance between the two increases to 55 Å³¹. This 23 Å change greatly reduces $\alpha 5\beta 1$ binding³⁵. Conversely, integrins that do not coordinate binding with the synergy site, such as $\alpha v\beta 3$, are not affected by the change in distance³⁶. Given that the distance between 9III and 10III can turn on or off some integrin binding, this region is called the 9III-10III integrin switch.

Beyond the 9III-10III integrin switch, Fn contains other variable domains that can affect the wound healing process. The Extra Domain Type III A (EDA) and Type III B (EDB) can be spliced between the 11III and 12III, and between the 7III and 8III, respectively. These alternative forms of Fn may include EDA, EDB or both and are secreted locally by cells, with the exception of hepatocytes which secrete plasma Fn (pFn) in the bloodstream. Since hepatocytes do not begin their synthetic activity during gestation, fetal Fn contains both extra type domains. This suggests that EDA and EDB Fn plays a role in development. Indeed, altering the EDB sequence while keeping the exon is embryonically lethal³⁷, as does deletion of

both extra domains³⁸. On the other hand, deletion of either EDA or EDB allows for a viable embryo with little defects^{39,40}. While levels of cell-secreted Fn (cFn) decrease with age in animals ^{41,42}, the extra domains are expressed alternatively to contribute to wound healing and related pathologies. An x-ray crystallography study on the presence of EDB in 7-9III Fn fragment reported a strong twist in the tertiary structure of Fn, which enabled a tight head to tail packing of two Fn molecules leaving the two Fn IBDs (9III and 10III) accessible, facing the same side and in close proximity. This new finding in the supramolecular, quaternary assembly of cFn fibers implies powerful downstream cellular signaling due to integrin receptor clustering⁴³.

Unlike EDB cFn, EDA cFn is present in the granules of platelets⁴⁰ and contributes to an accelerated thrombosis effect⁴⁴. EDA, produced by fibroblasts and absent in pFn, is needed for the transition from inflammation to the repair phase of wound healing. Consequently, EDA cFn makes up part of the provisional matrix and favors fibroblast infiltration. Unsurprisingly, it was found that EDA Fn knockout mice are protected from bleomycin-induced pulmonary fibrosis, while inflammation states and SMAD signaling did not differ from wild type mice. However, injury with a high dose of bleomycin led to higher mortality in EDA KO mice. Given that EDA KO mouse-derived fibroblasts plated on EDA cFn show the typical response after exposure to TGF- β ^{45,46}, we can be confident that this effect is protein specific. We explain this apparent contradiction between low and high bleomycin mouse models by accounting for the unabated inflammation processes. Since EDA is necessary for the transition to the repair phase, knocking it out would continue the secretion of free radicals and localized cell necrosis associated with

inflammation. In conclusion, EDA and EDB play essential, nuanced roles in development and phases of wound healing, making targeted intervention complicated and prone to side effects.

In addition to the above findings, EDA is necessary for accumulation of latent TGF- β -binding protein 1 in the ECM, which complexes the inactive form of TGF- β along with the latent associated peptide^{45,47}. The effects of TGF- β signaling span from inflammation to the repair phase of wound healing and are covered below.

INTEGRINS BINDING FIBRONECTIN

Due to its binding sites for integrins, ECM proteins, growth factors, and other Fn molecules, Fn can influence coordinated tissue behaviors, including morphogenesis, wound healing⁴⁸, and even pathologies like idiopathic pulmonary fibrosis (IPF). This led to a hypothesis that the force sensitivity of Fn enables mechanosensitive control of ligand recognition¹⁵. To investigate this mechanism, recombinant 9III and 10III were expressed as single Fn fragments for in vivo integrin targeting experiments. While the Fn matrix mimicking constructs by the Hocking group⁴⁹ showed improved wound repair, the contribution of integrins $\alpha 5\beta 1$ and $\alpha v\beta 3$ could not be conclusively discerned. To overcome this, a leucine to proline modified version, Fn 9*10, was developed to provide greater stability to RGD and the synergy site³¹. This new fragment offered more clustering of $\alpha 5$ integrins than wild type Fn. This and other assays suggest that integrin engagement selectivity affects disparate cell responses, including but not limited

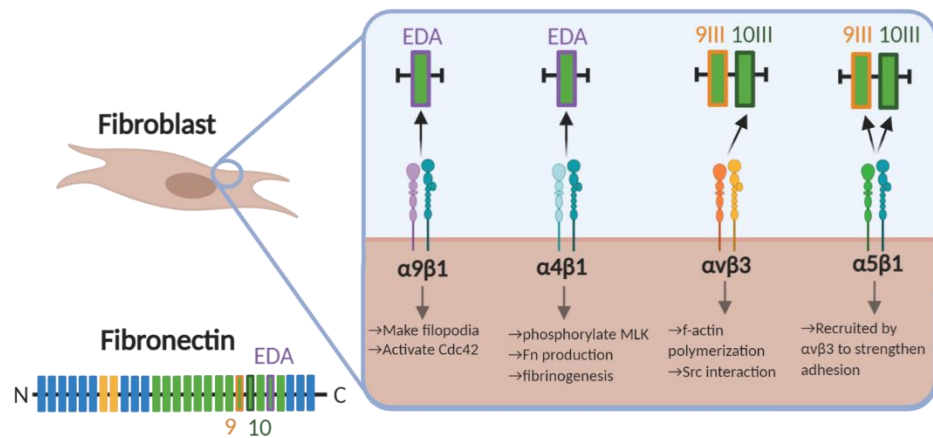


Figure 5: In the bottom left, cartoon showing the structure of one Fibronectin (Fn) monomer, with Type I repeats in blue, Type II in yellow, and Type III in green. The fibroblast integrins binding Fn are the following: $\alpha 9 \beta 1$ and $\alpha 4 \beta 1$ bind the Extra Domain A present in cell secreted Fn, whereas $\alpha v \beta 3$ and $\alpha 5 \beta 1$ bind the canonical Integrin Binding Domain. While $\alpha v \beta 3$ binds the RGD motif on the 10th Type III repeat (and other proteins), integrin $\alpha 5 \beta 1$ requires the "synergy" PHSRN peptide sequence on the 9th Type III to be in close proximity. Cell-generated forces on Fn fibers can unfold the Type III repeats, increasing the distance between RGD and the synergy site, inhibiting $\alpha 5 \beta 1$ engagement. Under those conditions, only $\alpha v \beta 3$ can properly bind the Integrin Binding Domain of Fn. This phenomenon, first predicted via steered molecular dynamics, has been named "integrin switch".

to the ability of cells to migrate on or assemble a Fn matrix⁵⁰. Furthermore, recombinant 9III and 10III were expressed with the addition of short flexible linkers, mainly made up by consecutive glycine residues, in order to provide tensile character and increase distance between the synergistic site and RGD⁵¹. Such integrin-specific Fn constructs managed to mask the stiffness induced epithelial-to-mesenchymal transition once conjugated to polyacrylamide (PAA) gels of varying stiffness, supporting that the integrin specificity mechanism plays a role in wound healing and the provisional matrix. Our lab has successfully employed a similar Fn fragment with a 4-glycine linker to screen for a single-chain antibody fragment detecting the transient, force-induced conformational change of the IBD. This antibody provided direct experimental evidence for the Fn integrin switch, both in vitro and ex vivo (mice models)⁵².

Given the results on the force threshold for 10III unfolding, we suggest that cells interacting with ECM generate forces sufficient to distance the two repeats of the IBD. Indeed, fibroblasts' lower bound for mechanical force exerted is in the tens of nN, which is well above the force required to unfold the 10III repeat⁵³.

All the studies on Fn mechanics and the ones relying on Fn fragments suggest that the unfolding of the IBD takes place in wound healing, possibly driven by fibroblastic forces to guide integrin specificity. This tightly regulated and nuanced process could lead to excessive scarring and downstream fibrosis if tampered with. As such, Fn IBD could be targeted to alter specific integrin engagement, thus affecting important cytosolic pathways. Besides peculiar mechanical properties, Fn has extra domains that can affect progression of fibrosis.

$\alpha v\beta 3$ and $\alpha 5\beta 1$

These two integrins bind the canonical IBD of Fn, defined by the accessible RGD peptide sequence on the 10III repeat. While this ligand is sufficient for $\alpha v\beta 3$ binding, $\alpha 5\beta 1$ also requires the PSHRN peptide sequence on the 9III repeat, the “synergy site”, in close proximity.

Recent studies⁵⁴ indicate that the $\alpha v\beta 3$ integrin in physiological conditions outcompetes $\alpha 5\beta 1$ when initiating binding on Fn, but afterwards recruits $\alpha 5\beta 1$ to strengthen adhesion through a mechanism involving talin sequestration, ICAP-1 permanence, kindlin, ILK, RhoA/ROCK and Rac1/Wave/Arp2/3 pathways. Despite advances in understanding mechanotransduction, experiments to better define the effects of the integrin switch still have to be performed, particularly in the context of Fn conformation and fibroblasts in fibrosis. Src, a member of the Src

Family Kinase (SFK), binds constitutively to β_3 ⁵⁵ and is activated following integrin engagement. This allows Src to bind to and promote the activity of one of its downstream targets, focal adhesion kinase (FAK). FAK can phosphorylate paxillin, a molecular scaffold for other focal adhesion proteins, that when interacting with adapter molecule crk (p38) leads to Rac1 activation and downstream f-actin polymerization⁵⁶. Moreover, active Src can promote phosphorylation of kindlin-2 and form a complex with it, which in turn promotes phosphorylation of paxillin⁵⁷. What is critical to myofibroblast differentiation is that these events lead to enhanced polymerization of f-actin, which in turn drives the translocation of myocardin-related transcription factor (MRTF) (normally cytoplasmically sequestered by g-actin) into the nucleus, where after complexing with serum response factor (SRF), instructs transcription of myofibroblastic and fibrosis relevant genes. Interestingly, recent work on cancer ECM shows that fibroblasts with inhibited, knocked out, or dominant negative FAK regained myofibroblastic development when an $\alpha_5\beta_1$ inhibiting antibody was administered (49). Src, Fyn, and Yes (all SFK members) null fibroblasts instead did not show myofibroblastic traits after $\alpha_5\beta_1$ inhibition, suggesting non-equivalent function for Src and FAK⁵⁸.

$\alpha_4\beta_1$ and $\alpha_9\beta_1$

The integrins described here also bind Fn but in domains other than the IBD. Specifically, both integrins bind Fn EDA. As mentioned earlier, this domain is present only in the Fn secreted by fibroblasts in situ. $\alpha_9\beta_1$ binds to the TYSSPEDGIHE peptide sequence displayed on the C-C' loop of EDA⁵⁹.

Engagement of EDA with $\alpha 9\beta 1$ leads to formation of filopodia, which fibroblasts use to probe substrate stiffness⁶⁰ and activate Cdc42, a GTPase involved not only in migration and cytoskeletal remodeling, but also in the cell cycle progression from G1 to S phases and mitosis. Additionally, blocking $\alpha 9\beta 1$ via a specific antibody slows and reduces formation of granulation tissue during skin wound healing, as shown in excisional wound mice models without altering wound closure time^{61,62}. This phenomenon is arguably closer to the ideal scarless wound healing, because the more granulation is present, the less the functionality of the tissue is restored. While Nakayama reports that $\alpha 9\beta 1$ blocking does not reduce fibroblast migration and proliferation, the lack of effect might be explained by an $\alpha 4\beta 1$ compensation mechanism. Indeed, as $\alpha 4\beta 1$ shares 39% of its amino acid sequence with $\alpha 9\beta 1$ ⁶³, it is not surprising that they bind the same site on EDA FN. Given the effects of the EDA domain (including increased stress fiber formation and phosphorylation of myosin light chain kinase, which further F η synthesis and fibrillogenesis), blocking $\alpha 4\beta 1$ with a specific antibody or knocking its expression down via siRNA indicates a significant reduction of this profibrotic progression, thus suggesting $\alpha 4\beta 1$ as a viable target for a future antifibrotic therapy⁶⁴. However, engagement of EDA FN by $\alpha 4\beta 1$ has not been correlated with increased α SMA expression, a marker of myofibroblastic transition.

MYOFIBROBLASTIC MARKERS

Myofibroblasts, activated fibroblasts that assemble, contract, and stiffen ECM, are thought to be the culprit of fibrotic disease progression. Unfortunately, myofibroblast remodeling of the microenvironment drives further differentiation

of naive fibroblasts as a consequence of their adaptation to the stiff microenvironments generated by myofibroblasts. In fibrotic conditions, these cells show an increased resistance to apoptosis, fueling this vicious cycle of ECM secretion and force generation via α SMA expression. For these reasons, it would be ideal to precisely target myofibroblasts in order to address fibrotic progression.

While the field has focused on α SMA and FN EDA expression to identify fibroblasts transitioned to myofibroblasts, recent work shows that these markers might not be sufficient to assure complete targeting of ECM remodeling cells in pathological conditions⁶⁵.

Diverging once again from the known behavior of adult fibroblasts, α SMA has been shown to be always expressed at low levels by fetal fibroblasts⁶⁶. ECM secreted by fetal (myo)fibroblasts contains more collagen III and is organized in a weave pattern, similar to uninjured ECM. As such, fetal wounds regain all of their mechanical strength unlike adult or postnatal scars. Fibroblast-specific protein 1 (FSP-1) was introduced as a unique fibroblast marker, but despite its expression level correlation with the progression of various fibrosis models⁶⁷, more in depth work indicated that its expression is not limited to fibroblasts⁶⁸ or that cells expressing it do not fall within the myofibroblastic phenotype⁶⁹.

On the other hand, Xu's team showed that cells expressing PDGFR α comprise 95% of the myofibroblasts contributing to fibrotic remodeling in the bleomycin murine model of lung fibrosis⁷⁰. Given the continued search for a defined fibroblastic marker and the debate in the field, the best approach to identify myofibroblasts should rely on a combinatorial approach of phenotypical

functions, which are not limited to the molecules listed above. Indeed, myofibroblasts present in fibroblastic foci and involved in ECM remodeling express prolyl 4-hydroxylase for collagen crosslinking⁷¹.

Integrins of (Myo)Fibroblasts

In addition to biochemical stimuli, fibroblasts respond to mechanical cues from their environment, in a process defined as mechanotransduction, which has been implicated as a key axis driving activation of naive fibroblasts down a myofibroblastic lineage.

Mechanotransduction is a cell phenomenon involving conversion of physical energy into biochemical activity. This can occur at the level of individual proteins (molecular) that undergo conformational changes in response to force and at the level of cellular/subcellular macromolecular complexes, which both transmit and translate forces through activation of key signaling pathways⁷². The primary force-sensing apparatus at the fibroblast-ECM interface is the focal adhesion⁷³, comprised of receptors (i.e. integrins) specific to particular motifs within various ECM proteins, like fibronectin (Fn), and a plethora of adaptor proteins and key kinases, like FAK and Src family kinases (SFK) among others⁵⁶. Importantly, there is recent evidence that specific integrins, such as $\alpha v \beta 3$, may be potentially pathological mechanotransducers while others, such as $\alpha 5 \beta 1$, may play more fundamental structural roles during normal physiology⁷⁴. In the following sections, we will discuss the integrins expressed by (myo)fibroblasts, grouped on the basis of their binding site and ligand.

$\alpha 1\beta 1$, $\alpha 2\beta 1$, and $\alpha 11\beta 1$

All these integrins bind, among other ECM proteins, fibrillar collagens, including type I and III, which are the most abundant collagens secreted during formation of the provisional matrix and scarring. It has been hypothesized that these integrins have limited binding sites under physiological conditions due to the tight alpha helices that make up collagen⁷⁵. The binding sites would become accessible after injury, during development, or during the secretion and assembly of the provisional matrix. While it has been shown that all three integrins bind the collagen consensus GFOGER sequence^{76,77}, more recent in vitro studies indicated GLOGEN as the more potent binding site of $\alpha 1\beta 1$ ⁷⁸. Since the latter peptide sequence is present on collagen III and $\alpha 1\beta 1$ engagement downregulates collagen secretion⁷⁹, it can be hypothesized that such binding events play a role as a negative feedback loop during fetal scarless wound healing, where collagen III is more abundant than in adult^{80,81}. Integrin $\alpha 1\beta 1$ downregulates expression of MMP13 via a Raf-1, MEK1/2, ERK1/2 pathway⁸². On the other hand, $\alpha 2\beta 1$ engagement on collagen upregulates MMP1⁷⁹ and MMP13⁸². Increased expression of the latter is due to MAPKKK, MKK3/6 mediated activation of p38. Enhanced production of MMPs is typically correlated with increased migration and invasion of fibroblasts at first, then increased provisional matrix remodeling. It has been suggested that $\alpha 2\beta 1$ engagement in 3D collagen I lattices also promotes NF-kB signaling, possibly via PCK-zeta⁸³ or PI-3K, thus upregulating the same collagen I⁸⁴. For the above reasons, activation of the downstream $\alpha 2\beta 1$ effectors could be considered as an undesired progression of wound healing towards fibrotic characteristics. However, the effects of this integrin on fibrosis might be tissue specific. While knockout mice

models of glomerular injury displayed reduced granulation tissue via negative regulation of collagen synthesis (92), ex vivo assays showed a significantly reduced $\alpha 2\beta 1$ expression in IPF fibroblasts when compared to control. In the latter case, higher levels of inactive GSK-3 β were found, due to reduced PPA2 activation⁸⁵.

$\alpha 11\beta 1$ is an integrin present only in a subset of all fibroblasts, yet it is the major collagen I receptor in dermal fibroblasts. This integrin is largely induced in excisional wounds, but knockout models indicate reduced formation of granulation tissue⁸⁶. Not only has TGF- $\beta 1$ been shown to regulate integrin $\alpha 11$ via its downstream partners SMAD2/3⁸⁷, but also by non-canonical Jun N-terminal kinase (JNK)-dependent TGF- β signaling, which was shown to be crucial for $\alpha 11\beta 1$ -dependent collagen secretion. Although more information is necessary to link JNK activation with $\alpha 11\beta 1$, Gullberg et al. suggest TGF- β Activated Kinase 1 (TAK1) as a potential candidate⁸⁸. More recently, overexpression of $\alpha 11$ in a transgenic mouse model led to a phenotype closely matching cardiac fibrosis⁸⁹.

These findings implicate integrin $\alpha 11\beta 1$ as a potential therapeutic target by blocking it in the context of myofibroblast differentiation during scar formation and pathological fibrosis in general⁶².

Further studies of these collagen-binding integrins relying on integrin-KO mice might be hindered by the $\beta 1$ subunit, shared by several integrins. Nonetheless, in the light of differential fetal fibroblast integrin expression, elucidating which integrin signaling contributes the most to the healing process would provide the field with a druggable target for the pursuit of scarless wound healing in adults.

HYPOTHESIS AND SUMMARY

The current Clinical Practice Guideline on management of IPF recommends several pharmacological treatments such as pirfenidone, a downregulator of key profibrotic factors, and nintedanib, an inhibitor for several tyrosine kinases. While the latter two compounds showed most promise in recent clinical trials, none of them represent a cure for IPF since patients continue to degenerate despite such treatments⁵. Moreover, the serious side effects of either drug lower the patient's quality of life while discouraging medication compliance. Because today IPF is still an incurable disease outside of a lung transplant, it is necessary to extensively investigate the mechanisms behind the etiology and progression of UIP in general, in order to identify targets for therapy in the near future.

Given all the considerations above, I hypothesize that the Fn IBD conformation is a “druggable” driver of fibroblast activation.

What follows is the recollection of a multi-pronged attempt to first find the Integrin Switch (IntSw) in mouse models of lung fibrosis *in vivo*. I rediscovered an antibody that can target the Fn IBD, with increased specificity towards its unfolded, pathologically associated conformation where it outcompetes integrin $\alpha\beta_3$. The antibody was labelled with VivoTag dyes and used to first monitor lung fibrosis development in live mice that received intratracheal bleomycin after 2 weeks. I also developed a novel triple transgenic mouse line in order to test whether affecting the IntSw by conditionally knocking out the other integrin involved, $\alpha_5\beta_1$, aggravates lung fibrosis.

In my single cell force spectroscopy experiments I observed that $\alpha 5\beta 1$ engagement was needed to generate high adhesion forces even at short time points (<120s), in accordance with previous literature. Luminex analysis highlighted increased activity in Rac pathways over Ras signaling for fibroblasts seeded on the open IBD conformation fragment. My mass spectroscopy work indicated that pro-fibrotic pathways and, particularly, collagen XIIa and tubulin beta3 appeared to be enriched upon increased $\alpha v\beta 3$ binding at 30'.

After culturing for 24h on soft substrates (5 kPa representing healthy lung tissue), lung fibroblasts plated on the open IBD Fn fragment predominantly engaged $\alpha v\beta 3$ and displayed increased nuclear translocation of transcription factors associated with a secretory and contractile phenotype. Fn (with Extra Domain A), Tropomyosin, Vimentin, Serpine1, and α integrins were among the genes upregulated on the open Fn fragment, compared to the closed fragment. These results were confirmed by qPCR and then bulk RNAseq assays.

In conclusion, these data support that differential integrin engagement due to Fn IBD unfolding appears to affect cell phenotype in both the short and long run. This work contributes to understanding the link between changes in the ECM and cell behavior in the context of fibroproliferative diseases. Furthermore, not only did I identify a novel druggable target in lung fibrosis, but I further validated a research tool with diagnostic potential.

CHAPTER 2

IN VIVO DETECTION AND BIOLOGICAL RELEVANCE OF THE INTEGRIN SWITCH

INTRODUCTION

Cells and particularly fibroblasts sense the mechanical properties of the extracellular matrix (ECM) primarily through integrin receptor engagement of the actinomyosin contractile machinery in a manner that facilitates mechanical homeostasis between the cell and its environment⁹⁰⁻⁹².

Integrin-ECM binding occurs within adhesive structures, termed focal adhesions, which couple the cytoskeleton to fibrillar ECM proteins, such as Fibronectin (Fn). Integrins are the main transmembrane receptors that bind ECM and facilitate force transmission and signaling (i.e. mechanosignaling). This “interaction landscape” is further modified by applied forces: conformations and activity of both focal adhesion components as well as ECM proteins (e.g. Fn) are altered by forces. Indeed, our previous work demonstrates that Fn fibers within the ECM exhibit distinct structural states in response to cellular forces⁹³. In other words, cells exist within a microenvironment that is both responsible for and regulated by mechanical force, either externally applied (i.e. tissue stretch during respiration) or internal (i.e. actomyosin contractility). Importantly, as Fn is 1) significantly upregulated during wound repair and in fibroblastic foci of fibrotic diseases presenting as Usual Interstitial Pneumonia (UIP)^{46,94}, 2) associated with the contractile myofibroblast phenotype⁹⁵⁻⁹⁷, and 3) a necessary template for cellular assembly of the type I collagen fibers prevalent in scar tissue^{98,99},

mechanisms regulating the mechanochemistry of fibroblast-Fn interactions appear critical to the pathophysiology of UIP. Furthermore, fibrotic ECM has been identified as a driver of pathological fibroblasts' phenotypes, indicating the ECM remains an exciting underexplored target for treatment^{100–102}.

At the molecular level, work by Vogel and others have shown that due to their unique structure, Fn type III repeats, such as the integrin binding 9th and 10th type III repeats, can undergo force-induced unfolding/refolding behavior^{15,103–105}. These findings have led to theorize that force-induced conformational changes within the integrin binding domain (Fn 9-10III) regulates specific integrin engagement – the so-called “integrin-switch” hypothesis¹⁰⁶. The integrin-binding domain (IBD) of Fn spans the 9th and 10th type III repeats, and is perhaps the most biologically active portion of the molecule in terms of engaging integrin receptors and mediating cell-ECM adhesions. Indeed, the RGD peptide sequence that is used routinely for targeting, facilitating, and inhibiting integrin binding was originally discovered from the 10th Fn type III repeat¹⁰⁷ and binds many integrin subtypes, including all of the α_v family. However, the 9th type III repeat of Fn contains at least one synergistic integrin-binding motif (PHSRN) that further facilitates integrin specificity. The physical distance between PHSRN (‘synergy’) and RGD is critical for engagement and activation of certain integrins, such as the synergy-dependent integrin $\alpha_5\beta_1$ ^{106,108}. RGD and synergy are separated by 3.7nm in the unstressed, natively folded IBD¹⁰⁹, which we consider the “off” state of the integrin switch. Molecular simulations reveal that physiologically relevant forces are capable of inducing a stable intermediate where PHSRN and RGD are separated by 5.3nm^{34,105}, which effectively decouples synergy and RGD and leads to

predominately αv integrin engagement^{110,111}, hence unfolding the Fn IBD and the “on” state of the integrin switch.

Since increased $\alpha v \beta 3$ signaling has been associated with fibrosis, further understanding the downstream effects of this differential integrin binding could elucidate several unresolved diseases’ mechanisms. We hypothesized that this change in Fn conformation affects lung fibroblasts by guiding integrin enrichment, pushing them towards a secretory and pro-fibrotic phenotype.

First, we used the single chain fragment antibody described previously¹¹² to monitor lung fibrosis development in live mice that received intratracheal bleomycin 2 weeks prior, validating the existence of the Integrin Switch (IntSw) in vivo. Then, we tested this premise by engineering Fn fragments containing the IBD site that mimicked either the open or closed conformation and employing them as substrates for several in vitro experiments.

In our Single Cell Force Spectroscopy experiments we observed that $\alpha 5 \beta 1$ engagement was needed to generate high adhesion forces even at short time points (<120s), in accordance with previous literature. Luminex analysis of phosphorylation levels of signaling kinases highlighted increased activity in the PI3K-Akt pathway for fibroblasts seeded on the open IBD conformation fragment. Our Mass Spec analysis of the adhesome indicates that collagen XIIa, tubulin beta3 and members of the PI3K-Akt pathway appeared to be enriched upon increased $\alpha v \beta 3$ binding at 30 minutes.

After culturing for 24h on soft substrates (5kPa representing healthy lung tissue), lung fibroblasts plated on the open IBD Fn fragment predominantly

engaged $\alpha v \beta 3$ and displayed increased upregulation of pathways involved with protein synthesis, proliferation, cytoskeletal remodeling, and apoptosis resistance.

Taken together, these data support that differential integrin engagement due to Fn IBD unfolding appears to affect cell phenotype in both the short and long term. This work contributes to understanding the link between changes in the ECM and cell behavior in the context of fibroproliferative diseases.

EXPERIMENTAL SETUP

As mentioned earlier, I devised an elegant method for purifying H5 and its isotype control E3. The convenience stems from the relatively weaker integrity of *E. coli* BL21 DE3 pLysS cell wall associated with the PelB leader in the scFv sequences. As verified in the early days of my PhD work at UVa, the overwhelming majority of the produced H5 ends up being secreted in the cytosol after induction of *E. coli* by IPTG, compared to the periplasmic or cytosolic fractions (not shown). Thus, the supernatant containing the antibody of interest can be separated from the bacterial culture via traditional centrifugation. H5 and E3 can then be easily collected and then eluted from a column packed with Protein L (GE Lifesciences), given that both of their light chains belong to the kappa category¹¹³. Purification of both scFvs can be achieved with the same buffers and protocol performed by an AKTA Pure (GE Lifesciences) High Performance Liquid Chromatographer or more affordable systems.

E3 was expressed in-house and chosen as isotype control because it binds a short peptide sequence (LFPAP) found on the EDA repeat of human and murine

Fn. Only Fn molecules secreted by cells other than hepatocytes contain FnEDA (Figure 4). Indeed, given EDA containing Fn is secreted by fibroblasts participating in remodeling, the field has attempted developing several antibodies against this repeat to either monitor fibrosis non-invasively or drug this target and interrupt or revert deleterious signaling derived by integrin engagement with FnEDA. Conveniently, there is only one target for H5 (IBD) and one for E3 (FnEDA) for each molecule of Fn, enabling a proper comparison between the two scFvs.

For the reader's benefit, the purification protocol is reported below (Appendix B) with the necessary minutia.

The purified antibodies had their buffer exchanged to PBS and were conjugated with either fluorescent VivoTag dye (H5 with 645, E3 with S750) (Perkin Elmer, #NEV11173 and #NEV10123 respectively, Waltham, MA) according to the manufacturer's instructions. The antibodies were then sterilized via filtration through a 0.22 μm syringe filter and preserved at 4 C until they were administered to male C57BL6 mice aged 8 weeks that had received either a saline (vehicle control) or bleomycin intratracheal spray.

Bleomycin model

Animals were anesthetized with a ketamine/xylazine cocktail (60/5 mg/kg). Animals were placed on a commercial board from Hallowell EMC and hung by their incisors at 45°. Bleomycin sulfate (0.2 U/kg) (Meitheal Pharmaceuticals, Chicago, IL, USA) in normal saline or normal saline vehicle control was instilled into the lungs through the trachea through angiocatheter tubing placed down the animal's throat and connected to a 1mL syringe. Mice were monitored during and

post- procedure to ensure recovery from anesthesia and not returned to housing until they were fully ambulatory and breathing normally.

A total of 18 animals were employed in this study, with 10 receiving saline and 8 bleomycin. All of them received FTY720 (Cayman Chemicals # 10006292, Ann Arbor, MI) dissolved in DI water at 1 mg/kg via IP injections, three injections spread over a week, for a total of two weeks.

Two weeks after the only bleomycin or saline intratracheal spray, the mice received a 2 nmol dose of each fluorescently labelled antibody via tail vein injections. Mice were then euthanized after either 30 minutes, 1, 2 or 4 hours, their organs explanted and imaged with an IVIS at the recommended excitation and emission wavelengths of the VivoTag dyes, H5 with 645 and E3 with S750, respectively. Acquisition settings were “high” sensitivity and 2 seconds exposure. Two sets of mice organs were imaged per frame. The analysis was performed by drawing regions of interest around each organ on the IVIS analysis software.

Inducible model of integrin $\alpha 5$ knock out

Fo PDGFR α -rtTA x tetO-Cre mice were kindly donated by the Sun lab at UCSD. We began crossing them with homozygous mice that had the first exon of gene ITGA5 floxed (Jackson Labs, JAX 032299). All litters were genotyped by using the primers in this table, using the “Touchdown” thermocycler protocol recommended by Jackson Labs.

rtta Fwd	GAA ATT GCA TCG CAT TGT CTG
rtta Rev	AGA AAG ACC TGG TGG GAG GT
CRE Fwd	GCG GTC TGG CAG TAA AAA CTA TC
CRE Rev	GTG AAA CAG CAT TGC TGT CAC TT
ITGA5 Fwd	TTC TCC GTG GAG TTT TAC CG
ITGA5 Rev	AGG TTC TTC CAC TGC CTC CT

Table 1: Names and sequences of DNA primers used for genotyping

Naïve mouse lung fibroblasts

Briefly, mice were humanely euthanized via ketamine/xylazine anesthesia followed by cervical dislocation. Lungs were explanted and dissociated by using Liberase (Roche) and DNase. Mouse cells were filtered through a cell strainer and allowed to seed and grow on progressively larger tissue culture plastic for up to two weeks. Then fibroblasts were seeded on ExCellness PDMS-gel plates (5 kPa) that were coated with gelatin for two weeks before fibroblasts were considered naïve and ready to be used, usually serum starved, for the experiments reported here. Further details are in Appendix B.

Functionalizing glass with Fn fragments

Glass surfaces were silanized with 2% APTES in acetone, then functionalized with a maleimide moiety by conjugating sulfo-SMCC. Meanwhile, the Fn fragments were reduced to remove disulfide-induced dimers by using TCEP gels. Reduced fragments were allowed to incubate and covalently bind the glass substrate thanks to the engineered N-terminal cysteine. Further details are in Appendix B.

Single cell Force Spectroscopy

Prior to experiments, tip-less V-shaped cantilevers (200 μm long; NP-O; Bruker) with a nominal spring constant of 0.06 N m^{-1} were plasma cleaned for ~ 5 min and incubated in 2 mg ml^{-1} concanavalin A (conA, in PBS) overnight at 4°C . The spring constant of each used cantilever was determined prior to attaching a single cell to it using the thermal noise method inbuilt into the AFM operations software.

For SCFS a NanoWizzardII AFM (JPK Instruments) equipped with a CellHesion module (JPK instruments) was mounted on an inverted microscope (Observer.Z1, Zeiss). The SCFS medium in the substrate-functionalized glass-bottom petri dish was maintained at 37°C using a PetriDish Heater. Detached and trypsin treatment-recovered fibroblasts were pipetted onto the glass-bottom petri dish and allowed to settle. To attach a single cell to the free end of a conA-coated cantilever, the cantilever was placed over a single fibroblast and lowered onto it with a speed of $10 \mu\text{m s}^{-1}$ until a force of 5 nN was recorded. The cantilever was

maintained at a constant height for 5 s before the cantilever was retracted for $>90 \mu\text{m}$ to completely detach the fibroblast from the substrate-coated petri dish. To ensure firm binding to the cantilever, the fibroblast was incubated at the cantilever for 3-5 min before adhesion experiments. To quantify adhesion forces of the fibroblasts, the cantilever bound fibroblasts were approached to the substrate-coated petri dish with a speed of $5 \mu\text{m s}^{-1}$ until a contact force of 1 nN was recorded. The height of the cantilever was maintained constant for the contact time of 5, 20, 50 or 120 s, before the cantilever was retracted at a speed of $5 \mu\text{m s}^{-1}$ for $>90 \mu\text{m}$ to completely detach the fibroblast from the substrate. The fibroblast was allowed to recover from adhesion experiments for at least the contact time, before probing the adhesion force of the same fibroblast after a different contact time. The contact times were randomized for all experiments. A single fibroblast was used for adhesion experiments on Fn 9-4G-10III and Fn 9*10III for all contact times or until morphological changes were observed (e.g. cell spreading).

Luminex assay

Naïve mouse lung fibroblasts (cultured for 2 weeks on soft 5 kPa gelatin-coated gels) were first serum starved (1% FBS) for 24 hours, then were trypsinized for 10 minutes. After collection, cells were concentrated and resuspended in MEM α with nucleosides (Gibco brand, ThermoFisher #12571048, Waltham, MA) supplemented only with 1% penicillin/streptomycin. Cells were seeded for varying time intervals (5, 15, or 30 minutes) on glass coverslips functionalized with either Fn 9-4G-10III or Fn 9*10III as described in Appendix B, before being lysed with ice-cold Milliplex Lysis Buffer supplemented with 1:100 Halt Protease and Phosphatase Inhibitor Cocktail (ThermoFisher #78440, Waltham, MA).

Fn fragment	Harvest time point (mins)	Biological replicates	MLFs per replicate
4G	5	4	3.38E+05
	15	4	3.75E+05
	30	4	6.00E+05
9*10	5	4	3.38E+05
	15	2	1.50E+05
	30	4	6.00E+05

Table 2: Experimental conditions for Luminex Cell Signaling assay

The phosphorylated proteins of interest were the following: ERK/MAP kinase 1/2 (Thr185/Tyr187), Akt (Ser473), STAT3 (Ser727), JNK (Thr183/Tyr185), p70S6K (Thr412), NF κ B (Ser536), STAT5A/B (Tyr694/699), CREB (Ser133), and p38 (Thr180/Tyr182).

The actual experimental run was performed by UVA Flow Cytometry Core Facility staff according to the protocol provided with Multi-Pathway Total Magnetic Bead 9-Plex kit (MilliporeSigma 48-680MAG, Burlington MA). Readouts were normalized for actual fibroblast content by total GAPDH content measured with GAPDH Total Magnetic Bead MAPmate (MilliporeSigma 46-667MAG, Burlington MA).

Mass spectroscopy of the adhesome

Four T225 flasks of cells per fragment dishes per condition of human lung fibroblasts CCL210 (ATCC) were cultured for 48 h to 90% confluency, trypsinized, then seeded on glass substrates functionalized with either Fn fragment, as described above, for half an hour. Four functionalized plates and two T225 TC flasks were used per fragment in a single replicate. To isolate adhesion complexes, cells were incubated with the membrane-permeable crosslinker dimethyl-3,3'-dithiobispropionimidate (DTBP, Sigma-Aldrich; 6 mM, 5 min). DTBP was then quenched using 1 M Tris (pH 8.5, 2 min), after which cells were again washed once using PBS and incubated in PBS at 4 °C. Cell bodies were then removed by a combination of cell lysis in RIPA buffer (50 mM Tris-HCl, pH 8.0, 5 mM EDTA, 150 mM NaCl, 1% (wt/vol) TX-100, 1% (wt/vol) sodium deoxycholate (DOC), 0.5% (wt/vol) SDS; 3 min) and a high-pressure water wash (10 s). Protein complexes left bound to the tissue culture dish were washed twice using PBS, recovered by scraping in 200 µl recovery solution (125 mM Tris-HCl, pH 6.8, 1% (wt/vol) SDS, 15 mM dithiothreitol), and incubated at 70 °C for 10 min. Each sample was

subsequently precipitated from solution by addition of four volumes of $-20\text{ }^{\circ}\text{C}$ acetone, incubated for 16 h at $-80\text{ }^{\circ}\text{C}$, and resuspended in reducing sample buffer.

For MS, samples were separated by SDS–PAGE on a 4–12% SDS Bis-Tris gel (Thermo Fisher), stained for 10 min with Instant Blue (Expedeon), and washed in water overnight at $4\text{ }^{\circ}\text{C}$. Gel pieces were excised and processed by in-gel tryptic digestion as previously described⁴. Peptides were analyzed by liquid chromatography (LC)–tandem MS (MS/MS) using an UltiMate 3000 Rapid Separation LC (RSLC, Dionex Corporation) coupled to an Orbitrap Elite mass spectrometer (Thermo Fisher). Peptides were separated on a bridged ethyl hybrid C18 analytical column ($250\text{ mm} \times 75\text{ }\mu\text{m}$ inner diameter, $1.7\text{ }\mu\text{m}$ particle size, Waters) over a 1 h gradient from 8 to 33% (vol/vol) ACN in 0.1% (vol/vol) FA. LC–MS/MS analyses were operated in data-dependent mode to automatically select peptides for fragmentation by collision-induced dissociation (CID). Quantification was performed using Progenesis LC–MS software (Progenesis QI, Nonlinear Dynamics; <http://www.nonlinear.com/progenesis/qi-for-proteomics/>)¹¹⁴.

Two replicate experiments were performed. KEGG pathway analysis was performed by using the R package.

Functionalizing soft PDMS gels with Fn fragments

10-cm Petri dishes with a 5 kPa PDMS gel (ExCellness PrimeCoat, Lausanne C.H.) were plasma-etched in a plasma cleaner supplemented with oxygen for 25 seconds. After adding 10 mL of freshly made 1% APTES solution in water to each dish, they were incubated at $60\text{ }^{\circ}\text{C}$ for 90 minutes. After three washes with deionized water, the dishes

were ready to be functionalized with sulfo-SMCC and the Fn fragments, using the same procedure and chemistry for glass substrates. Exhaustive details listed in Appendix B

RNaseq experiment

Naïve mouse lung fibroblasts (2 weeks of culture of soft 5 kPa PDMS gels coated with gelatin, 20% FBS DMEM) were serum starved (1% FBS) for 24 hours before plating. Those cells were trypsinized and seeded on the Fn fragment-functionalized 5 kPa PDMS gels (at least 900'000 MLFs per 10 cm dish, ExCellness PrimeCoat, Lausanne C.H.) and maintained in 1% FBS DMEM for 24 hours more, until harvest with 1mL of Trizol per dish (ThermoFisher Scientific, # 15596-026, Waltham MA).

MLFs were plated on 4 different substrates, defined by the Fn fragment combination, and each at least four biological replicates were assigned to each condition. Those were Fn 9-4G-10III, Fn 9*10III, an equimolar mixture of the two (50:50), and this same 1:1 mixture but incubated with molar excess of H5 (200 µg/mL, 10 mL to cover each dish) (50:50 + H5).

RNA was purified by using a combination of solvent precipitation and a spin-column kit (Zymo Research. # R1014, Irvine CA). Briefly, 0.2 mL of chloroform was added to each sample and shaken by hand for 15 seconds, then allowed to incubate for 3 minutes. The samples, after being centrifuged at 12000 xg at 4 C for 15 minutes, separated in a lower, red phenol-chloroform, an interphase, and a colorless superior aqueous phase. As much of the latter phase was carefully collected, transferred to a new tube and mixed with 1 volume of molecular biology grade ethanol. Mixture was transferred to one spin-column and

centrifuged at RT for 30 seconds at 16000 xg. Each sample was washed with 400 μ L the provided RNA Prep Buffer, spun down then washed twice more with RNA Wash Buffer (700 and 400 μ L). Each sample was then eluted with warm 17 μ L of DNase free water before measuring its concentration with a Qubit High Sensitivity kit (ThermoFisher Scientific, # Q3285, Waltham, MA).

Sample type	Collection date	[conc] ng/uL	RIN
50:50 + H5	12/1/2020	20.5	9.2
50:50 + H5	12/2/2020	41.6	9.1
50:50 + H5	4/2/2021	100.0	9.1
50:50 + H5	4/2/2021	84.0	9.2
50:50 + H5	4/2/2021	64.0	9.2
50:50 + H5	4/2/2021	too high	9.2
50:50	4/2/2021	too high	9.3
50:50	4/2/2021	90.0	9.2
50:50	4/2/2021	60.0	9.4
50:50	4/2/2021	too high	8.9
9*10	2/12/2021	54.0	9.8
9*10	3/31/2021	71.0	7.4
9*10	4/8/2021	59.0	9.9
9*10	4/14/2021	96.0	N/A
9*10	4/14/2021	77.0	N/A
9*10	1/14/2021	9.3	N/A
9*10	5/2/2021	too high	8.9
4G	4/2/2021	54.0	9.1
4G	4/8/2021	16.0	2.4
4G	4/14/2021	54.0	N/A
4G	4/14/2021	93.0	N/A
4G	1/14/2021	7.7	N/A
4G	5/2/2021	too high	8.9
4G	5/2/2021	73	8.7
4G	5/2/2021	too high	8.8

Table 3: submitted RNAseq samples

Out of all the sample submitted (Table 3: submitted RNAseq samples, only those with RIN greater than 7 were further processed into DNA libraries by the Molecular Evolution Core at the Georgia Institute of Technology. Sequencing run

was performed on an Illumina NovaSeq with a 800M, 100 bp paired end reads kit (Illumina, San Diego CA), giving a sequencing depth above 42M reads per sample.

Analysis of the resulting reads was performed with the UVA Rivanna high performance cluster using the DESeq2 package. Plotting the results done in R via the tidyverse package.

RESULTS

The Fn Integrin Switch is activated and detectable in in vivo models of lung fibrosis.

C57Bl/6 mice exposed to bleomycin represent the most documented and used animal model for lung fibrosis¹¹⁵. We delivered bleomycin sulfate directly into the mouse lungs through intratracheal spray once, at the beginning of the study. In this case, primary alveolar epithelial cells are insulted with bleomycin-related DNA strand breaks and oxidative stress. However, it has been reported that the bleomycin injury and thus the fibrotic condition is completely reverted by 30 weeks or earlier for the single injection model. This downside decreases the fidelity of the model to human fibrotic conditions and is unhelpful when trying to document disease progression with a new imaging method. To obviate this pitfall, we supplemented the single bleomycin dose model by repeatedly dosing fingolimod (FTY720) via intraperitoneal (IP) injection and lowering the starting dose of bleomycin (Figure 6A). This model combines the S1P receptor functional antagonist FTY720 to disrupt endothelial barrier function with low-dose bleomycin to induce mild lung injury¹¹⁶. Sustained exposure to FTY720 causes increased vascular leak and intra-alveolar coagulation after lung injury, which also leads to an exaggerated fibrotic response to a low dose of bleomycin challenge¹¹⁷. Fourteen days since bleomycin or saline intratracheal administration, mice received 2 nmoles of fluorescently labelled single chain fragment antibodies targeting Fn. H5, first described in the work of Cao et al. ¹¹², is capable of selectively bind Fn integrin binding domain that has undergone a conformational change that favors integrin $\alpha\beta 3$ engagement over $\alpha 5\beta 1$ (i.e., activated Integrin Switch). H5

was modified for this experiment: at the C-terminus the V5 peptide tag (GKPIPPLLGLDST) was added, followed by a FLAG tag. In addition to enabling detection of H5 by two unrelated sets of antibodies, the FLAG tag (DYKDDDDK) contains many reactive, primary amines in its amino acid side chains (Figure 6A). Such design was deliberately chosen to spatially control common conjugation reactions (i.e. labelling with fluorescent dyes) by increasing the number of reactive sites away from the CDR domains. E3 was expressed in-house and chosen as isotype control because it binds a short peptide sequence (LFPAP) found on the EDA repeat of human and murine Fn (E3 is referred in Figure 6 as FnEDA for clarity). Only Fn molecules secreted by cells other than hepatocytes contain FnEDA. Conveniently, there is only one target for H5 (IBD) and one for E3 (FnEDA) for each molecule of Fn, enabling a proper comparison between the two scFvs.

This live imaging experiment provided several key pieces of data not only about the relevance of the IntSw of fibronectin, but also about key characteristics of scFv H5, such as blood half-life (about half an hour, Figure 10) and biodistribution.

Preliminary experiments (not shown) confirmed the literature's findings describing heightened development of lung fibrosis in the animals receiving FTY720 and intratracheal bleomycin, when compared to the traditional model with just intratracheal bleomycin spray. On the other hand, mice that received both saline and FTY720 did not develop fibrosis. As shown in Figure 6 B, a large portion of the injected, fluorescently labeled antibodies was catabolized in the liver and expelled via urine (kidney signal) in the saline and FTY720 groups. In fibrotic mice,

the H5 scFv remarkably accumulated in its target tissue, the lungs, and appear to be depleted at a slower rate, given the large signal in the kidneys, that was likely due to the increased permanence in the lungs.

When the analysis is focused on the lungs and the four imaging time points selected, the properties of H5 and E3 strongly diverge. In Figure 6 C, all readings have been normalized to the normalized intensity recorder for E3 in non-fibrotic mice at the half an hour time point for clarity. While both E3 and H5 registered an increased lung accumulation (lung fluorescent signal) over non-fibrotic mice that received saline and FTY720 across all time points, H5 signal is significantly higher in the fibrotic mice at 30 minutes since tail vein administration. Additionally, the ratios between normalized intensities for fibrotic mice readings over non-fibrotic readings is much higher for H5, at all time points.

This data supports the existence of the Integrin Switch in fibrotic mouse lungs, since H5 accumulation in the lungs should be explained by an increased amount of its epitope. It is reasonable to also deduce that during fibrosis, the Fn IBD is in the pathologically unfolded, “on” conformation, because the isotype control against FnEDA did not record a comparable increase in fibrotic lung signal. If H5 accumulated in lungs merely due to increased Fn deposition, E3 (anti-FnEDA) would also register a similar relative increase in lung signal after normalization to mice receiving just saline and fingolimod.

If H5 binds the IBD conformation that favors $\alpha v \beta 3$ engagement in vivo, as theorized earlier, could tampering with the Fn engagement of the other integrin in this switch, $\alpha 5 \beta 1$, provoke worse lung fibrosis? The results of this “loss of function” are illustrated in Figure 11. Approaching this question on the cell side and with a

genetic knock out set the stage for clean data at the end. We designed this approach instead of pharmacological inhibitors or other antibodies targeting matrix epitopes (not unlike H5) to minimize confounding factors (Figure 11B). Three genetically diverse groups of mice received the initial bleomycin intratracheal spray and were left alone, with ad libitum access to water and the doxycycline infused diet, until the endpoint. The first group, the homozygous mice (blue plot) had no intact allele for integrin $\alpha 5$, as the inducer, doxycycline was amply dosed before and after the bleomycin administration, and should have expressed PDGFR α at basal level, according to the Sun's group work, that discovered the outsized contribution of PDGFR α -expressing fibroblasts to lung fibrosis remodeling^{70,118}. They received the heaviest losses. The second group, identical to the first except for having one working allele should have been able to maintain a physiological amount of intact $\alpha 5$, as long as remote metabolic issues did not arise. Indeed, they did not in this run. Mortality due to fibrosis was lower than the homozygous group. The last group, which does not have both elements of the promoter, controlled for potential deleterious effects due to bleomycin or doxycycline administration, but received minimal losses, which are in line to what is expected with intratracheal bleomycin sprays. The differences in the survival trends are statistically significant, supporting the conclusion that removing $\alpha 5$ eliminates functional $\alpha 5\beta 1$ heterodimers and that removal of those signaling cascades aggravates lung fibrosis, with lethal consequences.

Fibroblasts develop lower adhesion forces on the activated Integrin Switch due to predominant integrin $\alpha\beta 3$ engagement.

Having shown that unfolding of Fn IBD takes place in remodeling mouse lungs and that activation of the integrin switch impacts fibrosis, we aimed to investigate the effects of the IntSw specifically on fibroblast populations. We discovered the link between a shift in integrin engagement and increased fibroblast activation, as measured by metrics of pathways upregulation and mechanical changes. The systematic approach described next moves from protein interactions to analyzing RNA to confirm the protein-level observation, from short term protein activity (minutes) to long term developments in transcripts (days), to exclude potential concurring explanations for the IntSw hypothesis.

We analyzed adhesion forces of naïve mouse lung fibroblasts depending on their Fn substrate (Fn 9*10III or Fn9-4G-10III) via single-cell force spectroscopy (scFS), described in Figure 7A-C. To confirm attribution of those findings to the IntSw mechanotransduction, I explored the substrates and parameters but this time using engineered mouse fibroblasts expressing one set of integrins ($\beta 1$, αv , both, or none). The significant trends discovered in primary fibroblasts were restated by the poly-integrin KO fibroblasts, all but indicating that differences in adhesion strengths are due to the IntSw.

Naïve mouse lung fibroblasts generate closely comparable adhesion forces, regardless of contact time, when interacting with a rigid substrate functionalized with Fn 9-4G-10III, that simulates the unfolded conformation of Fn IBD. On the other hand, the same cells develop significantly larger adhesion forces, starting at 2 seconds of contact time, when engaging with Fn 9*10III, that mimics the stably

folded conformation of the IBD (Figure 7F). Such significant difference with longer contact times is in agreement with previously published literature: integrin $\alpha\beta_3$ outcompetes $\alpha_5\beta_1$ to bind Fn IBD, even on full-length Fn molecules. However, cytosolic signaling triggered by $\alpha\beta_3$ engagement contributes recruiting $\alpha_5\beta_1$ to the same position, thus reinforcing the focal adhesion over time⁵⁴. $\alpha_5\beta_1$ can properly bind Fn 9*10III, because of the location of the synergy site compared to RGD, causing stronger MLF adhesion over time.

In order to tease out the integrin role in the adhesion force, we examined multiple integrin knock out mouse fibroblasts developed by the Fassler group¹¹⁹. The “base” line, pKO, has had integrins β_2 , β_7 , β_1 , and α_v deleted. As shown in Figure 13C, pKO cells employed as a negative control develop the smallest adhesion forces and show no differences over time or across substrates. By reintroducing just integrin β_1 , pKO- β_1 cells express only integrin $\alpha_5\beta_1$ and, to a minor extent $\alpha_8\beta_1$, that can bind Fn IBD. Figure 7D illustrates how, in addition to a moderate increase in adhesion force over increasing contact times, murine fibroblasts (pKO- β_1) expressing $\alpha_5\beta_1$ generate significantly higher forces when in contact with Fn 9*10III, compounding the longer contact time effect.

Reintroducing integrin α_v into pKO cells leads to the pKO- α_v fibroblast line, expressing Fn IBD binders $\alpha\beta_3$, $\alpha\beta_5$, $\alpha\beta_6$, and $\alpha\beta_8$, although $\alpha\beta_3$ is the integrin predominantly expressed out of this group¹²⁰. Under the same experimental conditions as pKO- β_1 , pKO- α_v cells generate statistically equivalent forces whether in contact with 9-4G-10III or 9*10III (Figure 7E). This is likely due to $\alpha\beta_3$ requiring only the RGD motif for engaging Fn IBD. Moreover, it is known that single $\alpha\beta_3$ integrins bind faster and stronger to Fn⁵⁴. Hence, they outcompete

$\alpha 5\beta 1$ integrins at early timepoints. However, $\alpha 5\beta 1$ integrins alone strengthen adhesion at faster rates than $\alpha v\beta 3$ integrins. We see that when both are expressed together, their interaction strongly depends on their expression level ratio. It is plausible that the adhesion force data would not diverge at the end (i.e. at 120 seconds contact time). In addition, the rupture force distributions in Figure 7H for pKO- αv fibroblast are unaffected by the type of Fn substrate, while there exist a deceptively small difference ($\sim 6\text{pN}$) for pKO- $\beta 1$ fibroblasts (Figure 7G). This is likely due to the capability of integrin $\alpha 5\beta 1$ to form a catch bond on Fn 9*10III, but not with the distanced synergy site of Fn 9-4G-10III. The gap between the catch and no-catch bonds and the catch bond force magnitude match previous reports^{121,122}. This single molecule data also shows that $\alpha 5\beta 1$ integrins can bind to Fn when the synergy site is not available, as the rupture forces are clearly higher than of pKO fibroblasts (Figure 13D). This is matched with the cell adhesion experiment, where pKO- $\beta 1$ fibroblasts show higher adhesion than pKO fibroblasts (Figure 13C) on both fragments as well as pKO- $\beta 1$ fibroblasts induce spreading on FN9-4G-10III (Figure 12B). These results fit very well together with a paper by the Costell lab¹²³ where it was shown that $\alpha 5\beta 1$ integrins do not require the synergy site to bind to Fn and still induce rudimentary cell spreading, but to form the catch bond and for normal spreading.

The single cell force spectroscopy experiments described thus far strongly suggest that, in addition to the different adhesion forces that can be generated, fibroblasts engaging on the unfolded conformation of Fn IBD (represented by 9-4G-10III) experience downstream effects primarily due to $\alpha v\beta 3$ binding and

consequent signaling. In the next section, we will discuss the effects on select cytoplasmic signaling nodes due to the activation of the IntSw.

The activated Integrin Switch promotes cytosolic protein signaling and clustering that enhance proliferation, survival, and secretory pathways within 30 minutes

Out of the signaling nodes selected for this assay, JNK, p38, and Akt (aka Protein Kinase B) show the cleanest trends: JNK and p38 show increasing levels of (activating) phosphorylation, both over time and on Fn 9-4G-10III over 9*10III (Figure 8A). Akt phosphorylation displays a peculiar phosphorylation spike at 15 minutes since seeding. For these three proteins, the effect of the substrates became statistically significant after half an hour incubations.

Transient JNK activation promotes cell survival, while sustained activation appears to mediate apoptosis^{124,125}. Since seeded cells were washed with PBS before lysis, apoptotic fibroblasts should have been removed from the data set, restricting the JNK activation being described here as likely of the transient category. JNK has been implied in the mechanism of renal and lung fibrosis.

In a mouse model of the former (Unilateral Ureteral Obstruction), a small-molecule inhibitor protects against fibrosis by lowering myofibroblast accumulation, collagen deposition and transcript levels of TGF- β 1^{126,127}.

In pulmonary fibrosis, a different small-molecule JNK inhibitor attenuates collagen transcription, deposition, and secretion of matrix metalloprotease 7 (MMP7) in a mouse model. This molecule in a clinical trial reduced serum MMP7 levels as well¹²⁸.

JNK interacts with several fibrotic pathways, but the best described interactions are in the context of enhancing TGF- β 1 signaling. JNK can promote TGF- β 1 production through activation of AP-1, a transcription factor for TGF- β 1^{129–132}, while the latter promotes p38 and JNK activity via the TAK1 – MAPK axis¹³³. Furthermore, in renal fibrosis, JNK promotes thrombospondin-1 expression, which can activate the latent TGF β complex¹³⁰. Lastly, SMAD3 linker region is a substrate for JNK^{128,134}. Phosphorylated SMAD3 complexes with SMAD2 and translocates in the nucleus to upregulated TGF β downstream genes.

These data indicate that JNK plays a role in the fibrosis mechanisms, thus the higher phosphorylation of JNK on fibroblasts seeded on 9-4G-10III suggest those cells are being pushed towards a myofibroblastic phenotype.

Since activated fibroblasts are, among other markers, defined by their increased contractility, CREB represent as signaling node worth investigating. CREB family proteins are well-characterized Protein Kinase A substrates, with PKA being recognized as an effector of cell mechanotransduction and migration that is modulated by actomyosin contractility^{135–138}. Among PKA targets, CDC42 interacting protein 4 (CIP4) coordinates membrane deformation and actin polymerization¹³⁹. CREB (Figure 8A) belongs to a group of the basic leucine zipper (bZIP) superfamily transcription factors that bind to the cAMP response element (CRE) in the promoter region of target genes and initiate genes transcription, thereby regulating cell differentiation, proliferation, apoptosis, metabolism¹³⁹.

The middle subplot (Figure 8A) shows an increase in p38 activation as the incubation time increases, but once more this trend is significantly aggrandized for naïve fibroblasts seeded on 9-4G-10III. It has been established that P38 is

downstream of cytoskeleton-modulating kinases, such as ROCK87 and PKC88, or the small GTPase CDC42¹⁴⁰. More importantly for this work, p38 induces senescence-associated secretory phenotype (SASP) in fibroblasts thanks to transcriptional activity by NF- κ B¹⁴¹. Although in the context of lung cancer, fibroblasts with this secretory phenotype contribute to preparing the tumor niche by expressing hyaluronan^{142,143}. It has been reported that HA can further stimulate fibroblasts activation¹⁴⁴ in ex vivo conditions, although others do not report this effect in simplified in vitro systems¹⁴⁵.

Another kinase downstream of TGF- β 1, Akt, shows increased activation in 9-4G-10III (rightmost panel, Figure 8A). Unlike the previous kinases described above, Akt phosphorylation peaks at 15 minutes incubation time, suggesting a transient signaling boost that involves several pathways. Specifically, inhibiting phosphorylation of the S473 (the one we analyzed) inhibits human myofibroblast differentiation of normal and idiopathic pulmonary fibrotic (IPF) fibroblasts¹⁴⁶.

To summarize, IntSw does not cause divergent fibroblast signaling at this stage, but it shows upregulation of signaling effectors and targets due to predominant engagement of α v β 3, thus reinforcing the relevance of the IntSw effects without confounding, overwhelming effects that could be present in in vitro assays or at the organism level. Besides phosphorylation states, examining proteins that aggregate to α v β 3- or α 5 β 1-dominant focal adhesions could shed some light on the IntSw effects in the short term.

Mass spectroscopy analysis of the proteins clustering around nascent focal adhesions uncovers proteins that are enriched exclusively on one Fn fragment. In Figure 8B, those proteins cluster appear on $\pm 45^\circ$ directions, because of the

approximation, necessary to compute the fold-change. Proteins appearing only in one Fn fragment set, with zero Peptide Spectral Matches (PSM) on the other, had that zero changed to 0.1 to avoid division by zero. The upper cluster represents proteins exclusively enriched in the adhesome of CCL210 lung fibroblasts incubated on Fn 9-4G-10III, with integrin $\alpha\beta3$ dominating, while the lower cluster represents the proteins enriched on 9*10III, that enables integrin $\alpha5\beta1$ engagement.

Among the former cluster, Integrin-Linked Kinase (ILK), Collagen XIIa and tubulin $\beta3$ are of particular interest. The former has been documented in lung and kidney fibrosis^{147,148}, supporting our hypothesis that the IntSw activation pushes fibroblasts towards a myofibroblastic phenotype. This fibrillar collagen isotype typically is associated with Collagen I fibers assembled in the extracellular space¹⁴⁹. Its interactions with the $\alpha\beta3$ are completely novel, to the best of my ability. A very recent metanalysis associates it with focal adhesion and Akt signaling pathways¹⁵⁰, improperly so, because the authors use patient data on COL12A1 proximal alleles likely to be damaged or modified in colorectal cancer in order to populate KEGG (expressed) protein interaction pathways. Thus, it is plausible that already synthesized Collagen XIIa is secreted upon $\alpha\beta3$ -dominant adhesion and signaling, as part of a myofibroblast-like ECM secretion and assembly effort. Given the relatively short incubation (30 minutes), it can be safely excluded that the detected Collagen XIIa peptides were translated and synthesized in response to $\alpha\beta3$ engagement.

The exclusive enrichment of tubulin $\beta3$ in Fn 9-4G-10III samples suggests involvement of intermediate filaments in the change in morphology that lung

fibroblasts undergo when the Integrin Switch is activated (promoting progression towards an activated fibroblast phenotype).

Among the proteins exclusively enriched on 9-4G-10III we found both RAP1B and Ras Like Proto-Oncogene A (RALA). The former belongs to the RAS-like small GTP-binding protein superfamily that regulates multiple cellular processes including cell adhesion and growth and differentiation. RAP1B protein localizes to cellular membranes and has been shown to regulate integrin-mediated cell signaling and partakes in Akt signaling, which typically leads to apoptosis resistance¹⁵¹. RALA is considered of downstream of PI3K/Akt signaling in the context of insulin metabolism¹⁵². Remarkably, Akt activity is significantly increased when MLFs are plated on 9-4G-10III, as we have shown in Figure 8A.

On the other hand, among proteins that appear only in the Fn 9*10III clusters, alpha-actinin stands out. The field describes its involvement specifically with mature focal adhesions¹⁵³. This finding also agrees with the literature and the findings reported in the single cell force spectroscopy section, because integrin $\alpha 5 \beta 1$ is required to strengthen focal adhesion and is recruited by $\alpha \nu \beta 3$ over time in cells that bind Fn^{54,123}. Predominant integrin $\alpha 5 \beta 1$ engagement, whether due to an engineered Fn fragment or recruitment via $\alpha \nu \beta 3$, leads to development of mature focal adhesions.

Despite finding well-known proteins or novel interactions, an unbiased analysis of this rich MS dataset is necessary. We used an unsupervised, bidirectional statistical analysis to map the changes of the Fn 9-4G-10III over 9*10III adhesomes into KEGG pathways (Figure 8C). The topical “COVID-19” pathway should not come as a surprise, since lung fibrosis complications have been

well-characterized in many survivors. Those include fibrotic changes detectable via CT scan in up to 65% of survivors, focal fibroproliferative diffuse alveolar damage, and end-stage fibrosis expression patterns, as measured via single cell RNAseq¹⁵⁴.

Other pathways that were enriched in cells incubated over 9-4G-10III include “focal adhesions” and “ECM-receptor interactions”. These data further support that activation of the IntSw can drive fibroblast differentiation towards a contractile and secretory phenotype at 30 minutes.

Transcriptome of fibroblasts engaging the activated Integrin Switch significantly diverges from baseline at 24 hours

To better understand the potential genomic impacts of the integrin switch, we utilized RNA-sequencing to evaluate the transcriptome of naïve, primary fibroblasts seeded on Fn fragments biased towards either $\alpha v\beta 3$ (9-4G-10III) or $\alpha 5\beta 1$ (9*10III) integrin binding.

Briefly, pulmonary fibroblasts were isolated from C57/BL6 mice and expanded on TCPS for ~1 week and subsequently moved to soft (5 kPa), gelatin-coated hydrogels for 2 weeks. After generating mechanically “naïve” fibroblasts, these cells were then seeded on soft hydrogels coated with 4G, 9*10 fragments, or an equal proportion mixture of the two (50:50) for 24 hours, then the RNA was collected (Figure 9A).

Globally, RNAseq identified a staggering 9,551 genes with significantly different expression levels (DEGs) between fibroblasts seeded on 9*10 vs. 4G fragments (Figure 9B). Within this cohort of DEGs, we noted little to no bias towards either upregulation or downregulation. To identify potential cellular processes that underly phenotypic changes associated with the integrin switch, we

performed gene set enrichment analysis (GSEA) among the DEGs (Figure 9C). Among enriched gene families were several gene sets associated with survival/apoptosis (PI3K-Akt/MAPK signaling), mechanotransduction (Focal adhesion, Regulation of actin cytoskeleton), and myofibroblast differentiation (Hippo/FoxO signaling). Enrichment of gene sets ascribed to various cancers is also noteworthy as ECM remodeling/stiffening is a hallmark of the tumor microenvironment. This analysis confirms and extends the findings of our kinase signaling Luminex assay (Figure 8A) on the same set up but at 30' from cell seeding. Predominant integrin $\alpha\beta3$ (4G) engagement increased activity of Akt and its downstream signaling partners that are known to be involved with protein synthesis, proliferation, and apoptosis resistance.

Analogously, RNAseq identified 3,866 DEGs when comparing fibroblasts seeded on a 50:50 mixture of Fn fragments vs 9*10III, which can be considered the baseline in both comparisons. Presenting equal amounts of Fn 9-4G-10III and Fn9*10III on the substrate should push the MLFs transcripts towards an “intermediate point” between profiles of fibroblasts seeded on the activated IntSw (4G) or the off, physiological conformation (9*10). Indeed, some of the significant KEGG pathways for this comparison, in Figure 9E, match those of Figure 9C, including PI3K-Akt signaling, Rap1 signaling, Focal Adhesion.

Among individual genes, we also noted upregulation of pro-fibrotic ECM components Col1a1 and Col3a1 transcript as well as a strong downregulation of Ptg2 (COX-2) – a well-documented negative regulator of pulmonary myofibroblast differentiation – on $\alpha\beta3$ biased ECM. Upregulation of Interleukin 1 Receptor and Interleukin 6 signal transducer on 4G suggest that fibroblasts are

increasing their interleukin signaling by increasing the number of receptors. IL1, IL6, and IL33 (also upregulated) can be secreted by fibroblasts during inflammation and fibrosis, thus an increase in their receptors indicates the establishing of an almost paracrine stimulation loop. Among the genes downregulated by fibroblasts on both 4G and the 50:50 mixture there is SMAD7, one of the few SMADs that antagonizes TGF- β 1 signaling¹⁵⁵, suggesting that these fibroblasts are priming and enhancing their response to TGF- β 1, which is typically secreted in latent-complex form and accumulated on Fn fibers.

Overall, using naïve primary fibroblasts we have shown that the integrin switch is a potent extracellular cue that induces a shift towards a pro-fibrotic, pro-myofibroblastic transcriptome.

Common predicted TF for upregulated genes	Common predicted TF for downregulated genes
'EPOP'	'ARID4B'
'FAM60A'	'BTAF1'
'HMGA2'	'CXXC1'
'NELFA'	'E2F1'
'NFYA'	'FOS'
'NRF1'	'GRHL3'
'PHF8'	'HDAC2'
'PHIP'	'HELLS'
'POLR2B'	'HRAS'
'RAG2'	'INO80'
'TAF3'	'KDM5A'
'TBP'	'KLF15'
	'NCOA2'
	'SIN3A'
	'SMARCA4'
	'ZBTB2'

Table 4: Lists of transcription factors predicted to explain DEGs in our RNAseq experiment. They are common because according to BART analysis, they explain DEGs for the 4G vs 9*10 comparison as well as the 50:50 vs 9*10

DISCUSSION

In this work we have attempted to better understand the role that the Integrin Switch activation has on lung fibroblast signaling over time (seconds to 24 hours). Successfully detecting the IntSw activation in murine lungs undergoing remodeling *in vivo* indicates that this phenomenon is not an artifact potentially related to tissue sample processing. Moreover, generating a triple transgenic mouse line more susceptible to lung fibrosis (via fibroblast-specific integrin $\alpha 5$ KO) supports the theory that the IntSw effects are not solely due to heightened $\alpha \beta 3$ signaling, but also to dysregulation in $\alpha 5 \beta 1$ engagement. Thanks to independent techniques investigating different time points, it is now possible to connect the dots from differential engagement of Fn-binding integrins and large changes in fibroblasts' transcriptome. Specifically, different Fn conformations can be considered to be watershed events in signal transductions. Fibroblasts plated on the conformation-mimicking Fn substrates could have converged over time and moved towards homeostasis, but these data indicate that and describe how a simple change in integrin binding profile leads to increasingly divergent gene translation patterns⁴⁵⁶. Specifically, dominant engagement of $\alpha \beta 3$ is sufficient to promote fibroblast activation and differentiation towards myofibroblastic character.

In this context, the signaling impact of Akt (PKB) cannot be understated. To better describe the effects with recorded with this assay, we populated a hand-curated KEGG pathway map (Figure 14) by computing the log-fold change of (9-4G-10III over 9*10III) phosphorylation levels for all the proteins assayed. Figure

14 shows the stimulus from integrin engagement (independent of which heterodimer) to PI3K and the web of signal transducers promoted by Akt. Following the paths, we can discern increases in cell proliferation, survival and even generic protein expression when naïve MLFs are plated on 9-4G-10III. Using the curated pathway could become the basis for discovering other “druggable” intermediate signaling nodes in fibroproliferative diseases.

Starting from the DEGs from the RNAseq experiment, we used Binding Analysis for Regulation of Transcription (BART) to predict functional factors (including transcription factors and chromatin regulators) that regulate gene expression in mouse^{157,158}. From the set of significant transcription factors (TF) predicted to be responsible for upregulation or downregulation of genes compared to baseline (for both 4G vs 9*10 and 50:50 vs 9*10 comparisons), we examined and report (in Table 4) the ones common for both experimental comparisons. With such selection, we are able to tease out changes in phenotype that are solely due to increased $\alpha\beta 3$ binding on Fn. This new information also enabled linking integrin activity to changes in gene expression. Among the TF predicted to recapitulate upregulated DEGs is Pleckstrin Homology Domain Interacting Protein (PHIP), which is known for its role in cell proliferation through regulation of cyclin transcription and anti-apoptotic activity through Akt signaling¹⁵⁹, along with regulation of cell morphology and cytoskeletal organization. The Fn 9-4G-10III exclusive adhesome protein RAP1B is involved in PI3K/Akt pathway, which is connected to survival, anti-apoptotic gene expressions. Some of the common TFs for upregulated DEGs connect activation of the IntSw directly with IPF. For example, HMGA2 is implicated in epithelial–mesenchymal transitions (EMT)¹⁶⁰

that alveolar cells undergo in IPF²⁶ and has been correlated with increased expression of Col1a1 and alpha smooth muscle actin¹⁶¹. Other TFs that play a role in proliferation genes upregulated due to the IntSw are EPOP, commonly upregulated in human cancer¹⁶², and FAM60A, which also suppresses apoptotic genes and is downstream of the PI3K/Akt pathway¹⁶³.

On the other hand, our kinase signaling (Luminex) assay findings can be corroborated by TF analysis, outside of Akt: SIN3A, in the common TFs that predict the downregulated DEGs, has been shown to repress STA3 signaling¹⁶⁴, which is instead elevated at 30 minutes since plating on Fn 9-4G-10III.

We also acknowledge some caveats in the interpretation of our data, due to limitations of our experiments that may require future deeper investigations

The data in Figure 6 points towards accumulation of H5, due to the increase of its preferred epitope, the unfolded IBD, but also that this significant difference between E3 (anti-FnEDA isotype control) and H5 readings is not due to labeling or fluorescent dye artifacts. However, these data may suggest that the IBD is the more accessible epitope to monitor lung fibrosis compared to FnEDA, at least in *in vivo* mice, as long as the affinities of the two scFvs are comparable. It is still plausible that this performance gap might be due to E3 design and the exact amino acid sequence it was raised against. As part of the single cell spectroscopy assays, both αv and $\beta 1$ were reintroduced to create the pKO- $\alpha v/\beta 1$ cell line. The latter cells show an increase in adhesion forces as contact time increases (Figure 13B), but the differences across Fn fragments are not statistically significant, unlike the primary MLFs of Figure 7D. This discrepancy might be due to comparing primary fibroblasts and immortalized fibroblast lines, despite the experiments being

conducted on identically Fn-functionalized glass substrates. Such divergence could be exemplified by different basal expression levels of $\alpha 5\beta 1$ or $\alpha v\beta 3$ between primary and engineered lines. There are also a couple of limitations to the MS adhesome experiment described earlier. First, I was able to execute only two biological replicates (with multiple technical replicates for each Fn fragment condition). A third or fourth replicate would help cull data points that might be due to contamination, reinforce the weight of proteins that cluster only on one substrate, and balance outliers (e.g. proteins that appear to be Fn fragment specific but aren't). An overall improvement for such assay would be switching to the resource intensive BioID tag setting. As described in Chastney et al., cells that are stably transfected with mutated biotin ligase (BirA*) enable affinity purification of proximal proteins that became biotinylated, thus identifying proteins with underappreciated roles in adhesion¹⁶⁵. Lastly, RNAseq GSEA analysis (Figure 9C) returned pathways only apparently extraneous to the IntSw phenomenon, namely *Yersinia* and *Salmonella* infections. These bacteria respectively invade the host cells by engaging integrins then causing cytoskeletal remodeling, and through the injection of an array of bacterial effector molecules into the host cytoplasm that also lead to cytoskeleton remodeling^{166,167}. The IntSw activation led to differential expressions of cytoskeletal genes likely highly weighted in the above pathways.

Even without statistically comparing our RNAseq datasets with previously published studies, we can evince that several genes that define fibrosis-effector fibroblasts populations in bleomycin mouse models of lung fibrosis¹⁶⁸ are upregulated just by activating the IntSw in the substrate. Remarkably, analogous population-defining genes from human IPF patient/lung donor single-cell

RNAseq¹¹⁸ also show a similar transcriptome profile. Specifically, Col1a1, Col1a2, Eln (Elastin), ACTG2 (Actin Gamma 2, Smooth Muscle), CTHRC1 (collagen triple helix repeat containing 1), POSTN (Periostin), Sparc (Secreted Protein Acidic And Cysteine Rich) and Sparcl1, MGP (Matrix Gla Protein), Fibrillin, and Insulin/like Growth Factor are all upregulated in MLFs plated on Fn 9-4G-10III when compared to Fn 9*10III.

In conclusion, we have turned our attention to a hypothesis that explores how minute conformational changes of ECM can potentiate pro-fibrotic polarization of naïve fibroblasts. For over a decade, the field of mechanobiology has gained a broad appreciation for the role of mechanics in driving cell phenotypes. However, in pathologies such as fibrosis, that paradigm does not shed light on how the pathology initiates since healthy lung is soft/compliant, thus promoting cell quiescence/homeostasis. Furthermore, we now know that fibroblastic foci are also very soft²⁷ and would be predicted to suppress myofibroblastic polarization, yet the cells in this critical zone are actively pro-fibrotic. How fibroblasts within the foci are stimulated to adopt these pro-fibrotic phenotypes remains unknown and is likely multifaceted in nature. Certainly, epigenetic programming is at play in defining fibroblast subpopulations, but alternatively (or additionally) our data show that Fn-rich ECM can undergo a force-dependent conformational change that is capable of activating naïve resident fibroblasts to adopt a contractile, synthetic myofibroblast phenotype.

FIGURES

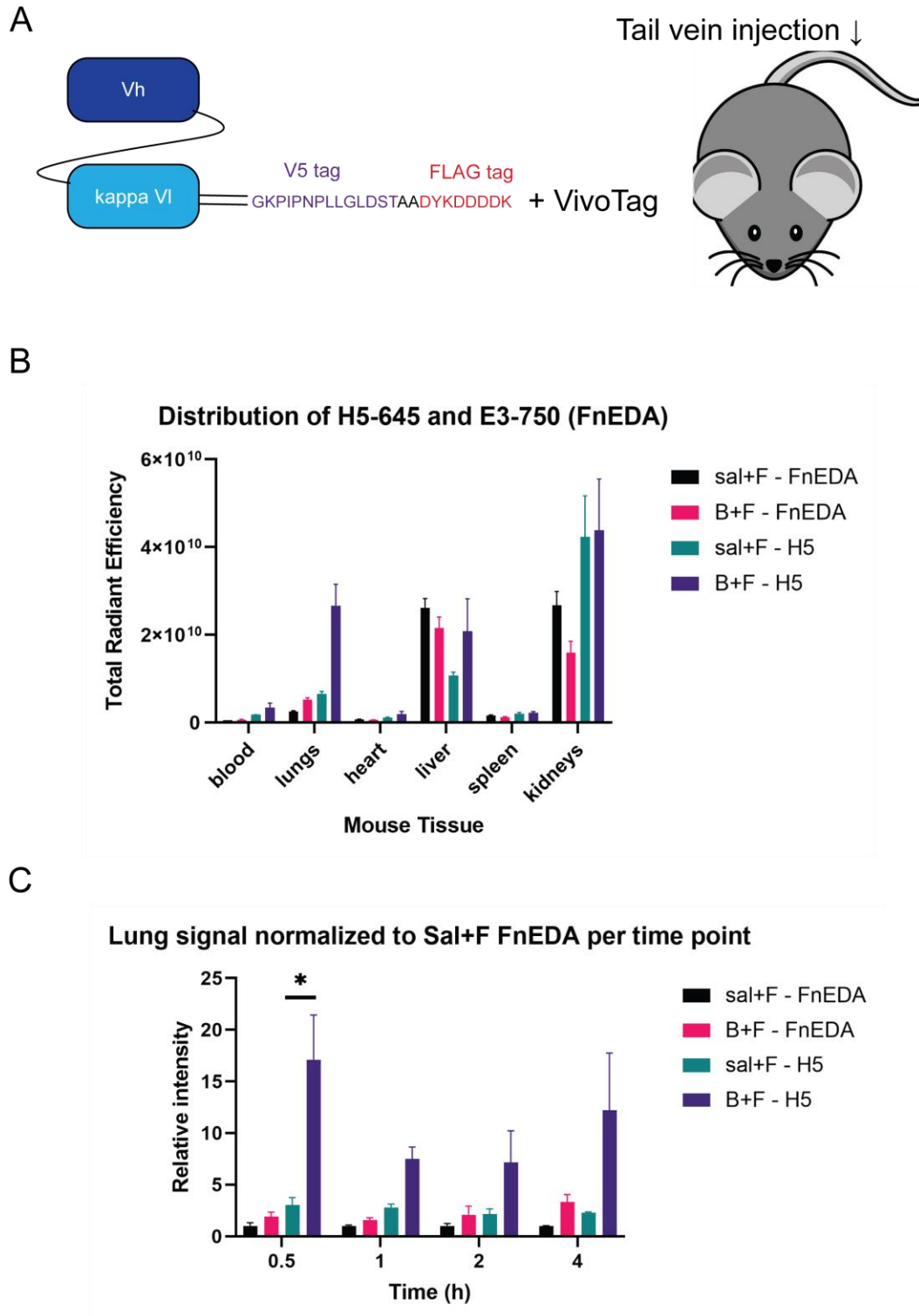


Figure 6: Fn integrin switch activation is detected by scFv and it correlates with lung fibrosis in vivo.

A) Diagram of H5 single chain fragment antibody and animal experiment. H5 has been engineered with a C-terminal V5 tag followed by a FLAG tag. The antibody was conjugated with an InVivoTag fluorophore (PerkinElmer). Male C57BL6 mice aged 8-12 weeks received an intratracheal spray of bleomycin or normal saline. For the following two weeks, the mice received three IP injections per week of fingolimond (FTY720). At Day 14, mice were injected with both H5 and E3 scFvs and imaged on an IVIS system at various time points (30 minutes, 1, 2, or 4 hours).

B) Distribution of H5 and E3 (FnEDA) scFvs. Total radiant efficiency from labeled antibodies in relevant mouse organs. Each mouse received both antibodies and was imaged at predefined timepoint in both channels, thus providing one readout per antibody. Mice were split in two groups 2 weeks before imaging, saline+F or Bleomycin+F. Mouse data points are cumulated based on treatment received at Day 0 and organ/tissue type, cumulated independently by assigned imaging time. Sal+F n=10; B+F n=8.

C) Normalized blood distribution for E3 (FnEDA) and H5 scFvs. All data points were normalized by the sal+F – FnEDA reading at 30 minutes. Relative intensity from labeled antibodies in relevant drawn blood. Each mouse received both antibodies and was imaged at the timepoints shown in both channels, thus providing one readout per antibody. Mice were split in two groups 2 weeks before imaging, saline+F or Bleomycin+F. Groups: sal+F n=2,3,3,2; B+F n=2,2,2,2 for 0.5,1,2, and 4 hours respectively. * for p-value=0.0364 determined with unpaired, one-tailed t-test with Welch's correction.

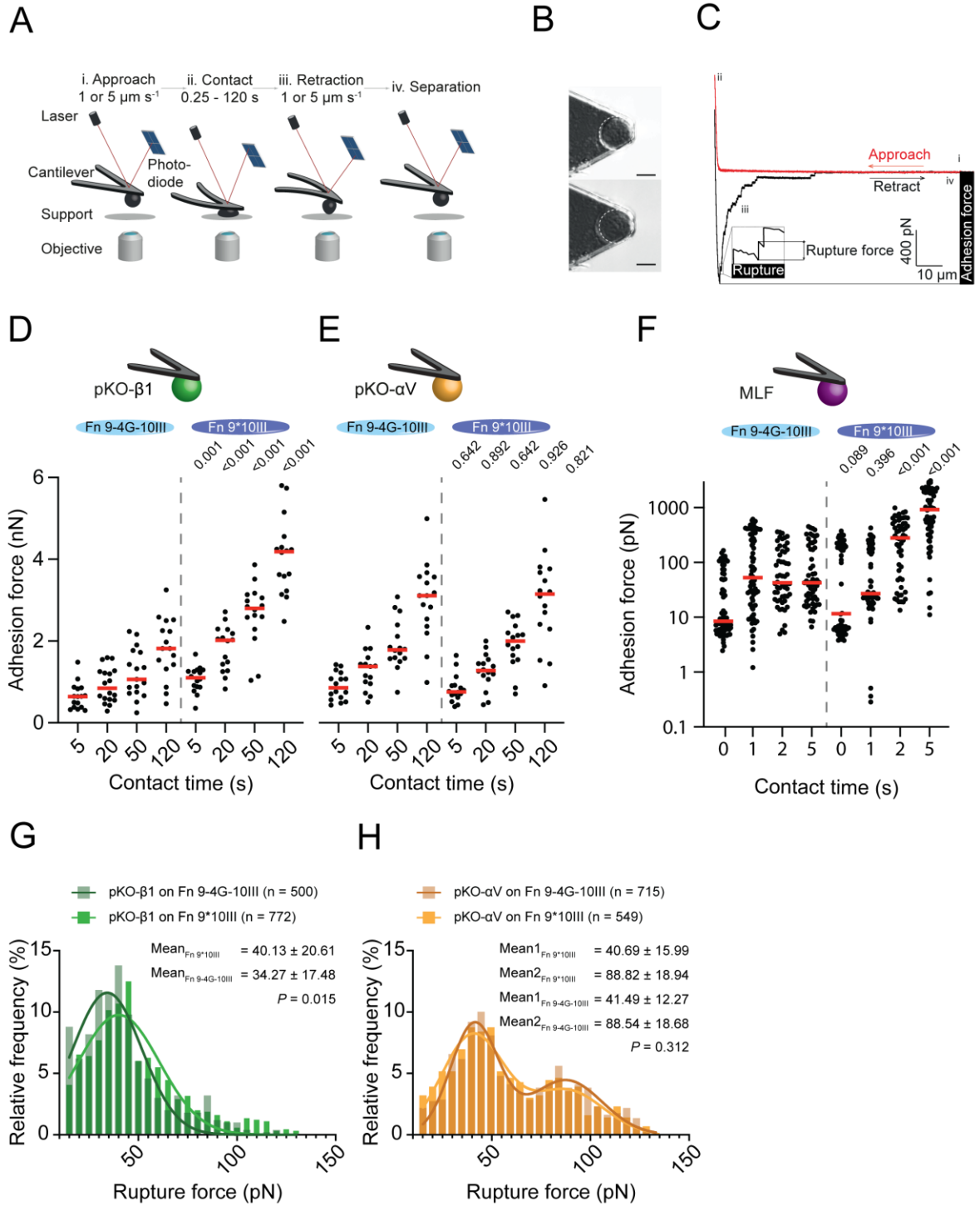


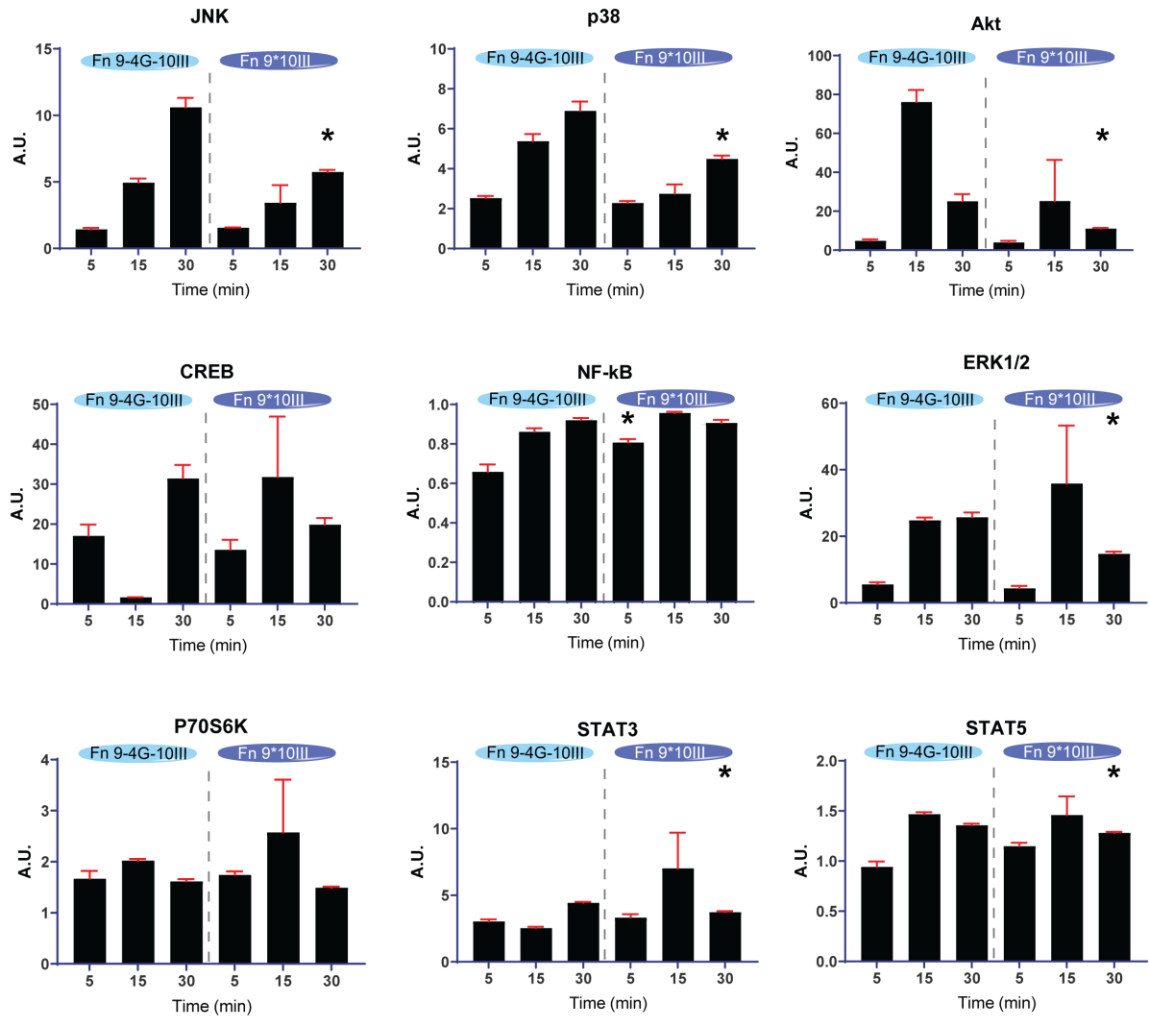
Figure 7: Integrin Switch activation favors $\alpha v \beta 3$ engagement and lowers attachment forces, below 2 minutes.

A) SCFS setup. (i) Single fibroblasts are incubated for 3-5 min on a concanavalin A-coated cantilever to assure firm attachment. (ii) Cantilever-attached fibroblasts are approached to FN-fragment (Fn 9-4G-10III or Fn 9*10III)-functionalized supports. (iii and iv) After 5 to 120 s contact time, the cantilever-bound fibroblast is retracted vertically until the fibroblast is fully detached from substrate to quantify adhesion forces between fibroblast and FN-fragments. During adhesion experiments the cantilever deflection is recorded and displayed in force-distance (FD) curves. B) (top) A single rounded fibroblast is attached to the apex of a cantilever and used for adhesion force measurements until (bottom) morphological changes (i.e. spreading) are observed. C) A representative FD curve from adhesion force measurements shows different features: the retraction FD curve (black) records the adhesion force of the fibroblast in the specific condition, which is represented by the maximum downward deflection of the cantilever. During the detachment process of the fibroblast from the substrate single receptor unbinding events are observed (ruptures). Rupture events occur when bonds between cytoskeleton-linked integrins and the FN-fragments fail. Tether events (longer plateaus) are recorded when a membrane tether extrudes from the cell body with a single or multiple integrins at its tip and occur when the integrin linkage to the actomyosin cytoskeleton is either too weak to resist the mechanical load applied, or non-existent.

Adhesion forces of pKO- $\beta 1$ mouse fibroblasts (D), pKO- αv mouse fibroblasts (E), naïve mouse lung fibroblasts (F).

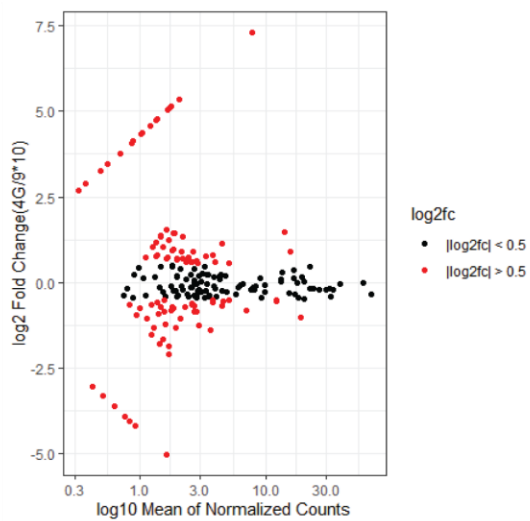
G) Rupture force distribution of single unbinding events in force-distance curves acquired with (left) pKO- $\beta 1$ and (right, H) pKO- αv fibroblasts adhering to Fn 9-4G-10III or Fn 9*10III (data taken from Fig. 2D, 2E). Force-distance curves recorded for all contact times were analyzed. Histograms were fitted using either a single gaussian function or a sum of two gaussians. The means of the gaussians and their SD are given. n gives the number of single rupture events analyzed. P values displayed in b) and c) were calculated using a two-tailed Mann-Whitney test and depict statistical differences. P values displayed in d) were calculated by extra sum-of-squares F-Test and compare whether both data sets should be fitted individually ($P < 0.05$) or with a single fit ($P > 0.05$).

A



B

Adhesome composition by PSM



C

Protein pathway analysis summary

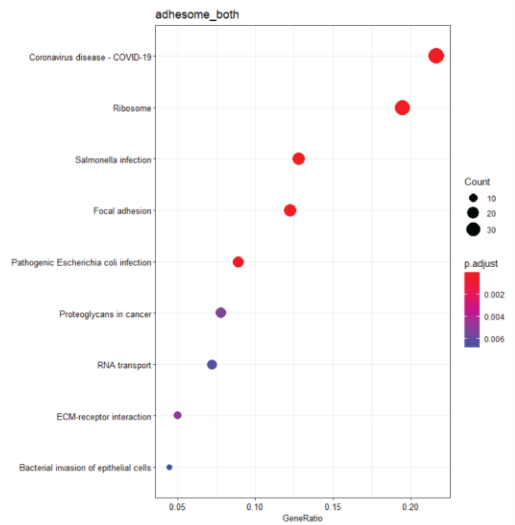


Figure 8: The Integrin Switch upregulates proliferation, survival, and secretory pathways within 30 minutes.

A) Phosphorylation levels of JNK, p38, and Akt in MLFs incubated on Fn 9-4G-10III or 9*10III for different time intervals, followed by phosphorylation levels of CREB, NF-kB, ERK1/2, P70S6K (aka S6K1/2), STAT3, and STAT5 in MLFs incubated on Fn 9-4G-10III or 9*10III on subsequent rows. Four biological replicates of at least 400'000 MLFs were used in all conditions except for 9*10III, 15 mins (2 replicates, 150'000 MLFs). Statistical significance was assessed via Mann-Whitney two-tailed test for the two substrates at each individual time point. Comparisons with p-value <0.05 are marked with an asterisk.

B) Adhesome composition by Peptide Spectral Matches, based on Fn fragment substrate. Log₂ fold change (9-4G-10III / 9*10III) versus log₁₀ of normalized counts (PSM hits). C) KEGG protein pathway analysis. Unsupervised, bidirectional analysis of the MS dataset matched to KEGG pathways. Pathways entries are arranged by the protein gene counts in the data set belonging to that pathway. GeneRatio represents ratio of number of hits belonging to that (pathway) geneset relative to the total amount of proteins collected in this data set. All enriched pathways displayed have an adjusted p-value below 0.01. Symbols are color coded from blue to red, the warmer the color the lower the adjusted p-value.

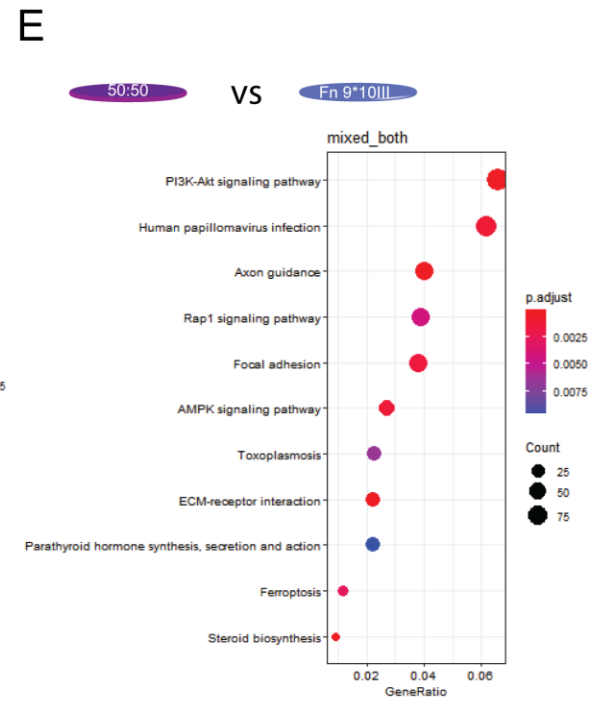
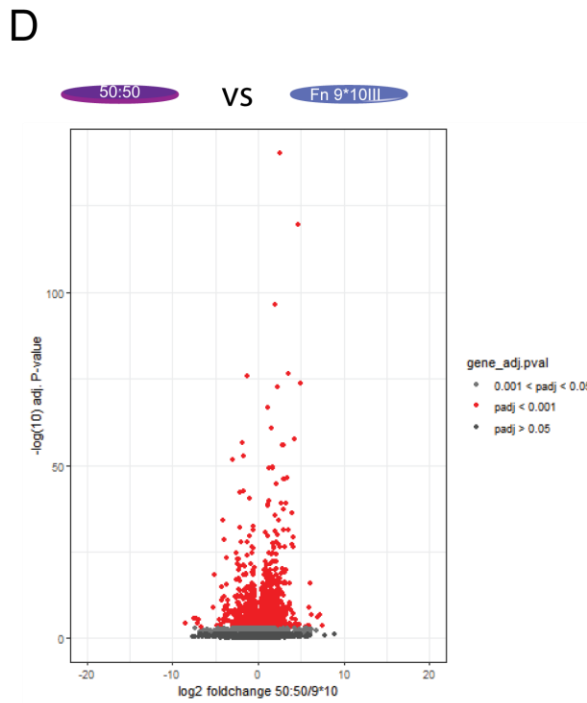
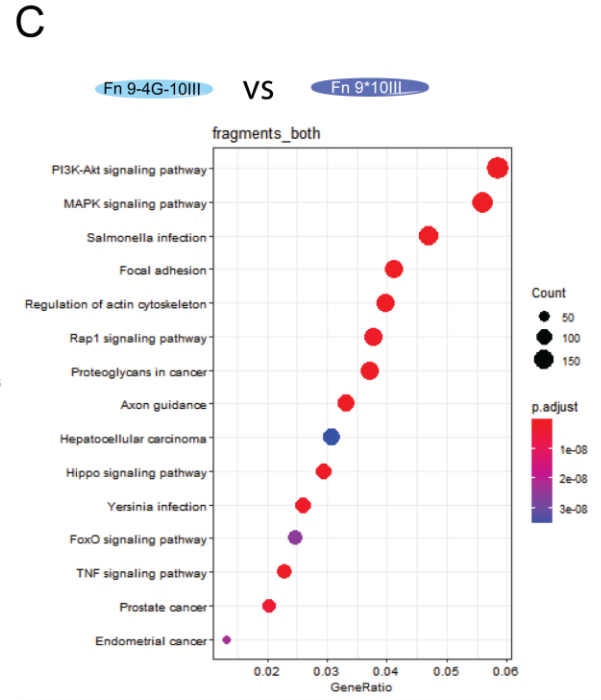
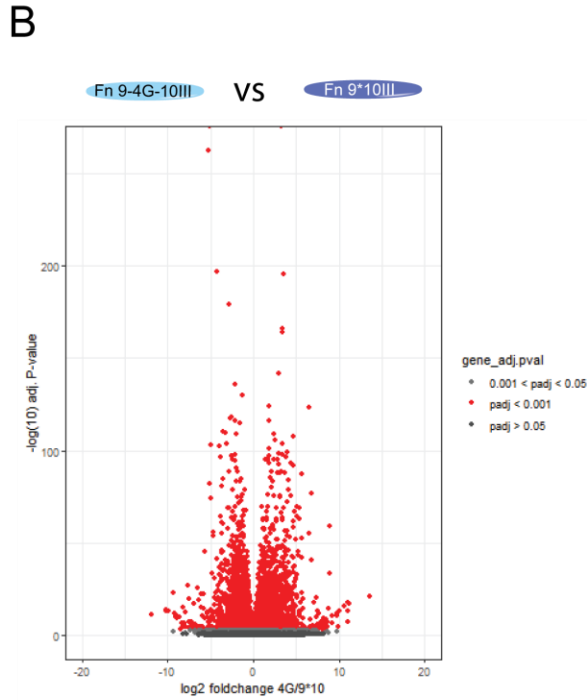
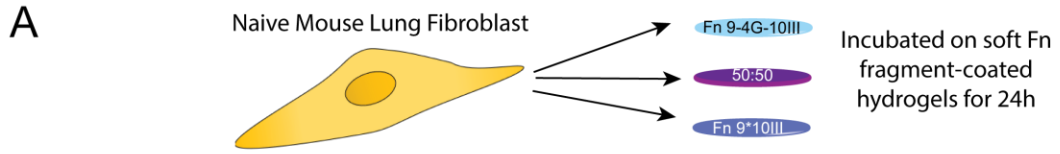


Figure 9: Activated Integrin Switch substrates upregulate mesenchymal genes at 24 h.

A) Experimental set up- Naïve mouse lung fibroblasts were plated on 5 kPa PDMS substrates coated with either Fn fragment (9-4G-10III or 9*10III) or a half and half molar ratio of the two (50:50). Cells were incubated for 24 hours in minimal serum conditions (1% FBS).

B) Volcano plot of 4G/9*10 comparison. 9594 significant differentially regulated genes were found. One dot per gene, red for adjusted p-value < 0.001

C) Pathway enrichment for 4G/9*10 substrates in both directions (upregulated and downregulated). Pathways entries are arranged by the protein gene counts in the data set belonging to that pathway. GeneRatio represents ratio of number of hits belonging to that (pathway) geneset relative to the total amount of proteins collected in this data set. Symbols are color coded from blue to red, the warmer the color the lower the adjusted p-value.

D) Volcano plot of 50:50/9*10 comparison. 3866 significant differentially regulated genes were found. One dot per gene, red for adjusted p-value < 0.001

E) Pathway enrichment for 50:50/9*10 substrates in both directions (upregulated and downregulated). Pathways entries are arranged by the protein gene counts in the data set belonging to that pathway. GeneRatio represents ratio of number of hits belonging to that (pathway) geneset relative to the total amount of proteins collected in this data set. Symbols are color coded from blue to red, the warmer the color the lower the adjusted p-value.

Blood signal normalized to Sal+F FnEDA per time point

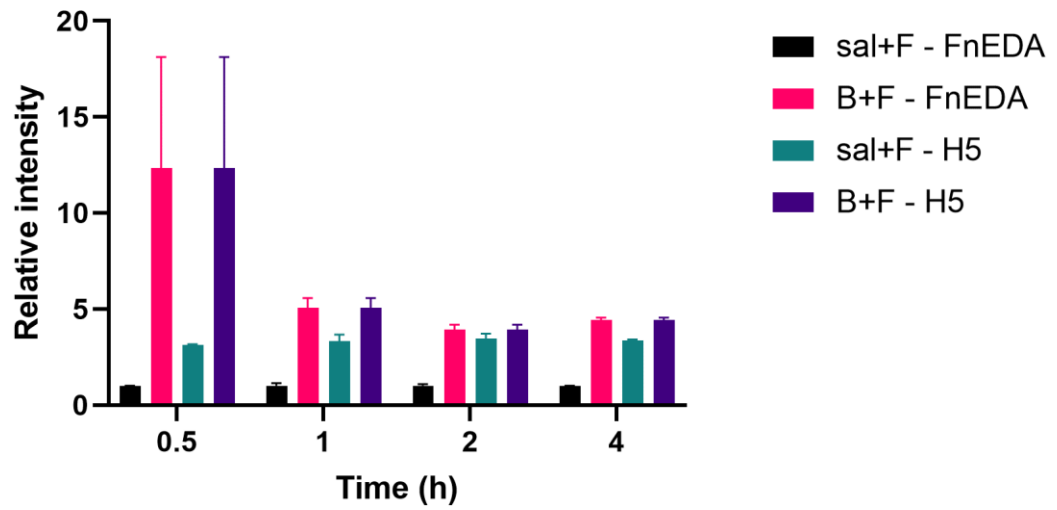
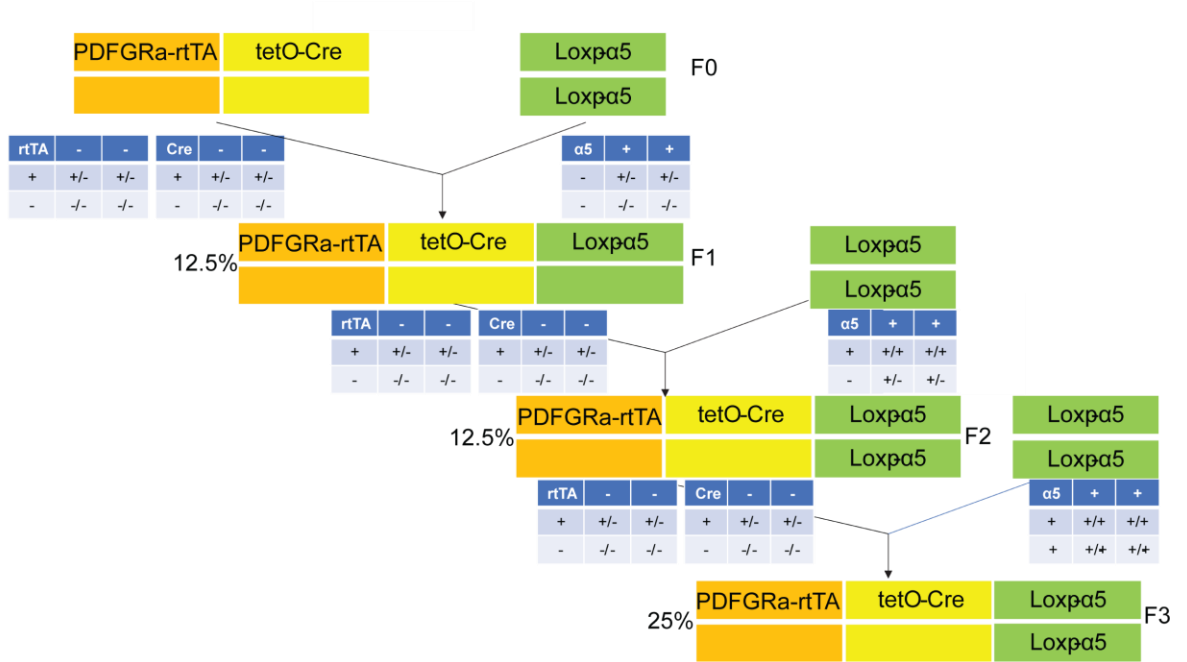
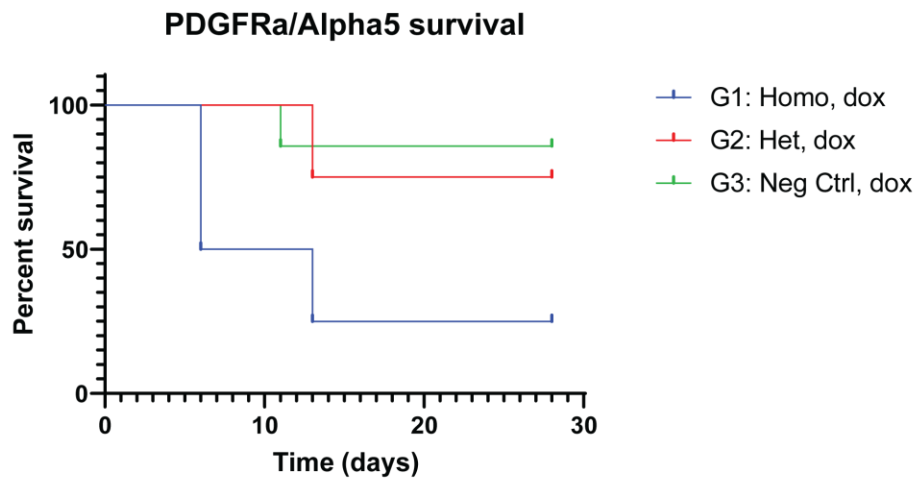


Figure 10: Normalized blood distribution for E3 (FnEDA) and H5 scFvs. All data points were normalized by the sal+F – FnEDA reading at 30 minutes. Relative intensity from labeled antibodies in relevant drawn blood. Each mouse received both antibodies and was imaged at the timepoints shown in both channels, thus providing one readout per antibody. Mice were split in two groups 2 weeks before imaging, saline+F or Bleomycin+F. Groups: sal+F n=2,3,3,2; B+F n=2,2,2,2 for 0.5,1,2, and 4 hours respectively.

A



B



Logrank test for trend p=0.0406, significant (*)

Figure 11: Loss of integrin alpha5, equivalently to activation of the Integrin Switch, significantly increases lung fibrosis mortality.

A) Breeding scheme. Alleles of interest are color-coded. Percentage of the useful offspring is reported on the side. Out of F3, statistically a quarter of the mice will be homozygous for floxed ITGA5 and have both components of the promoter system.

B) Survival of conditional integrin Alpha5 knock out mice. Groups: G1=5, G2=5, G3=8. Logrank test for trend $p=0.0406$, significant (*)

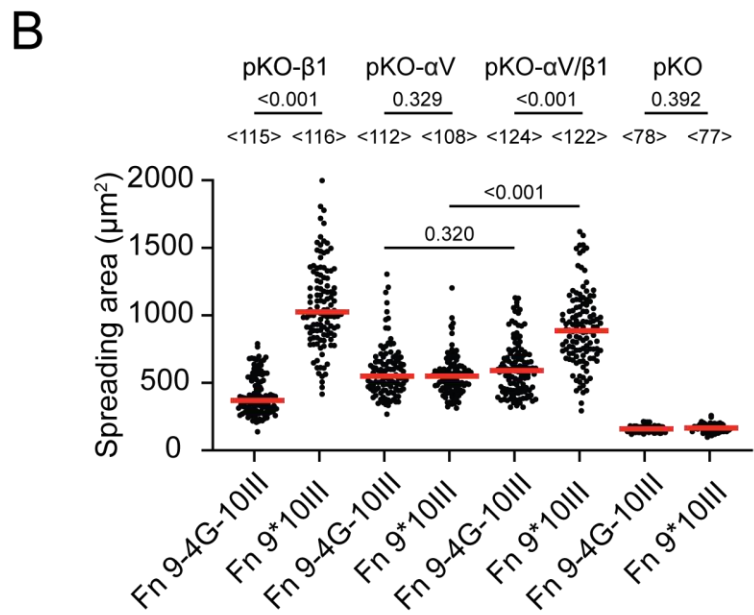
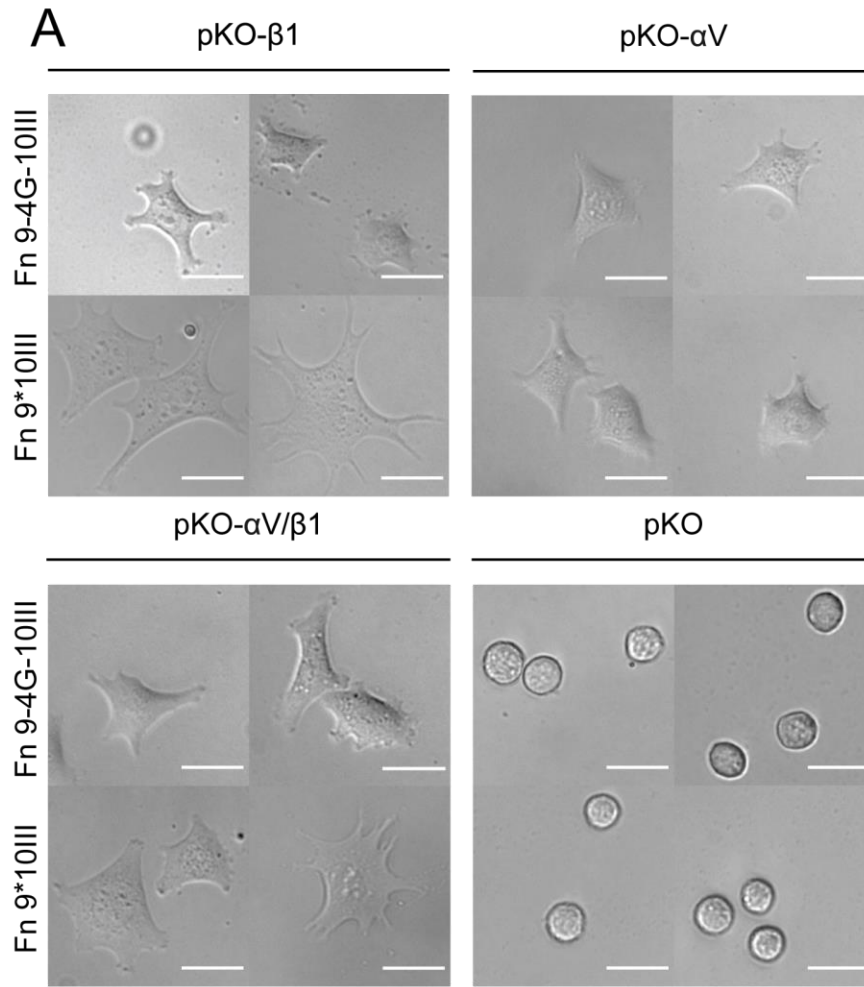


Figure 12: Fn 9-4G-10III reduces $\alpha 5\beta 1$ integrin mediated spreading of fibroblasts compared to Fn 9*10III

pKO- $\beta 1$, pKO- αV , pKO- $\alpha V/\beta 1$ or pKO fibroblasts were seeded on Fn 9-4G-10III or Fn 9*10III and allowed to spread for 60 min. A) Representative differential interference contrast microscopy images of given fibroblasts on indicated substrate. Scale bars, 25 μm . B) Spreading area of pKO- $\beta 1$, pKO- αV , pKO- $\alpha V/\beta 1$ or pKO fibroblasts on Fn 9-4G-10III or Fn 9*10III after 60 min. Dots represent the spreading area of single cells and the red bar their median. P values on bars compare indicated conditions. <n> gives the number of fibroblasts analyzed from three independent experiments

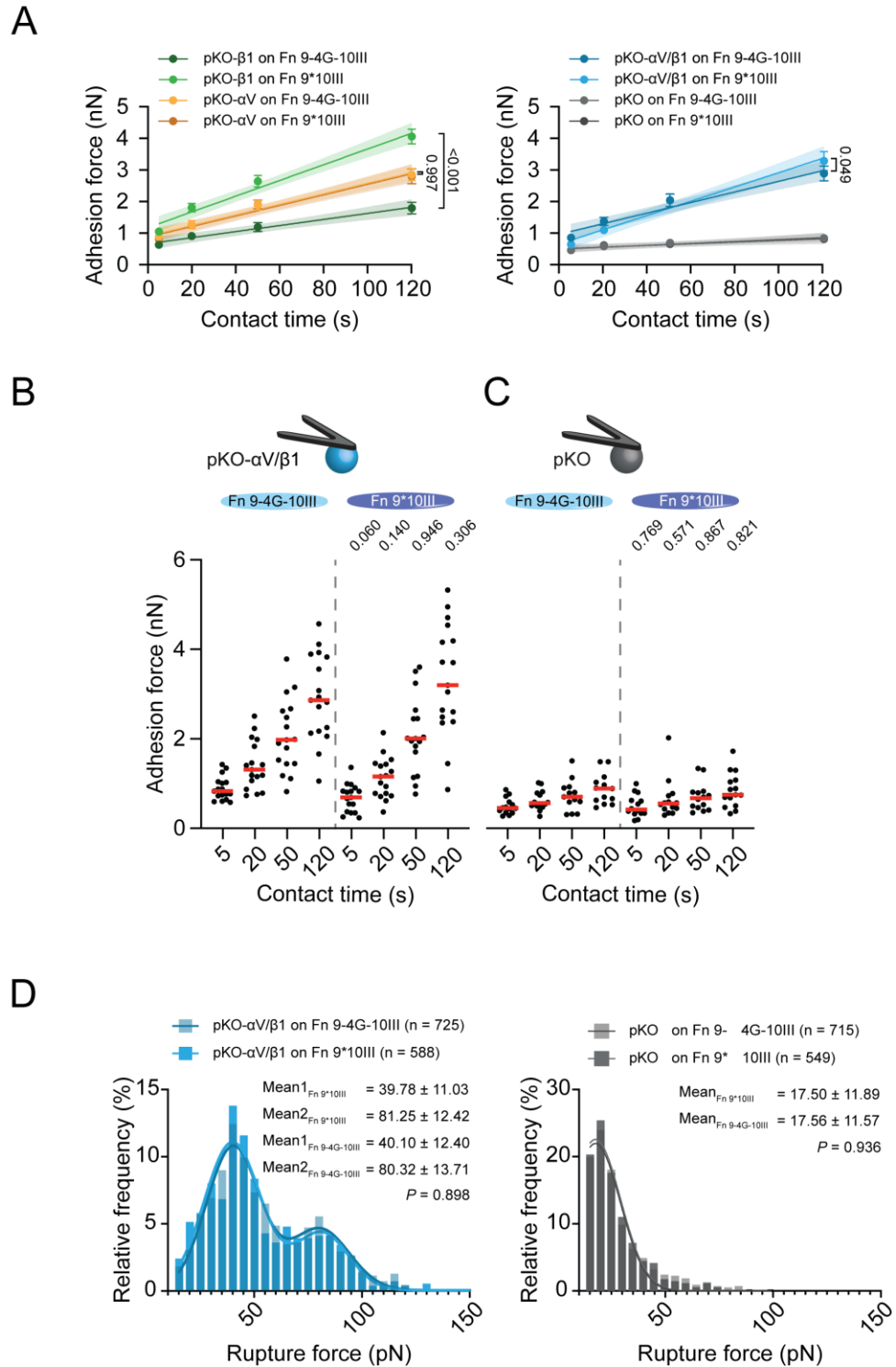


Figure 13: A) Adhesion strengthening dynamics of (left) pKO- β 1 and pKO- α V or (right) pKO- α V/ β 1 and pKO fibroblasts to Fn 9-4G-10III or Fn 9*10III are shown as linear fits (lines with 95% confidence intervals) through all adhesion forces quantified for all contact times. Dots represent mean adhesion forces for the given condition and contact time and the bars their SEM.

Adhesion forces of pKO- α V/ β 1 mouse fibroblasts (B) or pKO mouse fibroblasts (C) adhering to Fn 9-4G-10III or Fn 9*10III for given contact times. Dots are adhesion forces of single fibroblasts and the red bar their median. P values compare adhesion forces of the given cell line on Fn 9-4G-10III and Fn 9*10III.

D) Rupture force distribution of single unbinding events in FD curves acquired with (left) pKO- α V/ β 1 and (right) pKO fibroblasts adhering to Fn 9-4G-10III or Fn 9*10III (data taken from Fig. 2G,2H). FD curves recorded for all contact times were analyzed. Histograms were fitted using either a single gaussian function or a sum of two gaussians. The means of the gaussians and their SD are given. n gives the number of single rupture events analyzed. Given P values displayed were calculated by extra sum-of-squares F-Test and compare whether both data sets should be fitted individually ($P < 0.05$) or with a single fit ($P > 0.05$).

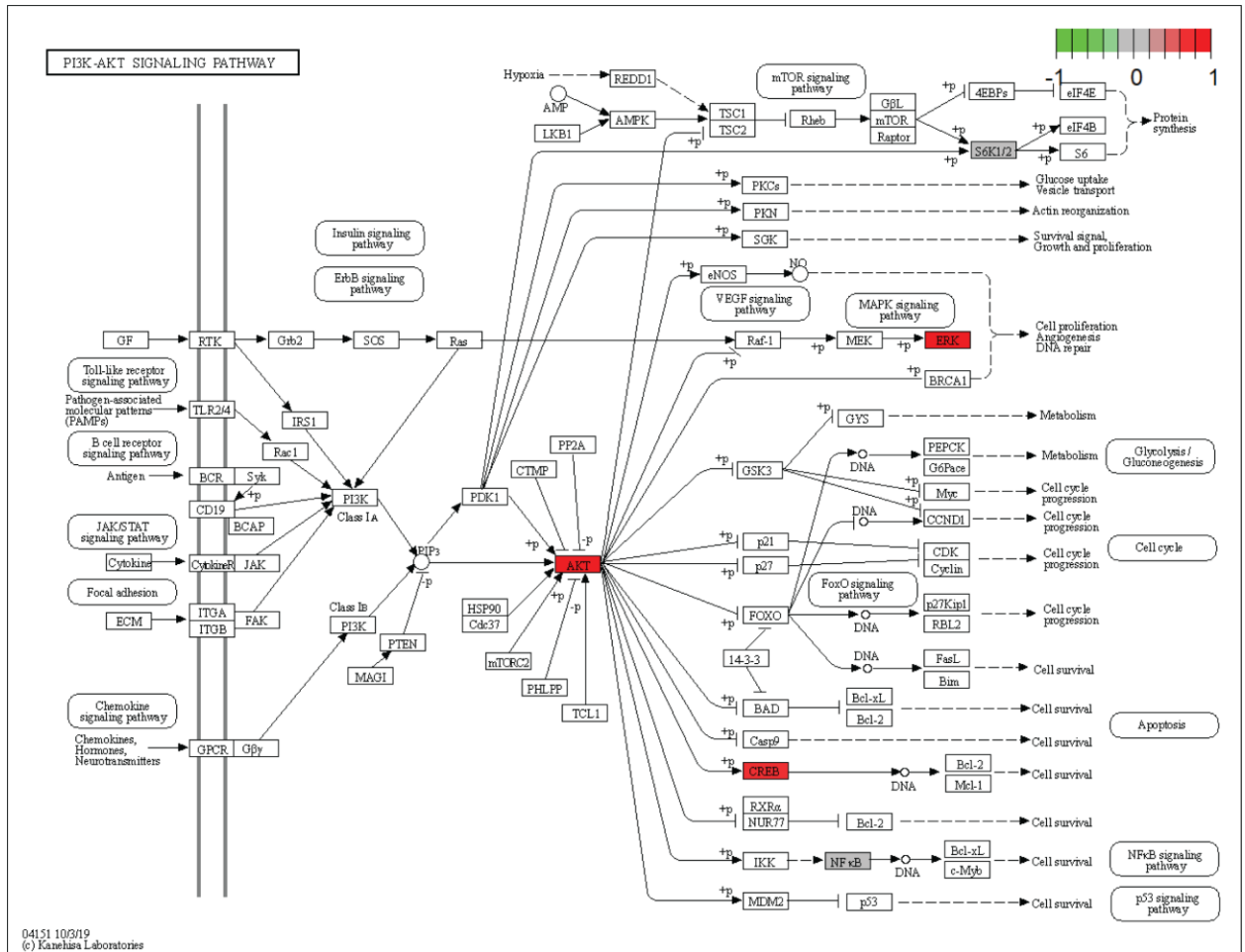
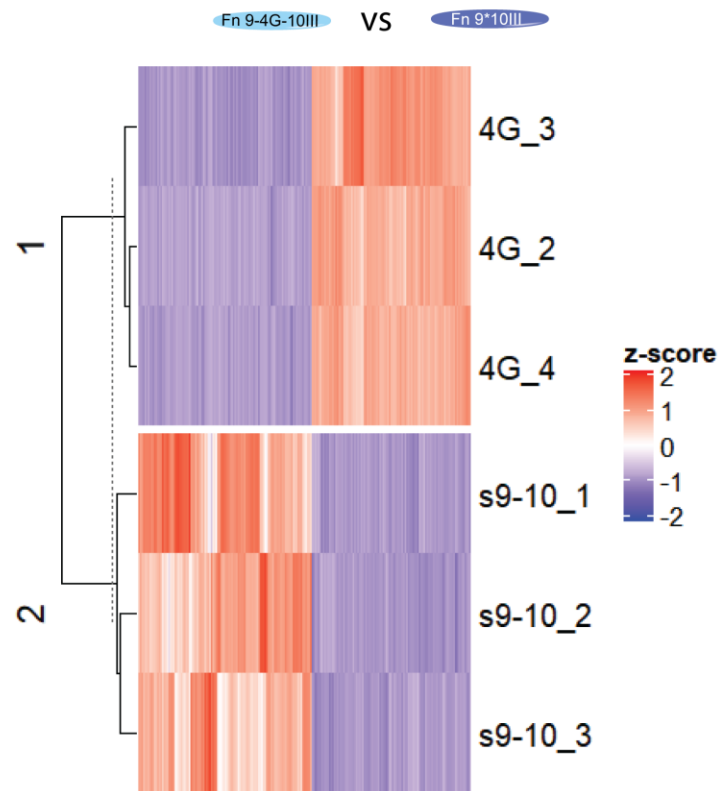


Figure 14: KEGG pathway map of Akt populated with Luminex data at 30 minutes for naïve fibroblasts on 9-4G-10III (From Figure 8A). Protein nodes with increased log-fold change activity compared to baseline (MLFs on 9*10III) are shaded in red, nodes with decreased activity are in green and little to no fold-change are shaded in grey.

A



B

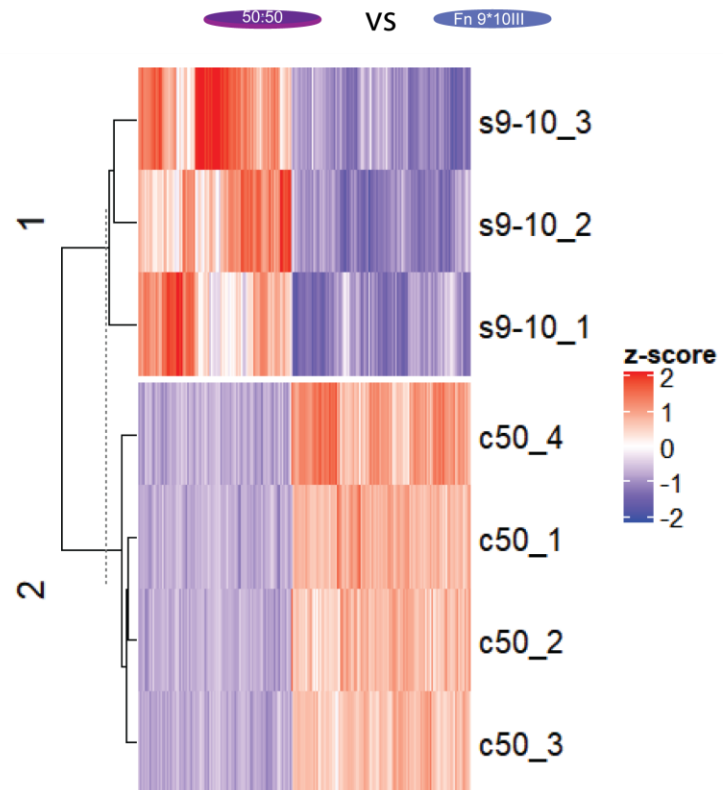


Figure 15: Bulk RNAseq heat maps for 4G/9*10 and 50:50/9*10 (data from Figure 9)

CHAPTER 3

POST TRANSLATIONAL MODIFICATIONS' ROLE IN PRIMING THE INTEGRIN SWITCH IN HUMAN LUNG DISEASES

INTRODUCTION

The findings and insights described in Chapter 2 stem from the application of several “orthogonal” (independent) investigative methods, that together describe the signaling due to activation of the IntSw from the focal adhesion, (protein level) to their impact on the mRNA transcripts after one day. A simple critique to all that work may be summarized by having conducted the experiments in vitro, i.e. using systems and substrates that are an abstraction of physiological conditions and without a host of confounding factors. Moreover, does the IntSw have any relevance in diseases outside of Usual Interstitial Pneumonia?

Those points were motivation enough for Wei Li, PhD and myself to investigate how a post translational modification (PTM) related to oxidative stress could alter mechanical properties of the Fn fiber, with particular attention to the IBD. This search owes to the work of Fernandez et al¹⁶⁹, who discovered that unpaired cysteine amino acids within the hydrophobic core of titin can undergo glutathionylation as a PTM, and such modification reversibly renders titin more prone to stretching and unfolding, significantly altering its mechanical properties.

Both in titin and Fn a group of cysteine residues are embedded in the hydrophobic core of the protein and do not contribute to any disulfide bonds. Accessing them requires a mechanical perturbation. For Fn, there exists two cryptic cysteines, one in 7III and one in 15III repeats. The former is conspicuously

close to the IBD (9III and 10III) and we detected its glutathionylation via mass spectroscopy (not shown).

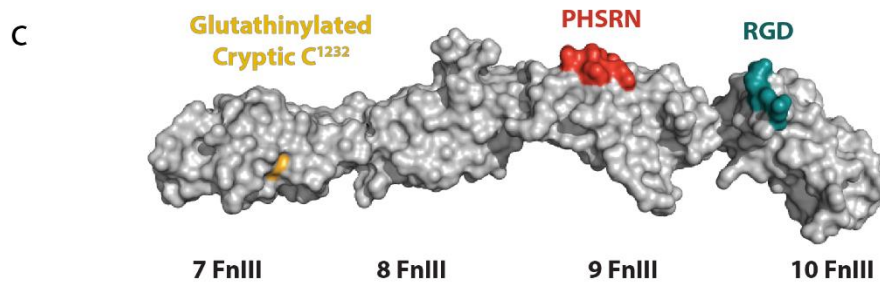


Figure 16: Crystal structure of fibronectin type III 7th – 10th repeat. Highlighted residues include the cryptic cysteine Cys1232 in the 7th repeat (yellow) as well as the PHSRN (red) and RGD (green) motifs that regulate integrin binding.

We began investigating potential changes in Fn mechanics at the single fiber level, learning that not only Fn fibers' mechanical properties are irreversibly changed after glutathionylation, but that this effect due specifically to the cryptic cysteines. Next, by using decellularized, cell derived Fn-rich matrices as fibroblast substrates, we discovered that glutathionylation causes shifts in integrin binding profiles and Myocardin Related Transcription Factor (MRTF) nuclear localization comparable or superior to changes due to physical stretching of the matrices. More importantly, glutathionylation lowers the stress/force threshold for conformational change of the IBD, by an order of magnitude.

I used phage display to screen for an antibody that would preferentially bind to glutathionylated-Fn (GluFn), in order to detect this PTM in human diseased tissues. The search for the PTM-specific antibody was unsuccessful, but I still managed to learn that instances of GluFn are significantly upregulated in some fibroproliferative lung diseases, such as lung adenocarcinoma and IPF, by using a colocalization and thresholding image analysis routine.

EXPERIMENTAL SETUP

Cell culture

Human foreskin fibroblasts (HFFs) were purchased from ATCC, passage 3 to 9 were used in all experiments. HFF cells were cultured in DMEM medium with 15% Fetal Bovine Serum (FBS) for production of cell-derived matrices, while other experiments (integrin switch and MRTF) were performed in serum free medium.

Single fiber deposition and decellularized matrix formation

All PDMS sheets were pretreated with 0.1M NaOH, 3% 3-aminopropyltriethoxysilane (APTES) and 1% glutaraldehyde before placing fiber and matrices.

Single fiber: Single Fn fibers were formed by previously described method^{16,17}. Briefly, a single Fn fiber was formed by drawing out a single fiber from a drop of Fn solution. It was deposited on striated PDMS sheets (0.005" NRV G/G 40D 12"×12") (Specialty Manufacturing Inc) fabricated by soft lithography with patterned ridges of 10×100μm and 50μm spacing. Masks (secondary modes) were made by photolithography.

Decellularized matrix: Human Foreskin Fibroblasts (HFF) cells were cultured on flat PDMS sheets (0.005" NRV G/G 40D 12"×12") (Specialty Manufacturing Inc) with a seeding density of 10,000/cm². After 7 to 9 days, HFF cells were lysed and removed with Latrunculin B (2μM) (Sigma Aldrich), EDTA (50mM) (Thermo Fisher Scientific), 2% sodium deoxycholate (DOC) and DNase I

(1U/ml) (Amresco). Afterwards, the cell derived matrices are stretched to different strain levels (0% and 200% strain). Further details are described in 31.

AFM manipulation

All force data was collected by MFP-3D Bio (Asylum Research) paired with a TiEclipse inverted optical microscope (Nikon).

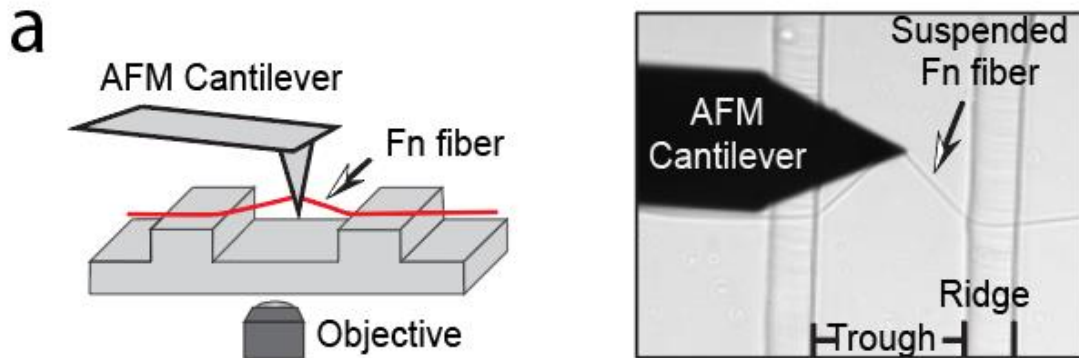


Figure 17: Schematic setup and bright field image of AFM tip pulling on single fibronectin fiber.

Single fiber mechanics: Single Fn fibers were deposited onto the striated PDMS substrate (as described before) mounted on a 50mm glass-bottomed Petri dish (FD5040-100, World Precision Instruments). Fn fibers were stretched (200%) with the underlying PDMS substrate, incubated with GSSG for glutathionylation, then relaxed to their original length. Each Fn fiber was pulled by an AFM tip (Model AC240TS-R3, Oxford instruments) with a spring constant of 2 N/m. The fiber was stretched at a rate of 320 nm/s. The strain at which the fiber breaks while pulling was reported as “extensibility”, and it is defined as $\epsilon =$

$\Delta L/L_{\text{initial}}$, where $\Delta L = L_{\text{extended}} - L_{\text{initial}}$. Young's modulus data was determined by using the incremental stress-strain curve, Young's modulus = σ/ϵ , where ϵ is the resulting strain and the applied stress $\sigma = F/A$, assuming fiber cross section is circular, $A = \pi(D/2)^2$. Fiber diameter is from AFM image with tapping mode. Details are described previously¹⁷⁰. For single fiber series pulling: The AFM tip pulled a single Fn fiber incrementally and the force was collected. After the complete relaxation, fiber was then extended (kept at 200% strain) with the AFM tip to allow GSSG (10 mM for 30 minutes) or DTT (1 mM for 40 minutes) incubation followed by relaxation and subsequent force measurement as before.

Decellularized matrix mechanics: A PDMS sheet with decellularized matrix (described in decellularized matrix above) was mounted on a 50mm glass-bottomed petri dish. Young's modulus of matrix was measured with an AFM tip (Model MLCT-O10, Bruker) with a 25 μ m polystyrene bead (Polysciences, Inc.) glued onto tip C with a spring constant of 0.01 N/m. Cantilever was calibrated by thermal method. Force indentation curve was analyzed by the Hertz model, $F = \frac{4E\sqrt{R}}{3(1-\nu^2)} \delta^{3/2}$, where E is the elastic modulus, R is the radius of the bead on the tip, δ is the indentation, and ν is the Poisson's ratio (in this experiment, 0.5). Measurements were made by indentation of 300 nm at a rate of 500 nm/s.

Immunofluorescence imaging

Imaging of Fn using H5 scFv: 48 hours before decellularization, 1 μ g/ml Alexa 555 labeled Fn was added into DMEM medium with 15% FBS which was then

assembled by cells into matrix. After decellularization, matrix was fixed with 4% paraformaldehyde and incubated in 3% Bovine Serum Albumin (BSA) in phosphate buffered saline (PBS) at room temperature for 1 hour. Then H5 (1:100) (10 $\mu\text{g}/\text{mL}$) antibody (Lab made antibody)³¹ was added to the surface of the decellularized matrix at 4°C overnight. Detection of H5 was enabled with anti-myc antibody (1:1000) (Fisher Scientific) and Alexa 647 secondary antibody (1:2000) (Thermo Fisher). Image analysis is described in³¹, briefly, ratiometric images were processed by custom Matlab code, Otsu's method was used to threshold images, signal passed threshold on both Fn and H5 channel was masked, then the ratio of fluorescence intensity of H5 and Fn were compared among different groups.

Integrin switch and MRTF: HFF cells were seeded at a density of 3,000/cm² and cultured for 2 hours on decellularized matrix in serum free DMEM medium. Cells were then fixed by 4% paraformaldehyde for 10 minutes, permeabilized by 0.2% triton-X for 5 minutes. Samples were blocked with 5% normal goat serum before primary antibody incubation (1:200) overnight at 4°C.

Primary antibody used in these experiments: active $\alpha\beta 3$ (WOW-1, gift of Sanford Shattil, University of California, San Diego), active $\beta 1$ (9EG7, BD Pharmingen), α -SMA PE conjugated (1A4, R&D Systems), anti-MKL1 (HPA030782, Sigma-Aldrich), rabbit anti-paxillin (Y113, Abcam).

All fluorescence images were imaged by a UltraView Vox Spinning Disk Confocal Microscope (PerkinElmer) (63X). Nuclei were stained with Hoechst (1:1000) (H3569, Thermo Fisher), while Alexa 488 phalloidin (1:40) (Thermo Fisher) was used for actin staining. For MRTF nuclear translocation experiment, z-stacks of 10 slices through the whole cell thickness were recorded. All image

analysis were conducted by Volocity software. In Volocity, threshold was set accordingly to different channels for all the samples, only signal above the threshold were accounted for fluorescence intensity, then fluorescence intensity ratio of two channels (vary from different experiments) was used to compare.

Human Tissue Staining

Four lung cancer cryocores were provided by the Mid-Atlantic CHTN. We received a set of lung adenocarcinoma with patient-matched healthy control, and a set of bronchoalveolar carcinoma with patient-matched healthy control as well. Sections were cut on a cryotome at 10 um thickness. After thawing, the sections were fixed in 1% PFA for 10 minutes at room temperature (RT). After one wash in 1x PBS, they were permeabilized with 0.2% TritonX-100 in PBS for 10 minutes at RT. We blocked for 1 hour at RT with 5% BSA, 5% goat serum, 5% donkey serum and mouse Fc-block according to the provided protocol. Then the following antibodies were incubated overnight at 4C in PBST with 1% BSA: rabbit pAb anti-Fn (Abcam, 1:1000 dilution, 647 channel); mouse anti-Glutathionylation (Virogen, 1:100 dilution, 555 channel).

The next day, after three washes in PBST of 10 minutes each, we incubated secondary antibodies for 1 hour at RT in PBST: goat anti-rabbit AF647 (ThermoFisher), biotinylated donkey anti-mouse (abcam). After another set of washes, we incubated Streptavidin AF555 for 1 hour at RT. We then washed and added Prolong Gold+DAPI and allowed it to cure overnight. We intentionally left channel 488 open because tissue autofluorescence would provide structural

information. DAPI in 405 channel stained cell nuclei. Slides were sealed and imaged on the same confocal microscope with the following settings:

Ch. 648: 48% laser power 400 ms exposure

Ch. 561: 37% laser power 300 ms exposure

Ch. 488: 37% laser power 200 ms exposure

Ch, 405 13% laser power 250 ms exposure

20 to 30 random 20X fields on each section were collected.

Unadulterated .tiff images were analyzed with our previously published ⁵² ratiometric Matlab routine. The median pixel-by-pixel intensity ratio outputs were then used in Prism7 to produce the plots shown.

Mutant Fibronectin

Seven million HEK293T cells (ATCC) plated in a 10 mm dish in DMEM + 10% FBS were transfected using upscaled Lipofectamine 3000 reagents (Invitrogen). Specifically, 60 μ l of lipofectamine 3000 reagent were combined with 40 μ l of P3000 and 20 μ g of mutant-Fn plasmid (kindly donated by Christopher Lemmon, Virginia Commonwealth University)¹⁰. The reagents were diluted in OptiMEM and administered to the cells according to the manufacturer protocol. Medium was replaced after 6 hours with DMEM +10% of Fn depleted FBS. Medium was collected, changed, and refrigerated every 2 days. Mutant-Fn was collected via gelatin-sepharose gravity filtration. After concentrating the eluted mutant-Fn, we obtained 250 μ l at a concentration of 3.2 mg/ml.

RESULTS AND DISCUSSION

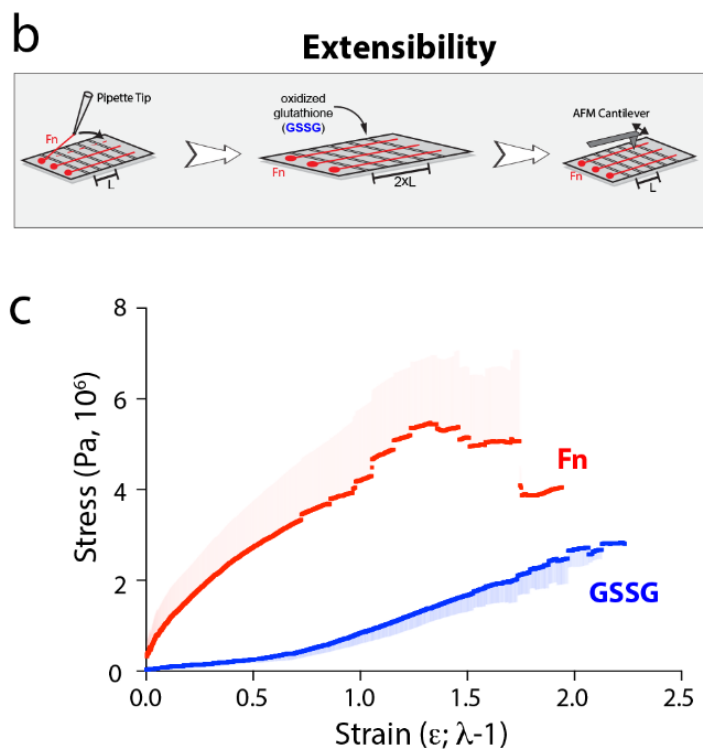


Figure 18: (B) For extensibility testing, manually-deposited fibers on PDMS were initially stretched and incubated with GSSG for glutathionylation. They were then allowed to relax to their original length followed by AFM measurement. **(C)** Stress-strain plot shows glutathionylated fibronectin fibers (Blue, Average \pm S.D.) (N=23) are more extensible and less stiff than unmodified fibronectin fibers (Red, Average \pm S.D.) (N=21).

We hypothesized that fibronectin's two sets of free cysteines are susceptible to glutathionylation. Given the cryptic nature of the reactive thiols we hypothesized that glutathionylation occurs following force/stretch-mediated unfolding of the 7th and/or 15th type III repeats. Limitations in mass spectrometry significantly prevent the specific, direct detection of glutathionylated cysteines on fibronectin from tissue samples. We therefore took a reductionist approach to further evaluate the mechanism of glutathionylation and subsequent impacts on cell-ECM biology. We first set out to evaluate the effective sites of modification in a physiologically relevant decellularized ECM (dECM). Fibroblasts were seeded on flexible silicone substrates and stimulated to produce a diverse, but fibronectin-

rich, ECM. We subsequently decellularized the samples and applied uniaxial strain to the dECM by stretching the underlying silicone. Following treatment of dECM with FITC-conjugated oxidized glutathione (GSSG), we observe strain-dependent glutathionylation of the dECM.

Given the fibronectin-rich nature of fibroblast-derived ECM *in vitro*, the modification is presumed to reside on the fibronectin backbone. In order to validate the dECM FITC-GSSG observations, we analyzed unmodified and glutathionylated dECM by bottom-up mass spectrometry. Analysis of unmodified dECM illustrates the protein diversity within dECM (not shown), but confirms the dominance of fibronectin, and to a lesser extent collagen, within cell-derived ECM. Analysis of strain-mediated glutathionylated dECM reveals only site-specific glutathionylation of the cryptic cysteine residue (Cys₁₂₃₂) within the 7th type III repeat. Although several ECM proteins were detected in the experiment, fibronectin was again identified as the predominant protein within the sample and Cys₁₂₃₂ was also the most predominant glutathionylation site (of only two sites observed across all ECM proteins). Taken together, these findings demonstrate that cryptic cysteine residues, particularly the cysteine within the 7th Type III repeat of fibronectin is a strain-dependent target of S-glutathionylation *in vitro*.

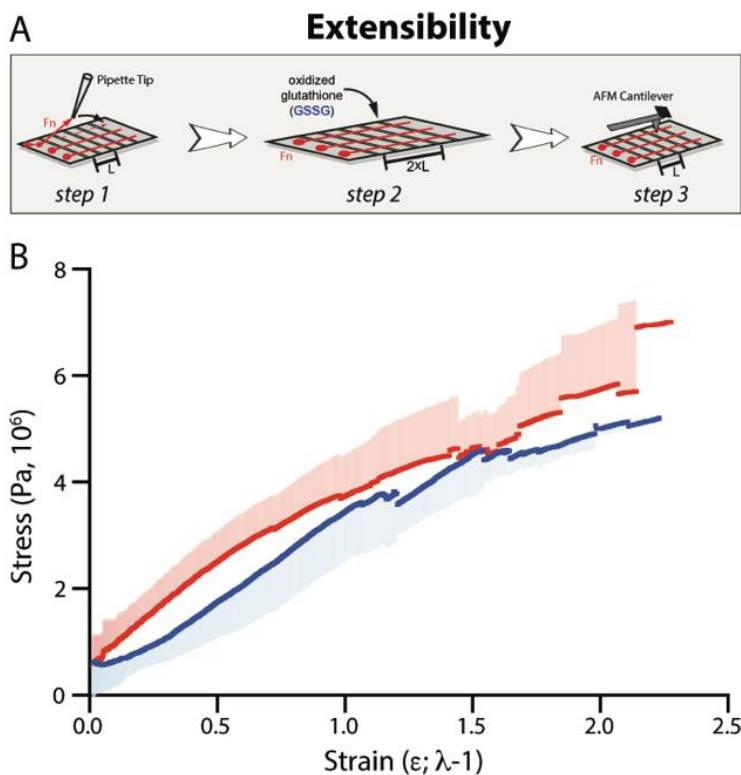


Figure 19: Cryptic cysteines in the 7th and 15th type III repeats are essential for glutathionylation impacts on fiber modulus. (A) Schematic setup and bright field image of Atomic Force Microscopy (AFM) tip pulling on single mutant fibronectin fiber. (B) Plasmids containing fibronectin cDNA with site-specific mutagenesis of the cryptic cysteines in the 7th and 15th type III repeats (Fn^{C1232A} and Fn^{C2136V}, respectively, gift from Chris Lemmon) were used to produce purified mutant fibronectin. Mutant fibronectin was used to manually deposit fiber, which were then stretched with the underlying PDMS substrate, incubated with GSSG, then relaxed to their original length followed by AFM measurement. (B) Stress-strain plot of unmodified mutant fibronectin fiber (Red) and GSSG-treated mutant fibronectin fiber (Blue). There is no significant difference in modulus between them. The shaded areas are the standard deviation of the datasets.

The glutathionylation of fibronectin's cryptic cysteine in the 7th type III repeat suggests the potential for significant structural disruption or sensitization through theoretical steric inhibition of refolding. We therefore sought to determine if and how S-glutathionylation impacts the biophysical properties of fibronectin fibers and the potential reversibility or permanence of such changes. Fibronectin predominately exists in a stabilized fibrillar form in vivo, so we manually deposited purified soluble fibronectin into single, parallel fibers onto micropatterned flexible silicone substrates to mimic this ECM form^{171,172}. This

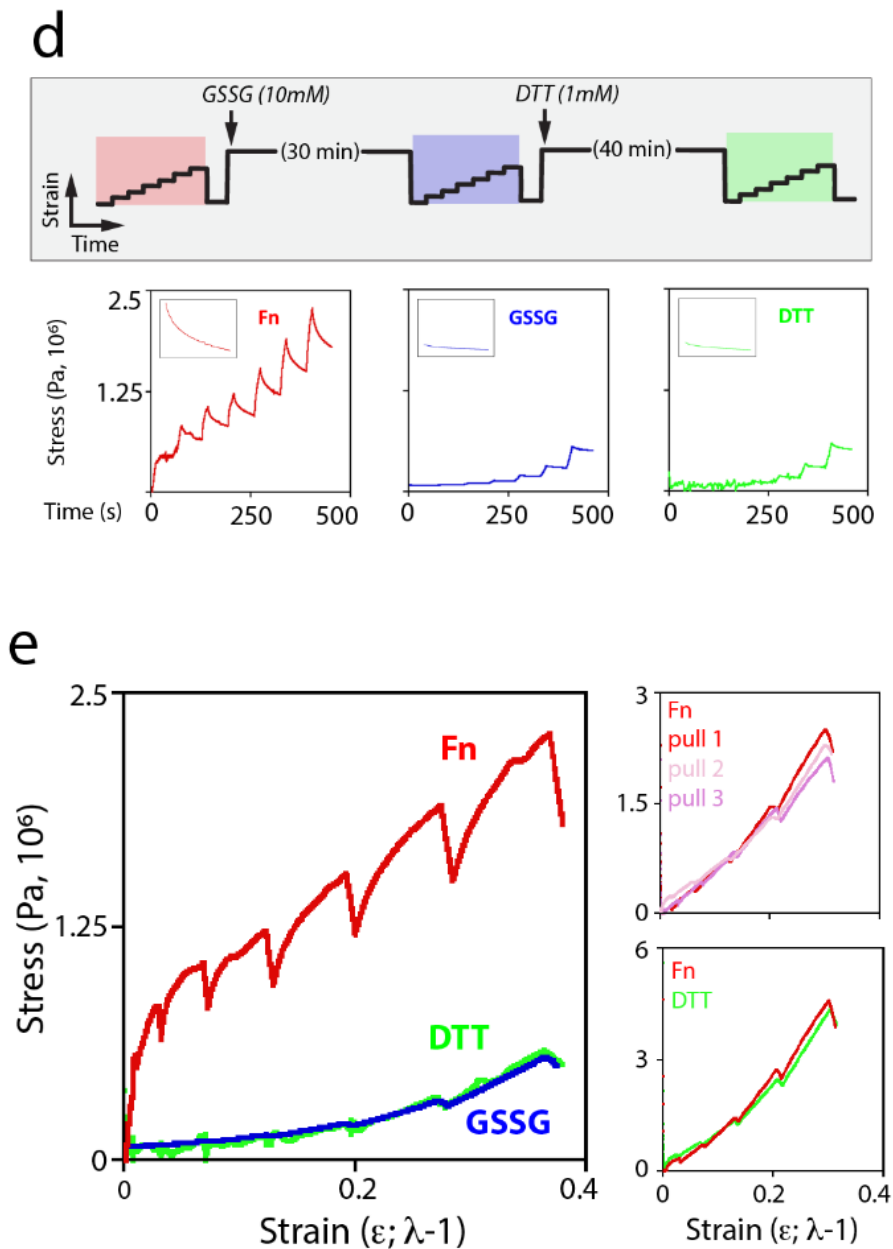


Figure 20: (D) For elasticity testing, manually deposited fibronectin fibers were instead only stretched by the AFM tip. Fibers underwent stepwise incremental extensions and force measurements, followed by complete relaxation. Fibers were then extended ($\lambda=2.0$) with the AFM tip to allow GSSG or DTT incubation followed by relaxation and subsequent elasticity measurement as before. (E) Representative plot of a full sequence (described in D) on a single fiber in stress-strain plot. It indicates that glutathionylated fibers are less stiff, a property not recovered by the removal of the glutathione. (E, upper right) The elasticity effect observed is not a function of multiple interrogations of a single fiber nor the lack of reversibility an artifact of DTT treatment (E, lower right).

format enables to use of an atomic force microscope (AFM; ¹⁷³) to both manipulate and measure the physical properties of individual fibronectin fibers and to enable

strain/extension-mediated unfolding representative of what might be encountered under physiological conditions. Fibronectin fibers exposed to GSSG under stretching conditions and then allowed to relax to their original fiber length (Figure 18) were subsequently found to be significantly more extensible and an order of magnitude less stiff than non-glutathionylated fibronectin fibers (Figure 18). Fiber breakage was observed starting at a strain value of ~ 0.8 for non-glutathionylated fibronectin fibers and nearly double that (~ 1.5) for glutathionylated fibronectin. Unmodified fibers broke more frequently at lower strain/extension compared to glutathionylated fibers, which also displayed a higher maximal strain to breakage (Figure 18).

We then utilized the AFM for both force measurement and in situ reaction conditions allowing the determination of the elasticity of a single fiber under multiple conditional states (Figure 20 **d**). Fibers underwent repetitive stepwise incremental extensions and force measurements, followed by complete relaxation to the original fiber state, in three stages. In stage one fibronectin fibers are measured in their unmodified state (red). In stage two, the fibers are extended and treated with GSSG for glutathionylation, then the stretching force is released, fibers are allowed to recover and another measurement is taken (blue). In stage three, the fiber's glutathionylation is reversed by reduction with excess dithiothreitol (DTT) under the stretched condition, the fiber is then relaxed and a final measurement is taken (green). As seen in the saw-tooth stress-strain plot (Figure 20 **e**), unmodified fiber stress sharply increases due to incremental

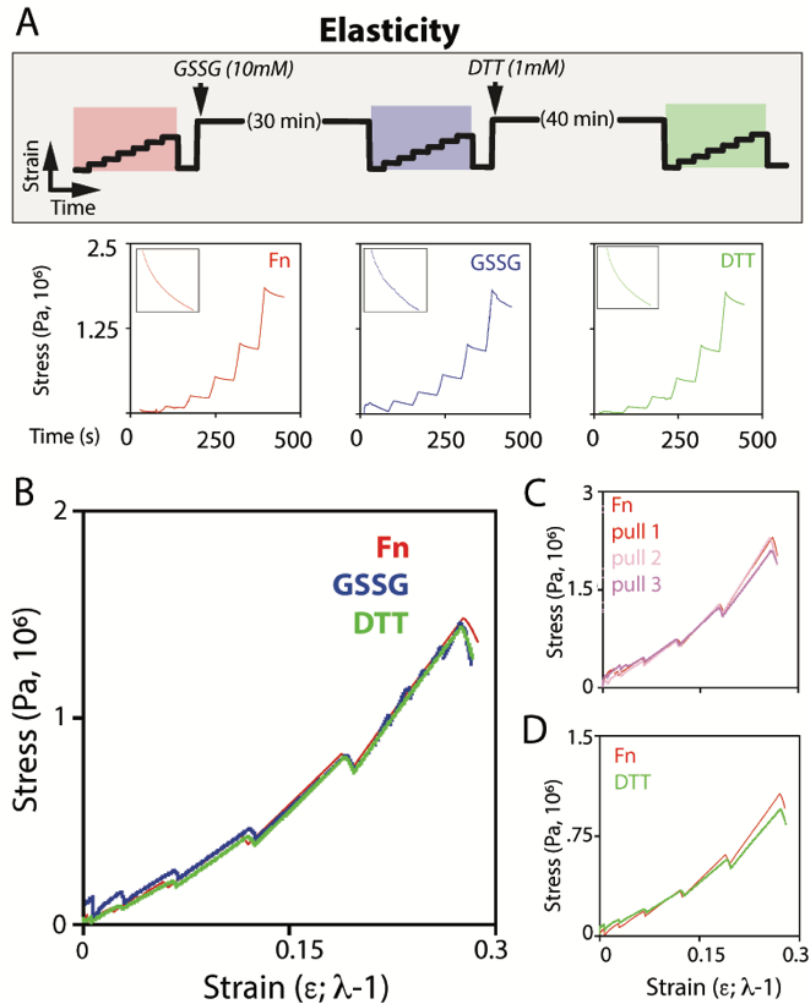


Figure 21: Cryptic cysteines in the 7th and 15th type III repeats are essential for glutathionylation impacts on fiber elasticity. Mutant fibronectin (Fn^{C1232A} and Fn^{C2136V}) fibers were manually deposited on micropatterned PDMS. (A) For elasticity testing, manually deposited fibronectin fibers were only stretched by the AFM tip. An initial stress-strain profile was established for the unmodified fiber through a series of step-wise defined strain amounts with concurrent force measurement. Following the complete series, the fiber was allowed to fully recover to its original state, followed extension to $\lambda=2.0$ with the AFM tip to allow GSSG (10mM, 30 min) incubation followed by relaxation and subsequent elasticity measurement as before. Similarly, the fiber was subsequently treated with DTT (1mM, 40 min) followed by elasticity measurement. (B) Representative plot of a full sequence on a single mutant fiber in stress-strain plot. Cysteine-modified fibronectin fibers show no response to GSSG treatment of subsequent DTT treatment. (C) The elasticity plots observed are not a function of multiple interrogations of a single mutant fiber nor DTT treatment (D).

extension followed by stress relaxation due, in part, to mechanical unfolding of domains and rehydration of the fiber. Strikingly, glutathionylated fibronectin fibers require an order of magnitude less force to achieve equivalent extension compared to non-glutathionylated fibers. Moreover, we do not observe mechanical

recovery of fibronectin fibers following removal of glutathione - a profound distinction between these and previous observations for reversible glutathionylation of Titin ¹⁷⁴. This irreversible, mechanical recording is not a function of pulling on a single fiber repetitively (Figure 20 **e**, upper right). Concerns regarding the possibility that DTT treatment of an extended fiber would reduce stabilizing disulfide bonds within fibronectin was also ruled out (Figure 20 **e**, lower right).

Consequently, these data demonstrate that strain-dependent glutathionylation of fibronectin's cryptic cysteine residues leads to an irreversible change in the fiber's biophysical behaviors. Re-stated, these data suggest that site-specific glutathionylation serves as a mechanism by which fibronectin records mechanical loading history. The cryptic cysteine residues in the 7th and 15th Type III repeats of fibronectin are absolutely essential to this unique behavior, as recombinant fibronectin displaying a cysteine-to-alanine substitution in the 7th Type III repeat and a cysteine-to-valine substitution in the 15th Type III repeat displays no response to GSSG or DTT treatment (Figure 19, Figure 21). In addition to single fiber strain-dependent reactivity with FITC-GSSG, soluble fibronectin can be glutathionylated and subsequently de-glutathionylated under heat denaturing conditions using GSSG and the reducing agent dithiothreitol (DTT), respectively.

In the intracellular environment, the effect of glutathionylation is well known and serves as a mechanism of signal transduction that mediates mitochondrial function ¹⁷⁵, receptor signaling ¹⁷⁶, and ion channel activity ¹⁷⁷. Dysregulation of intracellular S-glutathionylation can cause cell death associated

with many diseases, like cardiovascular disease and diabetes ¹⁷⁸. Although it is known that ECM biophysical properties govern the impact of oxidative stress on cells ¹⁷⁹ and that several glutathionylated extracellular proteins and cytokines are released during inflammation ¹⁸⁰⁻¹⁸², ECM responses to oxidative stress have been largely ignored. The glutathionylation of Cys1232 within fibronectin's 7th Type III repeat is a particularly interesting modification site based on its proximity to the primary binding sites for cell integrin receptors (PHSRN, a.k.a. "synergy site", and RGD) within the 9th and 10th Type III repeats (Figure 16, Figure 4). Thus, we sought to more specifically explore the impact of fibronectin glutathionylation on the integrin binding motif structure and function.

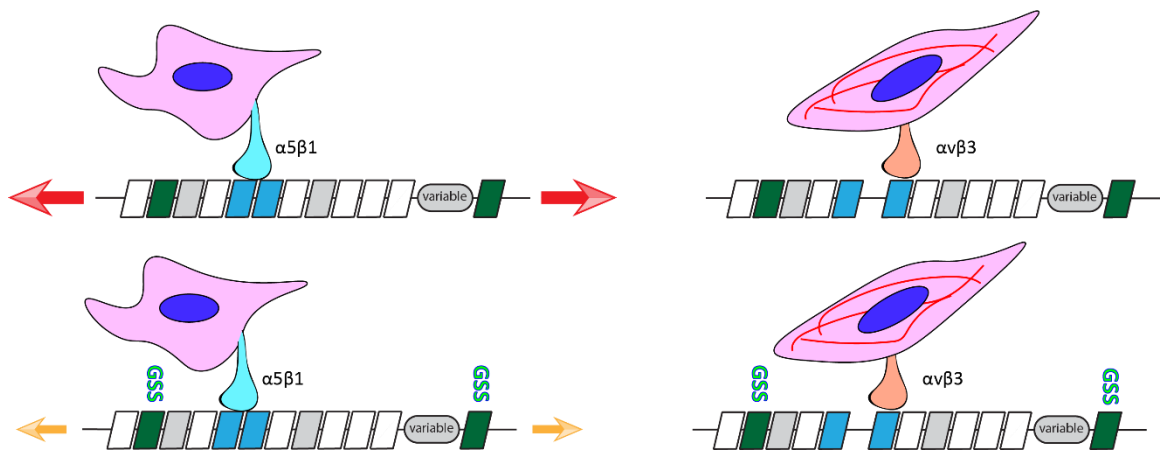


Figure 22: Glutathionylation of Fn lowers the force threshold necessary to unfold the IBD and cause the integrin switch (cartoon).

Fibronectin is one of many elastic proteins that are particularly sensitive to dynamic biophysical forces. Such forces are often generated by invading and contracting cells that induce strain, or extension/elongation of fibronectin fibers. This lengthening of fibronectin fibers is accommodated by significant conformational change in the domain structure of fibronectin that, in turn, provide a feedback stimulus to surrounding cells. Large-scale conformational changes in fibronectin regulate integrin receptor binding^{183,184}, the binding and release of growth factors^{185,186}, even its own polymerization¹⁸⁷. We've previously demonstrated that in response to cell contraction-mediated strain of fibronectin matrices, the primary cell-binding domains of fibronectin (the 9th and 10th Type III repeats) display a conformational change that directs integrin binding preference. Given the impact of glutathionylation on fibronectin fiber elasticity and the identified site of modification, we sought to measure this strain-mediated event (Figure 4), predicted by Vogel et al. nearly two decades ago¹⁸⁴ and made detectable with a single-chain antibody (clone H5) developed in our lab⁵². As before,

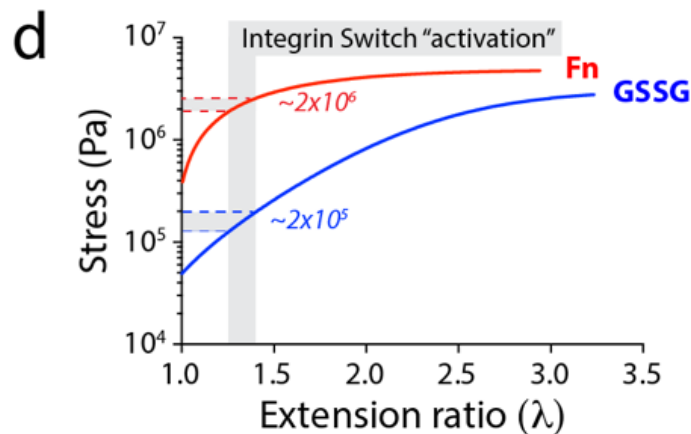


Figure 23: Glutathionylation of Fn lowers the stress (force) threshold necessary to unfold the IBD tenfold, and cause the integrin switch. The Fn IBD unfolding takes place when Fn fibers are between a 1.4 and 1.5 extension ratio.

fibroblasts were allowed to assemble a fibronectin-rich ECM on flexible silicone substrates and were subsequently removed through a decellularization process leaving a fibronectin-rich dECM. The substrates were left unstrained or extended to expose the cryptic cysteines followed by GSSG or control treatment. H5 was subsequently introduced to detect the strain-dependent conformational change in the integrin binding domain. Quantitation of the H5:total fibronectin signal ratio within ECM fibers demonstrates that this strain-dependent event is unaltered following glutathionylation, establishing the perseverance of this important fibronectin behavior. This result indicates that glutathionylation, by itself, does not disrupt previously identified strain-dependent behaviors of fibronectin. Importantly, the observed fiber-scale biophysical changes of fibronectin do not significantly impact the bulk material properties of the dECM (Supplementary Figure 7). Heterogeneous fiber alignment and porosity dominate these bulk material properties of polymer systems. So, fibronectin glutathionylation within a dECM does not confer broader changes in ECM rigidity that cells can sense.

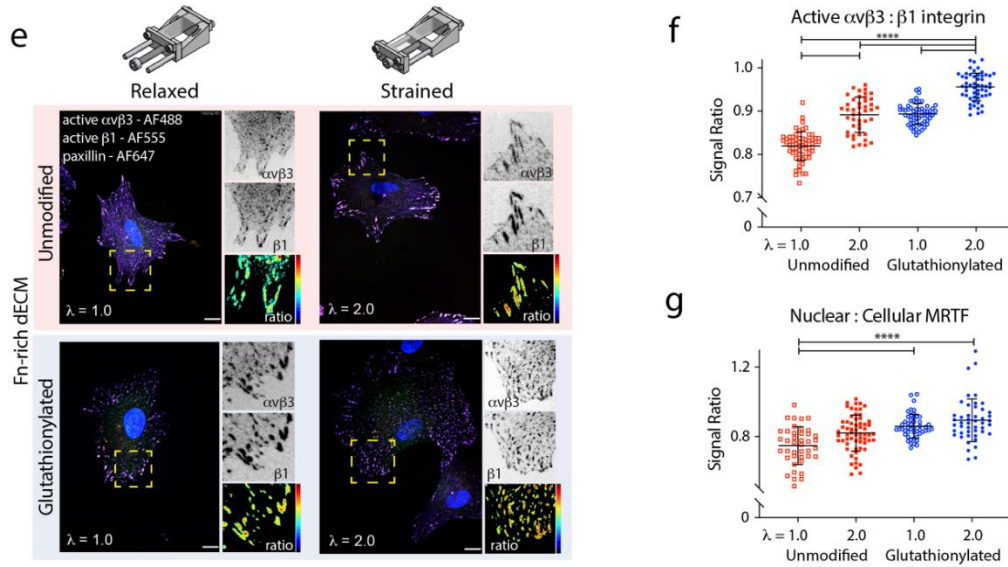


Figure 24: Glutathionylation of dECM enables integrin switch activation and MRTF nuclear translocation in naïve fibroblasts. (e) Ratiometric images and (f) quantitative analysis of active $\alpha v\beta 3$: $\beta 1$ ratios demonstrate a strong integrin switch toward $\alpha v\beta 3$ in focal adhesions of fibroblasts seeded in unstrained, glutathionylated dECM to an equivalent degree compared to dECM with manually applied strain (control; unmodified $\lambda=2.0$). Integrin switch activation was further accentuated on glutathionylated dECM that had been manually strained prior to cell seeding (N=55 for each condition) (Mean +/- S.D.). (g) Quantitative analysis of the nuclear:cytoplasmic ratio of MRTF illuminates a similar response; a strong shift toward the nuclear compartmentalization of MRTF, a strong myofibroblastic differentiation signal for fibroblasts, in unstrained, glutathionylated dECM to an equivalent degree compared to dECM with manually applied strain (control; unmodified $\lambda=2.0$). MRTF nuclear translocation was further accentuated on glutathionylated dECM that had been manually strained prior to cell seeding (N=50 for each condition) (Mean +/- S.D.). Scale bar in (A) is 12 μ m. Color scale bar is 0-0.7. Kruskal-Wallis statistical tests were employed for statistical analysis, ** P < 0.0001.**

Rather, glutathionylation only reduces the energy or force threshold required for to engage strain-dependent behaviors. In the case of the integrin binding domain's strain-dependent conformational change, which we've previously shown to be 'activated' at an extension ratio of ~ 1.4 (Strain ~ 0.4), glutathionylation lowers its activation force by an order of magnitude (Figure 23).

The balance of diverse integrins within the macromolecular complexes which form cell-matrix adhesions (i.e. focal adhesions) strongly influence cell behaviors due to alterations in focal adhesion signaling. For instance, we and others have previously demonstrated that preferential $\alpha v\beta 3$ integrin engagement

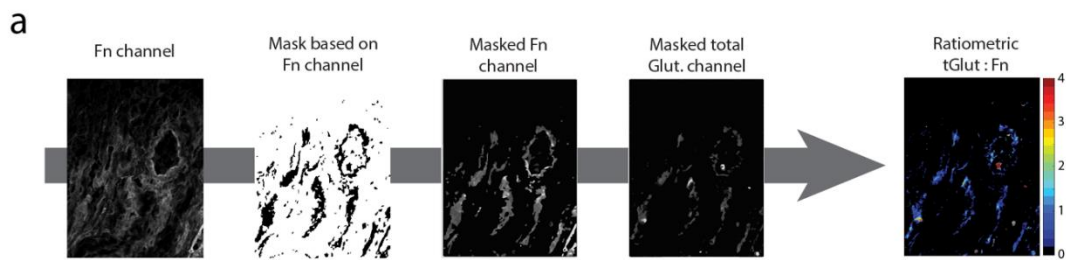


Figure 25: Step by step image analysis performed by ratiometric algorithm: the leftmost panel shows a representative 20X field of lung tissue in the Fn stain channel. A binary mask is built from this field using Otsu's thresholding method, then is applied to the Fn channel (middle panel). The mask is also applied to the anti-glutathionylation channel (fourth panel), thus accounting only for signal overlapped with Fn molecules. Then a pixel-by-pixel ratio of the intensity values between the glutathionylation and Fn channels is used to produce a ratiometric image, rightmost panel. Median ratio values for each field are used for statistical analysis.

over synergy-dependent integrins like $\alpha5\beta1$ and $\alpha3\beta1$ ¹⁸⁸ alters angiogenic programs¹⁸⁹, epithelial to mesenchymal transition (EMT)¹⁹⁰, and activation of naïve fibroblasts down a myofibroblastic lineage^{191,192}. In fibroblasts, the strain-dependent conformational change of fibronectin's integrin binding domain nearly abolishes integrin $\alpha5\beta1$'s ability to bind, thus strongly skewing focal adhesions toward an $\alpha\beta3$ character. Although we can artificially stretch fibronectin-rich ECM to activate the conformation change (Figure 24 e, top; Figure 24 f, unmodified), the impact of fibronectin glutathionylation is that naïve non-contractile (i.e. normal) fibroblasts readily trigger this integrin switch (Figure 24 e, bottom; Figure 24 f, glutathionylated $\lambda=1.0$). Ratiometric imaging and quantitation of active $\alpha\beta3$ versus active $\beta1$ within naïve fibroblast focal adhesions cultured on glutathionylated fibronectin-rich dECM demonstrates that even in the absence of artificial activation of the conformational change through substrate stretching ($\lambda=2.0$), these cells display heightened $\alpha\beta3:\beta1$ ratios (Figure 24), indicative of a true integrin 'switch'. We have shown that integrin $\alpha\beta3$ -mediated myofibroblastic differentiation occurs, in part, due to elevated cytoskeletal activity and the

concomitant conversion of globular (g) actin to filamentous (f) actin ¹⁹¹, demonstrated partly through enhanced spreading (not shown). This transition from g-actin to f-actin displaces the transcriptional co-factor MRTF (myocardin related transcription factor) from g-actin, resulting in its translocation to the nucleus where it drives myofibroblastic/mesenchymal gene expression. Concurrent with elevations in $\alpha\beta 3$ engagement, we observe a significant nuclear translocation of MRTF, demonstrating its activation (Figure 24 **g**).

Far from being a mere in vitro artifact, we explored the potential relevance of fibronectin glutathionylation in lung by analyzing patient tissue samples representing various pathologies with associations to elevated oxidant stress including lung adenocarcinoma¹⁹³⁻¹⁹⁶, bronchioalveolar carcinoma and idiopathic pulmonary fibrosis (IPF)¹⁹⁷⁻²⁰². In agreement with prior reports, we observe elevated glutathionylation within adenocarcinoma and IPF patient samples. Using previously published image processing approaches ⁵², we demonstrate strong colocalization of glutathionylation with the fibronectin fraction within adenocarcinoma and, to a lesser extent, in IPF

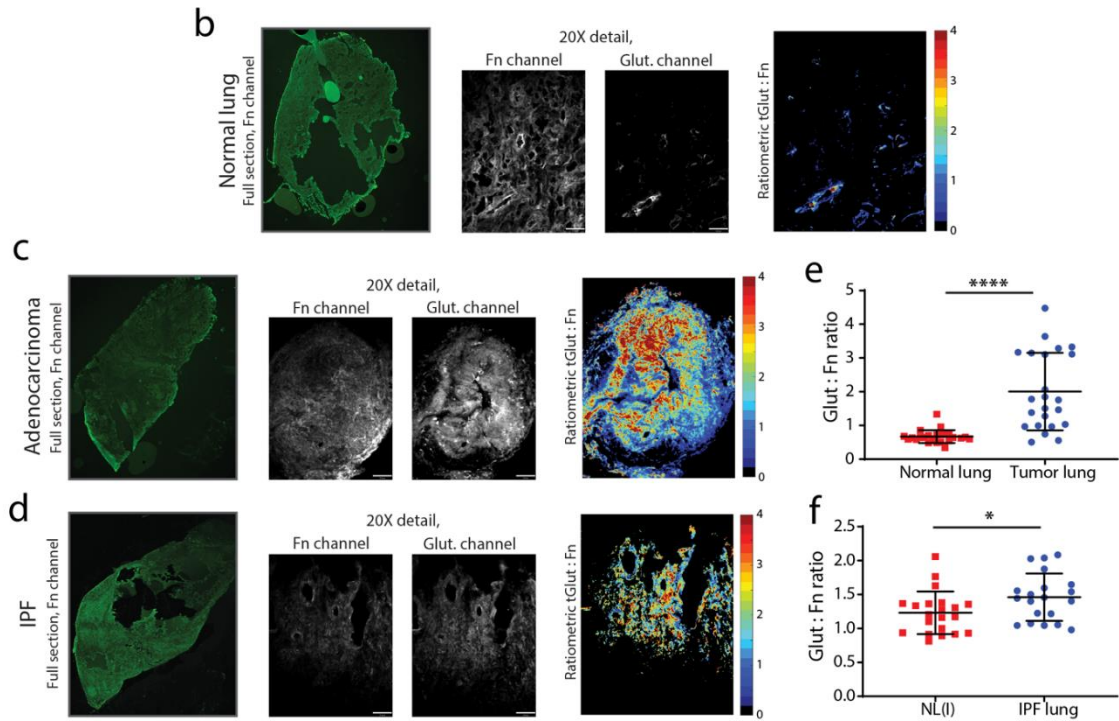


Figure 26: B Left, full section of normal lung tissue (Fn, AF647). Middle panels, 20X detail of the Fn (AF647) and glutathionylation channels (AF555), scale bar 54 μ m. Right panel, resulting ratiometric image. **C** Left, full section of lung adenocarcinoma tissue (Fn, AF488). Middle panels, 20X detail of the Fn (AF647) and glutathionylation channels (AF555), scale bar 54 μ m. Right panel, resulting ratiometric image. **D** Left, full section of IPF tissue (Fn, AF647). Middle panels, 20X detail of the Fn (AF647) and glutathionylation channels (AF555), scale bar 54 μ m. Right panel, resulting ratiometric image. Panels C and D show areas of higher GluFn/Fn ratio, indicating glutathionylation of Fn associated with these lung diseases. **E** Plots of median pixel-by-pixel GluFn:Ffn ratios from at least 20 random fields per condition, lung adenocarcinoma or patient matched normal lung. Glutathionylation of Fn is highly significantly increased ($p < 0.0001$). **F** Plots of median pixel-by-pixel GluFn:Ffn ratios from at least 20 random fields per condition, IPF or normal lung. Glutathionylation of Fn is significantly increased ($p = 0.0181$). Mann-Whitney two-tailed statistical tests were employed for statistical analysis.

CONCLUSION

Here, we provide the first evidence of fibronectin glutathionylation in the context of several lung pathologies and demonstrate the strain-dependency of glutathionylation, due to the cryptic location of reactive cysteines in the essential ECM protein, fibronectin. This modification was found to significantly reduce the force threshold required for cells to physically activate a conformational change in fibronectin's integrin-binding domain, leading to a cellular integrin switch in the engagement of fibronectin with clear consequences on downstream cytoskeletal signaling. The role of PTMs within the ECM has only recently gained attention in the field, but has the potential to expose new forms of information storage and transmission within the ECM. In particular, it is tempting to speculate that various PTMs mark the ECM and record events, like a contractile force or inflammation²⁰³. The accumulation of such marks could lead to a tipping point, whereby resident cells become more readily activated, potentially leading to disease initiation or more aggressive progression. In the case of Ox-PTMs and glutathionylation, this is particularly relevant considering the strong links between obesity and metabolic disorders and elevated systemic oxidative stress. The extent to which Ox-PTMs, and posttranslational modifications more generally, modulate the function of the ECM remains a significant gap in the field. Recording of stimulus history through such modifications adds to the substantial mosaic of factors driving complex diseases and will be an important consideration in the recent and increased use of decellularized tissues for regenerative medicine and stem cell delivery endeavors.

CHAPTER 4

IMPACT AND FUTURE DIRECTIONS

This thesis can be considered the culmination of 20 years of work in the field. The properties of 9III and 10III were first theorized via steered molecular dynamics¹⁸⁴, which unleashed efforts by mechanobiologists to understand the bidirectional signaling between ECM cell receptors (the integrins), and ECM proteins^{156,204}. Despite the engineering of a FRET sensor²⁰⁵, the Fn mimicking fragments themselves³¹, the relationship between Fn conformation and fibroblast behavior was never fully elucidated, to the best of our knowledge, until now. Our success was in part due to a unique experimental set up, as described earlier: Fn fragments regiospecifically conjugated to the substrate, physiologically soft gel substrates (5 kPa), and fibroblasts that were maintained phenotypically naïve despite being expanded to populate advanced assays²⁰⁶.

The findings highlighted in the previous chapters also suggest a “unifying” theory for the development of all diseases presenting as UIP. Activation of the IntSw likely takes place routinely during wound healing, given the prevalence of Fn in the clot and provisional matrix, and the temporally controlled activation of contractile fibroblasts in the wound bed. However, genetic factors, accumulated environmental damage, including redox-imbalance PTM (i.e. glutathionylation), lower the prerequisites for or indefinitely prolong this signal. I have successfully described the effects on cytoplasmic side signaling ensuing IntSw activation. Within 30 minutes, fibroblasts integrin adhesomes stray from baseline with the clustering of Vimentin and Collagen XII around the focal adhesion complexes. The Coll XIIa interaction in particular represents a novel development, as the protein

is canonically located in the extracellular space. The evidence presented here is not sufficient to add this fibrillar collagen to the set of proteins downstream of $\alpha\beta3$ signaling, but provides a lead worth pursuing. Furthermore, the heightened observed in phosphorylation levels (activity levels) of JNK, p38, Akt in cells seeded on the open IntSw indicate a more sustained activation of Rac over Ras pathways within 30 minutes. Ras-related signaling likely remains dominant for cells binding Fn IBD in a closed conformation.

Further investigation of the above phenomena, including later changes in the transcriptome (at 24 h), could include traditional reductionist biology studies relying on small molecule inhibition or Knock Out of the identified targets, looking at common downstream effectors. For example, the role of PI3K in IntSw signaling could be elucidated by using alpelisib, an inhibitor, or by measuring the activity and amount of PDK1 via Western Blot or mRNA transcript analysis, where qPCR might suffice.

Data Driven Modeling could be employed, starting with the data disclosed here, in order to find potentially novel nodes within these pathways, to then singularly target them in gain/loss of function type of experiments. A valid first approach at this stage could be represented by the technique involving paired signaling and phenotype data, championed by the Lazzara group here at UVA²⁰⁷.

The lack of success in inhibiting the IntSw in vitro does not necessarily invalidate the novel approach used to devise what was at first a mere research tool, H5. By not targeting cell-side receptors, I planned to reduce the unfortunately common whole cell-level side effects that have kept several promising compounds from reaching the clinic. On the contrary, targeting not merely the ECM, but a

pathologically associated modification thereof, suggesting a way for pre-clinical studies on a similar class of therapeutics, for applications well beyond organ fibrosis.

My work directly paves the way for better mechanotransduction studies involving integrins, having offset the impact of substrate stiffness on the expansion and growth of cell lines and on the experiments proper. Moreover, we now have the bases to expand the translatability of single chain fragment antibody H5 or an improved clone. While the occurrence of the epitope was described in mice under fibrotic lung conditions in an earlier publication⁵², it is necessary to detect the unfolded Fn IBD cryptic epitope in human lung fibrotic samples. Beyond the increased difficulty in acquiring human tissue, a negative IF or IHC staining result might not necessarily prove the absence of the Fn IntSw. Indeed, the epitope, far from being a covalent PTM, may be erased or damaged by the processing of the sample, including the fixation technique.

We also have the opportunity to improve H5, in particular its specificity for the open conformation of Fn IBD. A straightforward approach would entail reformatting H5 from a single chain antibody to a typical immunoglobulin gamma. However, this option offers tradeoffs. While affinity and specificity for the open conformation of the IntSw should improve due to the bivalence, access to the cryptic epitope might be compromised, since an IgG is 5 times as massive as a scFv. A more refined option relies on molecular evolution and screening (display) methods to discover better (as defined by affinity and specificity) clones of H5. A promising approach pioneered by the Reddy lab involves trained neural networks to screen a computational library of approximately 1×10^8 H5 variants and predict

the unfolded Fn-specific subset, which can then be filtered for viscosity, clearance, solubility and immunogenicity to generate thousands of highly optimized lead candidates^{208,209}.

In order to improve upon these in vitro results and embrace more physiologically relevant conditions, I should adopt human tissue as fibroblasts substrate. In the context of lung fibrosis, Precision Cut Lung Slices (PCLS) with thickness around 100 μm represent a first step in that direction. After crosslinking a PCLS to a soft substrate, such as a PDMS gel, H5 or its improved clone would be added in molar excess in order to block the $\alpha\text{v}\beta\text{3}$ binding site. Naïve fibroblasts could be seeded on PCLS blocked with or without H5 and their transcriptional activity compared. I expect H5 or its better clone should prevent activation of naïve fibroblasts seeded on IPF PCLS. Lastly, the above assay would be even more relevant if human fibroblasts were used, instead of murine cells we used in the vast majority of this work. Given the issues due to tissue thickness, analysis of bulk mRNA across the conditions (with or without H5 blocking) would represent an adequate metric.

Closing the loop between the lower threshold needed to activate the IntSw (due to glutathionylation) and fibroblast signaling is another aim worth pursuing. While we have identified an increase in MRTF nuclear translocation, there are several other pathways that contribute to myofibroblastic differentiation, not to mention actual myofibroblastic markers. Comparing mRNA transcripts between naïve MLFs seeded on unmodified dECM or glutathionylated dECM should reveal trends similar to the ones that emerged when comparing MLFs on 4G vs 9*10.

Furthermore, it would be beneficial to confirm glutathionylation of Fn in human diseases not merely by colocalization, but by screening for and designing an antibody preferentially binding GluFn. Knowing the errors committed in designing the screening strategy in the previous unsuccessful attempt, the phage (or less rudimentary) screens should be based on glutathionylated Fn 7-8III and its unmodified version.

Further in the future, before pursuing H5 (or improved clone) efficacy studies on animal models or exploring other murine models of organ fibrosis, we ought to settle on a delivery method. While direct protein administration, whether via intraperitoneal, subcutaneous, or tail vein injection is convenient for preliminary studies, these methods not necessarily clinically relevant and might promote an immune reaction against the antibody H5 with repeated doses. Drug delivery optimization might be considered a PhD project on its own, but here are two promising approaches to investigate. The first is AAV mediated delivery of the H5 DNA sequence, the second is naked mRNA delivery of the H5 sequence, potentially via nebulization into the airways. We could use a delivery technique pioneered by the Santangelo lab²¹⁰ that enables aerosolized delivery of naked messenger resuspended in PBS into the lung airspace. This approach will bypass systemic exposure side effects including inflammation.

mRNA has been successfully employed for therapeutic delivery of proteins or as therapy in and of itself in a variety of in vivo application to the lung and beyond²¹¹⁻²¹⁴. Furthermore, mRNA does not present the same issues related to delivery of DNA or proteins such as permanent genome incorporation or immunogenicity, respectively. Surprisingly, mRNA is cost effective compared to

the other two payloads. Moreover, replacement of certain bases with chemically modified ones in synthetic mRNAs has been shown to decrease their recognition by the innate immune system.

As mentioned above, animal studies involving different lung fibrosis models will remove doubts about the efficacy of H5 (or clone) being tied to the artifacts and peculiarities of one particular lung injury model. For example, this argument would be strengthened if H5 showed similar protective effects in Wild Type (BL6C57) receiving multiple intratracheal doses of bleomycin²¹⁵. On the other hand, we could leverage mice with different genotypes enabling non-resolving lung fibrosis. In addition to a model defined by aberrant $\alpha v \beta 3$ activation (Thy-1 / CD90 KO), the lab has access to the conditional integrin $\alpha 5$ KO model driven by a PDGFR α promoter, which is expressed by fibroblasts partaking in fibrotic remodeling according to the Sun group⁷⁰. Even without administration of a candidate therapeutic, this model should be used in studies aimed at elucidating the impact of integrin $\alpha 5$ removal in lung fibrosis. In particular, I would expect the highest degree of fibrosis in mice homozygous for the floxed integrin (as long as the two other promoter genes are present), while mice with the identical genotype that have not been induced with doxycycline would present the well-described resolving progression of the disease after single bleomycin insult. Induced, but heterozygous mice would present a fibrotic stage intermediate between the two groups above.

In conclusion, this thesis elucidates the effects of conformational changes in Fn IBD and lays the groundwork for a family of H5-derived antibodies to complete pre-clinical studies. Even past that stage, it is plausible that H5 or related

clone might become part of a successful treatment in combination with other independent APIs, given the complexity of lung fibrosis.

APPENDIX A: SUPPLEMENTAL DATA

Adhesome Data

Enriched Proteins on 9-4G-10III	Accession	Alternate	Mean 4G	Mean 9*10	4G/9*10
Tubulin beta-3 chain OS=Homo sapiens GN=TUBB3 PE=1 SV=2	Q13309	TUBB3	15.70015	0.1	157.0015
Keratin, type I cytoskeletal 13 OS=Homo sapiens GN=KRT13 PE=1 SV=	K7ERE3 (+)	KRT13	3.292425	0.1	32.92425
Keratin 77 OS=Homo sapiens GN=KRT77 PE=1 SV=1	Q0IIN1 (+)	KRT77	3.507165	0.1	35.07165
cDNA FLJ58539, highly similar to Keratin, type II cytoskeletal 4 OS=Ho	B4DKJ0 (+)		3.292425	0.1	32.92425
Keratin, type II cytoskeletal 78 OS=Homo sapiens GN=KRT78 PE=1 SV=	Q8N1N4	KRT78	3.423291	0.1	34.23291
60S ribosomal protein L6 OS=Homo sapiens GN=RPL6 PE=3 SV=1	A0A024RB	RPL6	4.060957	0.1	40.60957
Collagen alpha-1(XII) chain OS=Homo sapiens GN=COL12A1 PE=1 SV=	D6RGG3 (+)	COL12A1	3.329307	0.1	33.29307
Ribosomal protein L34, isoform CRA_a OS=Homo sapiens GN=RPL34 P	A0A024RD	RPL34	2.006983	0.1	20.06983
Septin-11 OS=Homo sapiens GN=SEPT11 PE=1 SV=1	D6RERS (+)	SEPT11	2.053975	0.1	20.53975
Interferon-induced protein with tetratricopeptide repeats 1 OS=Homo	P09914	IFIT1	0.637666	0.1	6.376663
Eukaryotic translation initiation factor 3 subunit I OS=Homo sapiens C	Q13347 (+)	EIF3I	1.68815	0.1	16.8815
RNA binding motif protein 14 isoform 1 (Fragment) OS=Homo sapien	A0A052Z4	RBM14	1.735141	0.1	17.35141
cDNA FLJ75556, highly similar to Homo sapiens ribosomal protein L14	A8K7N0		2.691641	0.1	26.91641
Tight junction protein ZO-1 OS=Homo sapiens GN=TJP1 PE=1 SV=1	A0A087X0	TJP1	2.738633	0.1	27.38633
Ras-related protein Ral-A OS=Homo sapiens GN=RALA PE=1 SV=1	P11233	RALA	0.956499	0.1	9.564995
Testicular tissue protein Li 149 OS=Homo sapiens PE=2 SV=1	A0A140VJ3	(+)	1.369316	0.1	13.69316
Coatamer subunit beta' OS=Homo sapiens GN=COPB2 PE=1 SV=2	P35606	COPB2	2.372808	0.1	23.72808
Band 4.1-like protein 3 OS=Homo sapiens GN=EPB41L3 PE=1 SV=1	A0A0A0M	EPB41L3	1.369316	0.1	13.69316
Dynamin-2 OS=Homo sapiens GN=DNM2 PE=1 SV=2	P50570	DNM2	1.735141	0.1	17.35141
HCG1994130, isoform CRA_a OS=Homo sapiens GN=hCG_1994130 PE=	B2R4W8 (-)	hCG_1994	1.097475	0.1	10.97475
2'-5'-oligoadenylate synthetase 3, 100kDa, isoform CRA_a OS=Homo s	A0A024RB	OAS3	1.097475	0.1	10.97475
Interferon-induced GTP-binding protein Mx1 OS=Homo sapiens GN=I	P20591	MX1	0.637666	0.1	6.376663
Eukaryotic translation initiation factor 3 subunit C OS=Homo sapiens	A0A024QY	EIF3S8	2.053975	0.1	20.53975
60S ribosomal protein L7a OS=Homo sapiens GN=RPL7A PE=1 SV=2	P62424 (+)	RPL7A	0.956499	0.1	9.564995
Testicular tissue protein Li 27 OS=Homo sapiens PE=2 SV=1	A0A140VJ3	(+)	0.637666	0.1	6.376663
26S proteasome non-ATPase regulatory subunit 11 OS=Homo sapiens	O00231	PSMD11	0.73165	0.1	7.3165
cDNA FLJ55002, highly similar to Alpha-centractin OS=Homo sapiens I	B4DM97 (+)		0.637666	0.1	6.376663
Apoptosis-inducing factor 2 OS=Homo sapiens GN=AIFM2 PE=1 SV=1	Q9BRQ8	AIFM2	0.73165	0.1	7.3165
40S ribosomal protein S9 OS=Homo sapiens GN=RPS9 PE=1 SV=1	A0A024R4	RPS9	0.637666	0.1	6.376663
EH-domain containing 4, isoform CRA_a OS=Homo sapiens GN=EHD4	A0A024R9	EHD4	1.369316	0.1	13.69316
RuvB-like helicase (Fragment) OS=Homo sapiens GN=RUVBL1 PE=2 SV	B5BUB1 (+)	RUVBL1	0.637666	0.1	6.376663
Filaggrin-2 OS=Homo sapiens GN=FLG2 PE=1 SV=1	Q5D862	FLG2	1.735141	0.1	17.35141
Zyxin (Fragment) OS=Homo sapiens GN=ZYX PE=1 SV=1	HOY2Y8 (+)	ZYX	0.956499	0.1	9.564995
Heterogeneous nuclear ribonucleoprotein L (Fragment) OS=Homo sa	M0QX55 (-)	HNRNPL	0.637666	0.1	6.376663
Microtubule-associated protein 1B, isoform CRA_b OS=Homo sapiens	A0A024RA	MAP1B	0.956499	0.1	9.564995
RNA-binding motif protein, X chromosome OS=Homo sapiens GN=RB	P38159	RBMX	0.73165	0.1	7.3165
Integrin-linked protein kinase OS=Homo sapiens GN=ILK PE=1 SV=1	A0A0A0M	ILK	0.73165	0.1	7.3165
VARS OS=Homo sapiens GN=VARS PE=1 SV=1	A0A024RC	VARS	0.956499	0.1	9.564995
Dynactin subunit 1 OS=Homo sapiens GN=DCTN1 PE=1 SV=1	E7EX90 (+)	DCTN1	1.369316	0.1	13.69316
cDNA FLJ55606, highly similar to Alpha-2-HS-glycoprotein OS=Homo s	B7Z8Q2 (+)		0.73165	0.1	7.3165
COP9 constitutive photomorphogenic-like protein subunit 4 isoform	A0A052Z5	COPS4	1.369316	0.1	13.69316
Sorting nexin OS=Homo sapiens PE=2 SV=1	B2RAU5 (+)		1.369316	0.1	13.69316
Ribosomal protein L23, isoform CRA_b OS=Homo sapiens GN=RPL23 P	A0A024R1	RPL23	0.73165	0.1	7.3165
Kinesin light chain 1J OS=Homo sapiens GN=KNS2 PE=2 SV=1	Q7RTP8 (+)	KNS2	0.637666	0.1	6.376663
Dihydropyrimidinase-related protein 2 OS=Homo sapiens GN=DPYSL	A0A1C7CY	DPYSL2	0.73165	0.1	7.3165
Annexin OS=Homo sapiens GN=ANXA5 PE=1 SV=1	D6RBL5 (+)	ANXA5	0.637666	0.1	6.376663
Ribonuclease/angiogenin inhibitor 1, isoform CRA_a OS=Homo sapie	A0A024RC	RNH1	1.097475	0.1	10.97475
2',3'-cyclic-nucleotide 3'-phosphodiesterase OS=Homo sapiens GN=C	A0A024R1	CNP	0.73165	0.1	7.3165
Angiopoietin-like 2, isoform CRA_a OS=Homo sapiens GN=ANGPTL2 F	A0A024R8	ANGPTL2	0.956499	0.1	9.564995
Myoferlin OS=Homo sapiens GN=MYOF PE=1 SV=1	Q9NZM1	MYOF	1.68815	0.1	16.8815
Developmentally-regulated GTP-binding protein 1 OS=Homo sapiens	Q9Y295	DRG1	1.369316	0.1	13.69316

Enriched Proteins on 9*10III	Accession	Alternate	Mean 4G	Mean 9*10	4G/9*10
NAD(P)H dehydrogenase [quinone] 1 OS=Homo sapiens GN=NQO1 P	B4DLR8 (+)	NQO1	1.735141	4.140553	0.41906
MHC class I antigen OS=Homo sapiens GN=HLA-C PE=3 SV=2	K7DWB0	HLA-C	0.73165	1.820276	0.401944
Protein FAM98A OS=Homo sapiens GN=FAM98A PE=1 SV=1	E9PH82 (+)	FAM98A	0.73165	1.820276	0.401944
COP9 constitutive photomorphogenic homolog subunit 8 (Arabidops	A0A024R4	COPS8	0.73165	1.820276	0.401944
40S ribosomal protein S2 OS=Homo sapiens GN=RPS2 PE=1 SV=2	P15880 (+)	RPS2	0.73165	1.820276	0.401944
Methylenetetrahydrofolate dehydrogenase (NADP+ dependent) 1, n	A0A024R6	MTHFD1	1.097475	2.730415	0.401944
Microtubule-actin cross-linking factor 1, isoforms 1/2/3/5 OS=Homo s	H3BQK9	MACF1	2.006983	5.281106	0.380031
60S ribosomal protein L24 OS=Homo sapiens GN=RPL24 PE=1 SV=1	C9JNW5 (-)	RPL24	0.637666	1.820276	0.350313
40S ribosomal protein S18 OS=Homo sapiens GN=RPS18 PE=1 SV=3	P62269	RPS18	0.637666	1.820276	0.350313
cDNA, FLJ94919, highly similar to Homo sapiens protein phosphatase	B2RAH5 (+1)		0.73165	2.320276	0.315329
Insulin-like growth factor 2 mRNA-binding protein 2 OS=Homo sapien	F8W930 (+)	IGF2BP2	0.637666	2.230415	0.285896
cDNA, FLJ95508, highly similar to Homo sapiens 5'-nucleotidase, ecto	B2RBH2 (+4)		0.637666	2.230415	0.285896
Rho/rac guanine nucleotide exchange factor (GEF) 2, isoform CRA_a	D3DVA5 (-)	ARHGEF2	0.73165	2.640553	0.277082
Apolipoprotein L, 2, isoform CRA_a OS=Homo sapiens GN=APOL2 PE=	A0A024R1	APOL2	0.637666	2.730415	0.233542
Inosine-5'-monophosphate dehydrogenase 2 (Fragment) OS=Homo s	H0Y4R1	IMPDH2	0.1	3.230415	0.030956
Uncharacterized protein DKFZp686F17268 (Fragment) OS=Homo sapien	A4GY8 (+)	DKFZp686	0.1	1.5	0.066667
Filamin B, beta (Actin binding protein 278), isoform CRA_a OS=Homo	A0A024R3	FLNB	0.1	1.640553	0.060955
Ras GTPase-activating protein-binding protein 1 OS=Homo sapiens G	Q13283 (+)	G3BP1	0.1	1.820276	0.054937
TAR DNA binding protein, isoform CRA_b OS=Homo sapiens GN=TARI	A0A024R4	TARDBP	0.1	1.230415	0.081273
Epididymis luminal protein 4 OS=Homo sapiens GN=YWHAZ PE=2 SV=	D0PN11 (+)	YWHAZ	0.1	0.820276	0.12191
Signal recognition particle subunit SRP68 OS=Homo sapiens GN=SRP6	Q9UHB9	SRP68	0.1	1.820276	0.054937
Ubiquitin-like protein ISG15 (Fragment) OS=Homo sapiens GN=ISG15	A0A096LN	ISG15	0.1	1.820276	0.054937
KN motif and ankyrin repeat domain-containing protein 2 OS=Homo	Q63ZY3	KANK2	0.1	0.820276	0.12191
cDNA FLJ43948 fis, clone TESTI4014924, highly similar to Homo sapien	B3KVV6 (+2)		0.1	0.820276	0.12191
cDNA FLJ78244, highly similar to Homo sapiens eukaryotic translation	A8K7F6 (+1)		0.1	0.820276	0.12191
Chloride intracellular channel protein OS=Homo sapiens PE=3 SV=1	A0A1U9X8Y4 (+3)		0.1	1.230415	0.081273
Plasminogen activator, urokinase, isoform CRA_a OS=Homo sapiens	A0A024QZ	PLAU	0.1	0.820276	0.12191
Tropomyosin alpha-1 chain (Fragment) OS=Homo sapiens GN=TPM1 F	H0YL52	TPM1	0.1	1.230415	0.081273
ADP-ribosylation factor 4 OS=Homo sapiens GN=ARF4 PE=1 SV=3	P18085	ARF4	0.1	0.820276	0.12191
HCG31253, isoform CRA_a OS=Homo sapiens GN=hCG_31253 PE=4 SV=	A0A024R8	hCG_3125	0.1	1.820276	0.054937
Cold shock domain containing E1, RNA-binding, isoform CRA_a OS=H	A0A024R0	CSDE1	0.1	1.230415	0.081273
60S ribosomal protein L23a OS=Homo sapiens GN=RPL23A PE=1 SV=1	A8MUS3 (-)	RPL23A	0.1	1.820276	0.054937
Pre-mRNA-processing factor 19 OS=Homo sapiens GN=PRPF19 PE=1 S	Q9UUM54	PRPF19	0.1	0.820276	0.12191
Actinin, alpha 1, isoform CRA_a OS=Homo sapiens GN=ACTN1 PE=4 S	A0A024R6	ACTN1	0.1	0.820276	0.12191
Serpin B3 OS=Homo sapiens GN=SERPINB3 PE=1 SV=2	P29508	SERPINB3	0.1	0.820276	0.12191
Nucleosome assembly protein 1-like 1, isoform CRA_a OS=Homo sap	A0A024RB	NAP1L1	0.1	0.820276	0.12191
Centrosomal protein 170kDa OS=Homo sapiens GN=CEP170 PE=2 SV=	A6H8X9 (+)	CEP170	0.1	0.820276	0.12191
40S ribosomal protein S13 OS=Homo sapiens GN=RPS13 PE=1 SV=1	J3KMX5 (+)	RPS13	0.1	1	0.1
Fibroblast growth factor receptor OS=Homo sapiens GN=FGFR4 PE=3	A0A024R7	FGFR4	0.1	1	0.1
Uncharacterized protein (Fragment) OS=Homo sapiens PE=4 SV=1	H0YHGO		0.1	0.820276	0.12191
60S ribosomal protein L9 (Fragment) OS=Homo sapiens GN=RPL9 PE=	H0Y9V9	RPL9	0.1	0.820276	0.12191
Caveolae-associated protein 3 OS=Homo sapiens GN=CAVIN3 PE=1 S	E9PIE3 (+1)	CAVIN3	0.1	0.820276	0.12191
Src substrate cortactin OS=Homo sapiens GN=CTTN PE=1 SV=2	Q14247 (+)	CTTN	0.1	1	0.1
Vinculin, isoform CRA_c OS=Homo sapiens GN=VCL PE=4 SV=1	A0A024QZ	VCL	0.1	1	0.1
SH3-domain GRB2-like 1 OS=Homo sapiens GN=SH3GL1 PE=1 SV=1	Q6FGM0 (-)	SH3GL1	0.1	0.820276	0.12191
GDP-mannose pyrophosphorylase A, isoform CRA_a OS=Homo sapien	A0A024R4	GMPPA	0.1	0.820276	0.12191
Cytoplasmic linker 2, isoform CRA_b OS=Homo sapiens GN=CYLN2 PE	A0A140VJ	CYLN2	0.1	1	0.1
Sorting nexin OS=Homo sapiens GN=SNX6 PE=1 SV=1	A0A0A0M	SNX6	0.1	1	0.1
Fructose-bisphosphate aldolase A (Fragment) OS=Homo sapiens GN=	H3BPS8 (+)	ALDOA	0.1	0.820276	0.12191
cDNA FLJ59571, highly similar to Eukaryotic translation initiation fact	B4DZF2 (+4)		0.1	0.820276	0.12191
Ribosomal protein L18, isoform CRA_c OS=Homo sapiens GN=RPL18 P	A0A024QZ	RPL18	0.1	1	0.1
Dermcidin OS=Homo sapiens GN=DCD PE=1 SV=2	P81605	DCD	0.1	0.820276	0.12191
Protein transport protein sec16 (Fragment) OS=Homo sapiens GN=SE	A4QN18 (-)	SEC16A	0.1	0.820276	0.12191

RNAseq Data

Upregulated in 4G/9*10			
pvalue	padj	mgi_symb	entrezgen description
0	0	llysyna1	71780 myo-inositol 1-phosphate synthase A1 [Source:MGI Symbol;Acc:MG
4.78E-200	2.34E-196	C4b	12268 complement component 4B (Chido blood group) [Source:MGI Symb
3.85E-170	1.35E-166	Mctp2	244049 multiple C2 domains, transmembrane 2 [Source:MGI Symbol;Acc:M
3.67E-168	1.12E-164	Olfml3	99543 olfactomedin-like 3 [Source:MGI Symbol;Acc:MGI:1914877]
8.61E-146	2.34E-142	Scp2	20280 sterol carrier protein 2, liver [Source:MGI Symbol;Acc:MGI:98254]
5.35E-128	1.09E-124	ApoE	11816 apolipoprotein E [Source:MGI Symbol;Acc:MGI:88057]
2.38E-127	4.11E-124	Hal	15109 histidine ammonia lyase [Source:MGI Symbol;Acc:MGI:96010]
7.24E-120	1.04E-116	Bicc1	83675 Bicc family RNA binding protein 1 [Source:MGI Symbol;Acc:MGI:193
1.27E-112	1.41E-109	Cxadr	13052 coxsackie virus and adenovirus receptor [Source:MGI Symbol;Acc:V
1.32E-111	1.41E-108	Ifi272a	76933 interferon, alpha-inducible protein 27 like 2A [Source:MGI Symbol;
1.17E-109	1.19E-106	Plat	18791 plasminogen activator, tissue [Source:MGI Symbol;Acc:MGI:97610]
1.71E-107	1.66E-104	Ednra	13617 endothelin receptor type A [Source:MGI Symbol;Acc:MGI:105923]
1.39E-104	1.18E-101	Cpt2	12896 carnitine palmitoyltransferase 2 [Source:MGI Symbol;Acc:MGI:1091
7.09E-103	5.79E-100	Gdpd2	71584 glycerophosphodiester phosphodiesterase domain containing 2 [Sc
2.43E-102	1.92E-99	G0s2	14373 G0/G1 switch gene 2 [Source:MGI Symbol;Acc:MGI:1316737]
2.54E-101	1.89E-98	Ism1	319909 isthmin 1, angiogenesis inhibitor [Source:MGI Symbol;Acc:MGI:244;
9.69E-101	6.79E-98	Ada	11486 adenosine deaminase [Source:MGI Symbol;Acc:MGI:87916]
2.07E-100	1.41E-97	Kcnj8	16523 potassium inwardly-rectifying channel, subfamily J, member 8 [Sou
4.75E-99	3.07E-96	Nt5dc2	70021 5'-nucleotidase domain containing 2 [Source:MGI Symbol;Acc:MGI:1
8.36E-99	5.12E-96	Il1r1	16177 interleukin 1 receptor, type I [Source:MGI Symbol;Acc:MGI:96545]
1.00E-98	5.98E-96	Il6st	16195 interleukin 6 signal transducer [Source:MGI Symbol;Acc:MGI:96560]
1.20E-98	7.03E-96	Tnxb	81877 tenascin XB [Source:MGI Symbol;Acc:MGI:1932137]
4.59E-97	2.55E-94	Il1r12	107527 interleukin 1 receptor-like 2 [Source:MGI Symbol;Acc:MGI:1913107]
1.95E-96	1.06E-93	Ptger3	19218 prostaglandin E receptor 3 (subtype EP3) [Source:MGI Symbol;Acc:G
2.61E-96	1.39E-93	Gyg	27357 glycogenin [Source:MGI Symbol;Acc:MGI:1351614]
2.23E-95	1.16E-92	Frm5	228564 FERM domain containing 5 [Source:MGI Symbol;Acc:MGI:2442557]
2.71E-92	1.35E-89	Ptger2	19217 prostaglandin E receptor 2 (subtype EP2) [Source:MGI Symbol;Acc:G
8.94E-92	4.21E-89	D430019H	268595 RIKEN cDNA D430019H16 gene [Source:MGI Symbol;Acc:MGI:244312
1.44E-91	6.55E-89	Sfrp1	20377 secreted frizzled-related protein 1 [Source:MGI Symbol;Acc:MGI:89
1.44E-91	6.55E-89	Arhgap20	244867 Rho GTPase activating protein 20 [Source:MGI Symbol;Acc:MGI:244;
3.30E-91	1.47E-88	Mfap4	76293 microfilament-associated protein 4 [Source:MGI Symbol;Acc:MGI:13
5.80E-91	2.54E-88	Olfml1	244198 olfactomedin-like 1 [Source:MGI Symbol;Acc:MGI:2679264]
1.16E-88	4.99E-86	Echdc2	52430 enoyl Coenzyme A hydratase domain containing 2 [Source:MGI Synt
2.02E-87	8.24E-85	Igf1bp3	16009 insulin-like growth factor binding protein 3 [Source:MGI Symbol;Ac
1.86E-86	7.25E-84	Rnf122	68867 ring finger protein 122 [Source:MGI Symbol;Acc:MGI:1916117]
1.35E-83	5.01E-81	Rab3d	19340 RAB3D, member RAS oncogene family [Source:MGI Symbol;Acc:MG
5.11E-82	1.84E-79	Myo5b	17919 myosin VB [Source:MGI Symbol;Acc:MGI:106598]
1.82E-80	6.36E-78	Gdf10	14560 growth differentiation factor 10 [Source:MGI Symbol;Acc:MGI:9568
1.37E-79	4.72E-77	Mdfi	17240 MyoD family inhibitor [Source:MGI Symbol;Acc:MGI:107687]
6.61E-79	2.19E-76	Il33	77125 interleukin 33 [Source:MGI Symbol;Acc:MGI:1924375]
6.80E-79	2.22E-76	Kdr	16542 kinase insert domain protein receptor [Source:MGI Symbol;Acc:MG
1.40E-78	4.53E-76	G5300110	654820 RIKEN cDNA G530011006 gene [Source:MGI Symbol;Acc:MGI:360351
2.89E-78	9.21E-76	Shisa6	380702 shisa family member 6 [Source:MGI Symbol;Acc:MGI:2685725]
1.09E-75	3.24E-73	Vstm4	320736 V-set and transmembrane domain containing 4 [Source:MGI Symbo
8.68E-73	2.47E-70	Acat1	110446 acetyl-Coenzyme A acetyltransferase 1 [Source:MGI Symbol;Acc:MK
1.24E-72	3.50E-70	Cdon	57810 cell adhesion molecule-related/down-regulated by oncogenes [So
1.38E-72	3.85E-70	Arsi	545260 arylsulfatase i [Source:MGI Symbol;Acc:MGI:2670959]
2.05E-72	5.64E-70	Fads6	328035 fatty acid desaturase domain family, member 6 [Source:MGI Symbo
2.10E-72	5.71E-70	Stab1	192187 stabilin 1 [Source:MGI Symbol;Acc:MGI:2178742]
5.47E-72	1.44E-69	Gm14226	50518 predicted gene 14226 [Source:MGI Symbol;Acc:MGI:3649244]
5.10E-70	1.29E-67	Mmp23	26561 matrix metalloproteinase 23 [Source:MGI Symbol;Acc:MGI:1347361]
6.67E-70	1.67E-67	Hdc	15186 histidine decarboxylase [Source:MGI Symbol;Acc:MGI:96062]
2.13E-69	5.26E-67	Cyp2d22	56448 cytochrome P450, family 2, subfamily d, polypeptide 22 [Source:MG
1.45E-67	3.48E-65	A2m	232345 alpha-2-macroglobulin [Source:MGI Symbol;Acc:MGI:2449119]
6.14E-67	1.42E-64	Z310043P	NA RIKEN cDNA Z310043P16 gene [Source:MGI Symbol;Acc:MGI:191738
6.41E-67	1.47E-64	Tspan5	56224 tetraspanin 5 [Source:MGI Symbol;Acc:MGI:1928096]
1.55E-66	3.52E-64	Rcn3	52377 reticulocalbin 3, EF-hand calcium binding domain [Source:MGI Syml
2.28E-66	5.14E-64	Gpx3	14778 glutathione peroxidase 3 [Source:MGI Symbol;Acc:MGI:105102]
3.87E-66	8.63E-64	Fgd5	232237 FYVE, RhoGEF and PH domain containing 5 [Source:MGI Symbol;Acc
8.47E-66	1.85E-63	Spsb1	74646 splan/ryanodine receptor domain and SOCS box containing 1 [Source
2.01E-65	4.37E-63	Il2zra1	230828 interleukin 22 receptor, alpha 1 [Source:MGI Symbol;Acc:MGI:26635
2.16E-65	4.63E-63	Pccb	66904 propionyl Coenzyme A carboxylase, beta polypeptide [Source:MGI
5.27E-65	1.12E-62	Scara5	71145 scavenger receptor class A, member 5 [Source:MGI Symbol;Acc:MGI
6.98E-65	1.46E-62	Kif26b	269152 kinesin family member 26B [Source:MGI Symbol;Acc:MGI:2447076]
3.89E-63	7.76E-61	C2	12263 complement component 2 (within H-2S) [Source:MGI Symbol;Acc:V
3.04E-62	6.01E-60	Chrdl2	69121 chordin-like 2 [Source:MGI Symbol;Acc:MGI:1916371]
1.19E-61	2.29E-59	Cldn10	58187 claudin 10 [Source:MGI Symbol;Acc:MGI:1913101]
1.39E-61	2.66E-59	Pde1a	18573 phosphodiesterase 1A, calmodulin-dependent [Source:MGI Symbo
4.29E-61	8.08E-59	Fkbp7	14231 FK506 binding protein 7 [Source:MGI Symbol;Acc:MGI:1336879]
5.19E-61	9.71E-59	Fbln1	14114 fibulin 1 [Source:MGI Symbol;Acc:MGI:95487]
7.24E-61	1.34E-58	RbmX	19655 RNA binding motif protein, X chromosome [Source:MGI Symbol;Acc
1.75E-60	3.21E-58	Vegfd	14205 vascular endothelial growth factor D [Source:MGI Symbol;Acc:MGI:1
5.53E-60	9.97E-58	Vkorc1	27973 vitamin K epoxide reductase complex, subunit 1 [Source:MGI Symb
1.12E-59	2.00E-57	Tnfrsf13b	24099 tumor necrosis factor (ligand) superfamily, member 13b [Source:MG
1.27E-59	2.25E-57	Gm14066	NA predicted gene 14066 [Source:MGI Symbol;Acc:MGI:3649728]
2.50E-58	4.32E-56	Cldn5	12741 claudin 5 [Source:MGI Symbol;Acc:MGI:1276112]
2.64E-58	4.53E-56	Gfpt2	14584 glutamine fructose-6-phosphate transaminase 2 [Source:MGI Symb
1.29E-56	2.12E-54	Kit	16590 KIT proto-oncogene receptor tyrosine kinase [Source:MGI Symbol;#
2.59E-56	4.18E-54	Rapgef5	217944 Rap guanine nucleotide exchange factor (GEF) 5 [Source:MGI Symb
4.62E-56	7.36E-54	Amigo2	105827 adhesion molecule with Ig like domain 2 [Source:MGI Symbol;Acc:G
8.58E-56	1.36E-53	Azin2	242669 antizyme inhibitor 2 [Source:MGI Symbol;Acc:MGI:2442093]
1.91E-55	3.00E-53	Lgr5	14160 leucine rich repeat containing G protein coupled receptor 5 [Source
5.47E-55	8.54E-53	Reps2	194590 RALBP1 associated Eps domain containing protein 2 [Source:MGI Sy
6.04E-55	9.36E-53	Cfi	12630 complement component factor i [Source:MGI Symbol;Acc:MGI:1059
1.03E-54	1.59E-52	Cables1	63955 CDKS and Abl enzyme substrate 1 [Source:MGI Symbol;Acc:MGI:192
1.32E-54	2.02E-52	Camk2a	12322 calcium/calmodulin-dependent protein kinase II alpha [Source:MG
1.52E-54	2.32E-52	Itga2	16398 integrin alpha 2 [Source:MGI Symbol;Acc:MGI:96600]
1.63E-53	2.41E-51	Wasf3	245880 WASP family, member 3 [Source:MGI Symbol;Acc:MGI:2658986]
6.88E-53	1.00E-50	Cxcl12	20315 chemokine (C-X-C motif) ligand 12 [Source:MGI Symbol;Acc:MGI:10
1.17E-51	1.69E-49	A530020G	NA RIKEN cDNA A530020G20 gene [Source:MGI Symbol;Acc:MGI:244282
1.54E-51	2.20E-49	Slc44a2	68682 solute carrier family 44, member 2 [Source:MGI Symbol;Acc:MGI:19
3.69E-51	5.14E-49	Igf1bp4	16010 insulin-like growth factor binding protein 4 [Source:MGI Symbol;Ac
3.98E-51	5.51E-49	Gpsm2	76123 G-protein signalling modulator 2 (AGS3-like, C. elegans) [Source:MK
4.22E-51	5.80E-49	Fam180a	208164 family with sequence similarity 180, member A [Source:MGI Symbo
1.30E-50	1.76E-48	Slc43a3	58207 solute carrier family 43, member 3 [Source:MGI Symbol;Acc:MGI:19
1.94E-50	2.62E-48	Adgrf5	224792 adhesion G protein-coupled receptor F5 [Source:MGI Symbol;Acc:V
2.69E-50	3.60E-48	Lgi3	213469 leucine-rich repeat LGI family, member 3 [Source:MGI Symbol;Acc:G
4.64E-50	6.18E-48	Fah	14085 fumarylacetoacetate hydrolase [Source:MGI Symbol;Acc:MGI:95482
9.53E-50	1.26E-47	Palmd	114301 palmdelphin [Source:MGI Symbol;Acc:MGI:2148896]
1.15E-49	1.52E-47	Tbx4	21387 T-box 4 [Source:MGI Symbol;Acc:MGI:102556]

Downregulated in 4G/9*10			
pvalue	padj	mgi_symb	entrezgen description
	0	0	Ptgs2 19225 prostaglandin-endoperoxide synthase 2 [Source:MGI Symbol;Acc:MG
5.13E-267	4.19E-263	Htr1b	15551 5-hydroxytryptamine (serotonin) receptor 1B [Source:MGI Symbol;Acc:MG
2.26E-201	1.38E-197	Sox11	20666 SRY (sex determining region Y)-box 11 [Source:MGI Symbol;Acc:MG
1.10E-183	4.48E-180	Hbegf	15200 heparin-binding EGF-like growth factor [Source:MGI Symbol;Acc:MG
3.60E-140	8.82E-137	Cited2	17684 Cbp/p300-interacting transactivator, with Glu/Asp-rich carboxy-ter
8.32E-134	1.85E-130	Nt5dc3	103466 5'-nucleotidase domain containing 3 [Source:MGI Symbol;Acc:MG:1
5.17E-122	9.05E-119	Lif	16878 leukemia inhibitory factor [Source:MGI Symbol;Acc:MG:96787]
3.47E-121	5.66E-118	Itpril2	319622 inositol 1,4,5-triphosphate receptor interacting protein-like 2 [Sou
5.21E-120	7.98E-117	Anxa1	16952 annexin A1 [Source:MGI Symbol;Acc:MG:96819]
5.92E-119	8.06E-116	Pgrmc1	53328 progesterone receptor membrane component 1 [Source:MGI Symb
7.28E-114	9.39E-111	Fosl1	14283 fos-like antigen 1 [Source:MGI Symbol;Acc:MG:107179]
2.17E-113	2.66E-110	Btc	12223 betacellulin, epidermal growth factor family member [Source:MGI:
6.21E-113	7.25E-110	Apbb2	11787 amyloid beta (A4) precursor protein-binding, family B, member 2 [S
1.76E-107	1.66E-104	Flnb	286940 filamin, beta [Source:MGI Symbol;Acc:MG:2446089]
4.81E-107	4.37E-104	Ankrd1	107765 ankyrin repeat domain 1 (cardiac muscle) [Source:MGI Symbol;Acc:
2.50E-106	2.19E-103	Rassf6	73246 Ras association (RalGDS/AF-6) domain family member 6 [Source:MK
1.71E-101	1.31E-98	Sh3kbp1	58194 SH3-domain kinase binding protein 1 [Source:MGI Symbol;Acc:MG:
9.32E-101	6.71E-98	Dusp4	319520 dual specificity phosphatase 4 [Source:MGI Symbol;Acc:MG:244219
4.57E-100	3.03E-97	Ccdc85a	216613 coiled-coil domain containing 85A [Source:MGI Symbol;Acc:MG:204
5.62E-99	3.53E-96	Srgap3	259302 SLIT-RHO GTPase activating protein 3 [Source:MGI Symbol;Acc
3.62E-98	2.06E-95	Cd44	12505 CD44 antigen [Source:MGI Symbol;Acc:MG:88338]
2.08E-94	1.06E-91	Noct	12457 nocturnin [Source:MGI Symbol;Acc:MG:109382]
3.30E-92	1.62E-89	Tmem200	77220 transmembrane protein 200A [Source:MGI Symbol;Acc:MG:192447
8.66E-92	4.16E-89	Sgms2	74442 sphingomyelin synthase 2 [Source:MGI Symbol;Acc:MG:1921692]
2.60E-88	1.10E-85	Plk2	20620 polo like kinase 2 [Source:MGI Symbol;Acc:MG:1099790]
3.76E-88	1.56E-85	Csf1	12977 colony stimulating factor 1 (macrophage) [Source:MGI Symbol;Acc:
8.74E-87	3.51E-84	Tbc1d2	381605 TBC1 domain family, member 2 [Source:MGI Symbol;Acc:MG:26528
1.86E-86	7.25E-84	Kihl21	242785 kelch-like 21 [Source:MGI Symbol;Acc:MG:1919288]
1.03E-85	3.93E-83	Nipal1	70701 NIPA-like domain containing 1 [Source:MGI Symbol;Acc:MG:191795
6.70E-84	2.53E-81	Hoxb9	15417 homeobox B9 [Source:MGI Symbol;Acc:MG:96190]
4.97E-82	1.82E-79	Wwp1	107568 WW domain containing E3 ubiquitin protein ligase 1 [Source:MGI Sy
6.67E-82	2.37E-79	Amot	27494 angiominin [Source:MGI Symbol;Acc:MG:108440]
1.71E-79	5.82E-77	Spire1	68166 spire type actin nucleation factor 1 [Source:MGI Symbol;Acc:MG:19
2.98E-79	1.00E-76	Cflar	12633 CASP8 and FADD-like apoptosis regulator [Source:MGI Symbol;Acc:
3.89E-78	1.22E-75	Sdc3	20970 syndecan 3 [Source:MGI Symbol;Acc:MG:1349163]
7.42E-78	2.30E-75	Prkx	19108 protein kinase, X-linked [Source:MGI Symbol;Acc:MG:1309999]
2.17E-77	6.65E-75	Csf3	12985 colony stimulating factor 3 (granulocyte) [Source:MGI Symbol;Acc:M
1.97E-76	5.96E-74	Ifit2	15958 interferon-induced protein with tetratricopeptide repeats 2 [Sou
1.96E-75	5.78E-73	Tulp4	68842 tubby like protein 4 [Source:MGI Symbol;Acc:MG:1916092]
7.86E-75	2.29E-72	Cpe	12876 carboxypeptidase E [Source:MGI Symbol;Acc:MG:101932]
4.13E-73	1.19E-70	Nectin1	58235 nectin cell adhesion molecule 1 [Source:MGI Symbol;Acc:MG:1926
3.19E-72	8.58E-70	Inhba	16323 inhibin beta-A [Source:MGI Symbol;Acc:MG:96570]
4.12E-72	1.10E-69	Galnt18	233733 polypeptide N-acetylgalactosaminyltransferase 18 [Source:MGI Syn
6.08E-71	1.59E-68	Zcchc2	227449 zinc finger, CCHC domain containing 2 [Source:MGI Symbol;Acc:MG
1.44E-70	3.71E-68	Fosl2	14284 fos-like antigen 2 [Source:MGI Symbol;Acc:MG:102858]
2.35E-70	6.01E-68	Trpv2	22368 transient receptor potential cation channel, subfamily V, member 2
5.97E-68	1.46E-65	Antxr1	69538 anthrax toxin receptor 1 [Source:MGI Symbol;Acc:MG:1916788]
1.03E-67	2.51E-65	B4galnt1	14421 beta-1,4-N-acetyl-galactosaminyl transferase 1 [Source:MGI Symbo
1.56E-67	3.70E-65	Fzd5	14367 frizzled class receptor 5 [Source:MGI Symbol;Acc:MG:108571]
1.91E-67	4.51E-65	Ahr	11624 aryl-hydrocarbon receptor repressor [Source:MGI Symbol;Acc:MG:1
5.66E-67	1.32E-64	Igf1r	16001 insulin-like growth factor I receptor [Source:MGI Symbol;Acc:MG:9
7.87E-66	1.74E-63	Acsf6	216739 acyl-CoA synthetase long-chain family member 6 [Source:MGI Synt
5.45E-65	1.15E-62	Smurf1	75788 SMAD specific E3 ubiquitin protein ligase 1 [Source:MGI Symbol;Acc
1.57E-64	3.25E-62	Prkab2	108097 protein kinase, AMP-activated, beta 2 non-catalytic subunit [Source
6.07E-64	1.25E-61	Ereg	13874 epi-regulin [Source:MGI Symbol;Acc:MG:107508]
1.07E-63	2.18E-61	Rnd1	223881 rho family GTPase 1 [Source:MGI Symbol;Acc:MG:2444878]
1.57E-63	3.18E-61	Tbs1	21825 thrombospondin 1 [Source:MGI Symbol;Acc:MG:98737]
2.66E-63	5.35E-61	Dusp6	67603 dual specificity phosphatase 6 [Source:MGI Symbol;Acc:MG:191485
5.77E-62	1.13E-59	Gnaq	14682 guanine nucleotide binding protein, alpha q polypeptide [Source:MG
6.50E-62	1.26E-59	Tnfrsf10b	21933 tumor necrosis factor receptor superfamily, member 10b [Source:MG
3.58E-61	6.80E-59	Ccnd2	12444 cyclin D2 [Source:MGI Symbol;Acc:MG:88314]
9.95E-61	1.83E-58	Cyr61	NA NA
4.60E-60	8.36E-58	Cap2	67252 CAP, adenylate cyclase-associated protein, 2 (yeast) [Source:MGI Sy
1.39E-58	2.44E-56	Ica1l	70375 islet cell autoantigen 1-like [Source:MGI Symbol;Acc:MG:1917625]
1.54E-58	2.70E-56	Gms3	NA predicted gene 53 [Source:MGI Symbol;Acc:MG:2684899]
2.44E-58	4.24E-56	Ilgav	16410 integrin alpha V [Source:MGI Symbol;Acc:MG:96608]
8.38E-58	1.43E-55	Soat1	20652 sterol O-acyltransferase 1 [Source:MGI Symbol;Acc:MG:104665]
3.40E-57	5.75E-55	Ncs1	14299 neuronal calcium sensor 1 [Source:MGI Symbol;Acc:MG:109166]
5.48E-57	9.20E-55	Klf6	23849 Kruppel-like factor 6 [Source:MGI Symbol;Acc:MG:1346318]
9.52E-57	1.59E-54	Tnfrsf10b	21929 tumor necrosis factor, alpha-induced protein 3 [Source:MGI Symbol
1.15E-56	1.90E-54	Akr1c18	105349 aldo-keto reductase family 1, member C18 [Source:MGI Symbol;Acc
1.53E-56	2.49E-54	Cpne2	234577 copine II [Source:MGI Symbol;Acc:MG:2387578]
1.95E-56	3.17E-54	Rasa4	54153 RAS p21 protein activator 4 [Source:MGI Symbol;Acc:MG:1858600]
3.55E-56	5.69E-54	Lingo1	235402 leucine rich repeat and Ig domain containing 1 [Source:MGI Symbol
1.63E-54	2.46E-52	Hmga1b	111241 high mobility group AT-hook 1B [Source:MGI Symbol;Acc:MG:96163
2.60E-54	3.90E-52	Frm4a	209630 FERM domain containing 4A [Source:MGI Symbol;Acc:MG:1919850]
2.88E-54	4.30E-52	Fmn1	14260 formin 1 [Source:MGI Symbol;Acc:MG:101815]
7.62E-54	1.13E-51	Sun2	223697 Sad1 and UNC84 domain containing 2 [Source:MGI Symbol;Acc:MG:
4.57E-53	6.70E-51	Plpp1	19012 phospholipid phosphatase 1 [Source:MGI Symbol;Acc:MG:108412]
6.97E-52	1.01E-49	Tll1	21892 tolloid-like [Source:MGI Symbol;Acc:MG:106923]
1.19E-51	1.71E-49	Myo1e	71602 myosin IE [Source:MGI Symbol;Acc:MG:106621]
1.94E-51	2.75E-49	Zmat3	22401 zinc finger matrin type 3 [Source:MGI Symbol;Acc:MG:1195270]
2.01E-51	2.83E-49	Heca	380629 hdc homolog, cell cycle regulator [Source:MGI Symbol;Acc:MG:268
3.29E-51	4.60E-49	Hs6st2	50786 heparan sulfate 6-O-sulfotransferase 2 [Source:MGI Symbol;Acc:MG
1.07E-50	1.47E-48	Sema3e	20349 sema domain, immunoglobulin domain (Ig), short basic domain, se
1.11E-50	1.50E-48	Hmga1	15361 high mobility group AT-hook 1 [Source:MGI Symbol;Acc:MG:96160]
1.28E-49	1.68E-47	Plexa1	18844 plexin A1 [Source:MGI Symbol;Acc:MG:107685]
3.16E-49	4.10E-47	Fyn	14360 Fyn proto-oncogene [Source:MGI Symbol;Acc:MG:95602]
4.50E-49	5.78E-47	Adra2a	11551 adrenergic receptor, alpha 2a [Source:MGI Symbol;Acc:MG:87934]
5.08E-49	6.45E-47	Crim1	50766 cysteine rich transmembrane BMP regulator 1 (chordin like) [Source
1.82E-48	2.28E-46	Ptchd4	627625 patched domain containing 4 [Source:MGI Symbol;Acc:MG:1920485
2.19E-48	2.69E-46	Txnrd1	50493 thioredoxin reductase 1 [Source:MGI Symbol;Acc:MG:1354175]
2.23E-48	2.73E-46	Spg20	229285 spastic paraplegia 20, spartin (Troyer syndrome) homolog (human)
5.51E-48	6.62E-46	Ripor2	193385 RHO family interacting cell polarization regulator 2 [Source:MGI Syr
8.01E-48	9.57E-46	Megf10	70417 multiple EGF-like-domains 10 [Source:MGI Symbol;Acc:MG:268517
1.69E-47	1.99E-45	Ctgf	NA NA
2.18E-47	2.55E-45	S100a7a	381493 S100 calcium binding protein A7A [Source:MGI Symbol;Acc:MG:268
3.15E-47	3.66E-45	Smad7	17131 SMAD family member 7 [Source:MGI Symbol;Acc:MG:1100518]
3.99E-47	4.62E-45	Syn1	20964 synapsin I [Source:MGI Symbol;Acc:MG:98460]
1.70E-46	1.94E-44	Nabp1	109019 nucleic acid binding protein 1 [Source:MGI Symbol;Acc:MG:192325]

Upregulated in 50:50/9*10			
pvalue	padj	mgi_symb	entrezgen description
2.73E-145	5.84E-141	Cxadr	13052 coxsackie virus and adenovirus receptor [Source:MGI Symbol;Acc:27332]
2.32E-124	2.49E-120	Ifi2712a	76933 interferon, alpha-inducible protein 27 like 2A [Source:MGI Symbol;Acc:396E-101]
3.96E-101	2.82E-97	Irgm1	15944 immunity-related GTPase family M member 1 [Source:MGI Symbol;Acc:7.79E-81]
4.16E-77	1.12E-74	Il22ra1	230828 interleukin 22 receptor, alpha 1 [Source:MGI Symbol;Acc:MGI:266;4.12E-78]
1.47E-74	1.47E-74	Hal	15109 histidine ammonia lyase [Source:MGI Symbol;Acc:MGI:96010]
6.69E-77	2.04E-73	C2	12263 complement component 2 (within H-2S) [Source:MGI Symbol;Acc:9.93E-71]
2.65E-67	1.87E-61	Isyn1	71780 myo-inositol 1-phosphate synthase A1 [Source:MGI Symbol;Acc:M:7.87E-65]
1.87E-61	1.87E-61	Amigo2	105827 adhesion molecule with Ig like domain 2 [Source:MGI Symbol;Acc:1.18E-61]
2.53E-58	1.42E-56	Tgtp1	21822 T cell specific GTPase 1 [Source:MGI Symbol;Acc:MGI:98734]
7.95E-60	1.42E-56	Gdpd2	71584 glycerophosphodiester phosphodiesterase domain containing 2 [Source:MGI Symbol;Acc:1.07E-59]
1.76E-56	1.76E-56	Palmd	114301 palmdelphin [Source:MGI Symbol;Acc:MGI:2148896]
3.30E-53	4.42E-50	Bmp4	12159 bone morphogenetic protein 4 [Source:MGI Symbol;Acc:MGI:8818]
4.76E-53	5.99E-50	C4b	12268 complement component 4B (Chido blood group) [Source:MGI Symbol;Acc:6.75E-53]
8.02E-50	4.80E-47	Adamts9	101401 a disintegrin-like and metalloproteinase (reprolysin type) with thrombospondin type 1 motifs [Source:MGI Symbol;Acc:MGI:1347476]
4.80E-47	4.80E-47	Foxa2	15376 forkhead box A2 [Source:MGI Symbol;Acc:MGI:1347476]
1.32E-49	1.41E-46	Apol9b	71898 apolipoprotein L 9b [Source:MGI Symbol;Acc:MGI:1919148]
1.41E-49	1.44E-46	Ptger3	19218 prostaglandin E receptor 3 (subtype EP3) [Source:MGI Symbol;Acc:3.10E-48]
3.01E-45	3.01E-45	Sp110	109032 Sp110 nuclear body protein [Source:MGI Symbol;Acc:MGI:1923364]
1.37E-40	1.37E-40	Spsb1	74646 splanchnin receptor domain and SOCS box containing 1 [Source:MGI Symbol;Acc:1.26E-42]
9.96E-40	9.96E-40	Igf3	16009 insulin-like growth factor binding protein 3 [Source:MGI Symbol;Acc:1.63E-42]
1.24E-39	1.24E-39	Dpysl5	65254 dihydropyrimidinase-like 5 [Source:MGI Symbol;Acc:MGI:1929722]
1.88E-39	1.88E-39	Zbtb7c	207259 zinc finger and BTB domain containing 7C [Source:MGI Symbol;Acc:9.98E-42]
7.12E-39	7.12E-39	Fam110c	104943 family with sequence similarity 110, member C [Source:MGI Symbol;Acc:8.21E-41]
5.66E-38	5.66E-38	Pcnx2	270109 pecanex homolog 2 [Source:MGI Symbol;Acc:MGI:2445010]
6.14E-37	6.14E-37	Gm14226	50518 predicted gene 14226 [Source:MGI Symbol;Acc:MGI:3649244]
2.70E-36	2.70E-36	Z310030G06	66952 RIKEN cDNA Z310030G06 gene [Source:MGI Symbol;Acc:MGI:19142]
5.55E-35	5.55E-35	Cttnbp2	30785 cortactin binding protein 2 [Source:MGI Symbol;Acc:MGI:1353467]
4.05E-32	4.05E-32	Irf7	54123 interferon regulatory factor 7 [Source:MGI Symbol;Acc:MGI:18592]
4.86E-32	4.86E-32	Apol9a	223672 apolipoprotein L 9a [Source:MGI Symbol;Acc:MGI:3606001]
1.05E-31	1.05E-31	Sema4a	20351 sema domain, immunoglobulin domain (Ig), transmembrane domain [Source:MGI Symbol;Acc:5.00E-34]
2.55E-31	2.55E-31	Stxbp2	20911 syntaxin binding protein 2 [Source:MGI Symbol;Acc:MGI:107370]
1.49E-30	1.49E-30	Rcsd1	226594 RCS domain containing 1 [Source:MGI Symbol;Acc:MGI:2676394]
2.32E-30	2.32E-30	Arhgap45	70719 Rho GTPase activating protein 45 [Source:MGI Symbol;Acc:MGI:19121E-32]
5.61E-30	5.61E-30	Zbtb8b	215627 zinc finger and BTB domain containing 8b [Source:MGI Symbol;Acc:3.68E-31]
1.64E-28	1.64E-28	Fam180a	208164 family with sequence similarity 180, member A [Source:MGI Symbol;Acc:8.65E-31]
3.63E-28	3.63E-28	Kif26b	269152 kinesin family member 26B [Source:MGI Symbol;Acc:MGI:2447076]
4.00E-28	4.00E-28	Il18bp	16068 interleukin 18 binding protein [Source:MGI Symbol;Acc:MGI:13338]
8.47E-28	8.47E-28	Tgtp2	1E+08 T cell specific GTPase 2 [Source:MGI Symbol;Acc:MGI:3710083]
1.04E-27	1.04E-27	Trf	22041 transferrin [Source:MGI Symbol;Acc:MGI:98821]
3.56E-27	3.56E-27	Fam83g	69640 family with sequence similarity 83, member G [Source:MGI Symbol;Acc:1.04E-29]
3.92E-27	3.92E-27	Cldn10	58187 claudin 10 [Source:MGI Symbol;Acc:MGI:1913101]
4.02E-27	4.02E-27	Phf11b	236451 PHD finger protein 11B [Source:MGI Symbol;Acc:MGI:3645789]
4.23E-27	4.23E-27	Pnoc	18155 prepronociceptin [Source:MGI Symbol;Acc:MGI:105308]
1.08E-26	1.08E-26	Aqp5	11830 aquaporin 5 [Source:MGI Symbol;Acc:MGI:106215]
1.68E-25	1.68E-25	Aldh1b1	72535 aldehyde dehydrogenase 1 family, member B1 [Source:MGI Symbol;Acc:7.78E-28]
2.56E-25	2.56E-25	Plscr2	18828 phospholipid scramblase 2 [Source:MGI Symbol;Acc:MGI:1270860]
6.68E-25	6.68E-25	Rasgrf2	19418 RAS protein-specific guanine nucleotide-releasing factor 2 [Source:MGI Symbol;Acc:2.14E-27]
6.83E-25	6.83E-25	Tmem51	214359 transmembrane protein 51 [Source:MGI Symbol;Acc:MGI:2384874]
7.84E-23	7.84E-23	Myo5b	17919 myosin VB [Source:MGI Symbol;Acc:MGI:106598]
8.13E-23	8.13E-23	Cables1	63955 CDKs and Abl enzyme substrate 1 [Source:MGI Symbol;Acc:MGI:15294E-25]
8.50E-23	8.50E-23	Gm26809	NA NA
8.54E-23	8.54E-23	Slc39a8	67547 solute carrier family 39 (metal ion transporter), member 8 [Source:MGI Symbol;Acc:1.46E-24]
4.11E-22	4.11E-22	Herc6	67138 hect domain and RLD 6 [Source:MGI Symbol;Acc:MGI:1914388]
4.88E-22	4.88E-22	Adar	56417 adenosine deaminase, RNA-specific [Source:MGI Symbol;Acc:MGI:3.29E-24]
6.68E-22	6.68E-22	Pkdcc	106522 protein kinase domain containing, cytoplasmic [Source:MGI Symbol;Acc:2.64E-23]
6.55E-21	6.55E-21	Ddx4	13206 DEAD box helicase 4 [Source:MGI Symbol;Acc:MGI:102670]
8.04E-21	8.04E-21	Mmp23	26561 matrix metalloproteinase 23 [Source:MGI Symbol;Acc:MGI:1347361]
8.62E-21	8.62E-21	Sp100	20684 nuclear antigen Sp100 [Source:MGI Symbol;Acc:MGI:109561]
1.25E-20	1.25E-20	Ly6c1	17067 lymphocyte antigen 6 complex, locus C1 [Source:MGI Symbol;Acc:6.51E-23]
1.53E-20	1.53E-20	Sh2d5	230863 SH2 domain containing 5 [Source:MGI Symbol;Acc:MGI:2446215]
1.53E-20	1.53E-20	Itgb4	192897 integrin beta 4 [Source:MGI Symbol;Acc:MGI:96613]
1.76E-20	1.76E-20	Oas1a	246730 2'-5' oligoadenylate synthetase 1A [Source:MGI Symbol;Acc:MGI:28.15E-23]
1.85E-20	1.85E-20	Bmp1	12153 bone morphogenetic protein 1 [Source:MGI Symbol;Acc:MGI:8817]
3.37E-20	3.37E-20	Clcn3	12725 chloride channel, voltage-sensitive 3 [Source:MGI Symbol;Acc:MGI:3.43E-22]
7.40E-20	7.40E-20	H2-Q6	110557 histocompatibility 2, Q region locus 6 [Source:MGI Symbol;Acc:MGI:4.36E-22]
9.33E-20	9.33E-20	Inava	67313 innate immunity activator [Source:MGI Symbol;Acc:MGI:1921579]
1.67E-19	1.67E-19	Ptpn13	19249 protein tyrosine phosphatase, non-receptor type 13 [Source:MGI Symbol;Acc:8.21E-22]
1.70E-19	1.70E-19	Oasl1	231655 2'-5' oligoadenylate synthetase-like 1 [Source:MGI Symbol;Acc:MGI:9.90E-22]
2.04E-19	2.04E-19	1010001N	NA NA
2.10E-19	2.10E-19	Arhgef28	110596 Rho guanine nucleotide exchange factor (GEF) 28 [Source:MGI Symbol;Acc:1.19E-21]
2.38E-19	2.38E-19	Dennd2d	72121 DENN/MADD domain containing 2D [Source:MGI Symbol;Acc:MGI:2.47E-21]
4.85E-19	4.85E-19	Tkfc	225913 triokinase, FMN cyclase [Source:MGI Symbol;Acc:MGI:2385084]
4.97E-19	4.97E-19	Gata6	14465 GATA binding protein 6 [Source:MGI Symbol;Acc:MGI:107516]
5.03E-19	5.03E-19	Lamc3	23928 laminin gamma 3 [Source:MGI Symbol;Acc:MGI:1344394]
5.83E-19	5.83E-19	Slc9a3r1	26941 solute carrier family 9 (sodium/hydrogen exchanger), member 3 [Source:MGI Symbol;Acc:7.85E-21]
1.45E-18	1.45E-18	Met	17295 met proto-oncogene [Source:MGI Symbol;Acc:MGI:96969]
1.48E-18	1.48E-18	Rnf122	68867 ring finger protein 122 [Source:MGI Symbol;Acc:MGI:1916117]
1.74E-18	1.74E-18	Serp1	12258 serine (or cysteine) peptidase inhibitor, clade G, member 1 [Source:MGI Symbol;Acc:1.02E-20]
1.83E-18	1.83E-18	Eif2ak2	19106 eukaryotic translation initiation factor 2-alpha kinase 2 [Source:MGI Symbol;Acc:1.32E-20]
2.35E-18	2.35E-18	Gm18853	NA NA
4.61E-18	4.61E-18	Pcsk9	100102 proprotein convertase subtilisin/kexin type 9 [Source:MGI Symbol;Acc:2.80E-20]
4.90E-18	4.90E-18	Nfe2l3	18025 nuclear factor, erythroid derived 2, like 3 [Source:MGI Symbol;Acc:2.91E-20]
5.05E-18	5.05E-18	Il1r1	16177 interleukin 1 receptor, type 1 [Source:MGI Symbol;Acc:MGI:96545]
7.10E-18	7.10E-18	Nmi	64685 N-myc (and STAT) interactor [Source:MGI Symbol;Acc:MGI:192836]
7.93E-18	7.93E-18	Rtn1	104001 reticulon 1 [Source:MGI Symbol;Acc:MGI:1933947]
8.59E-18	8.59E-18	Parp12	243771 poly (ADP-ribose) polymerase family, member 12 [Source:MGI Symbol;Acc:6.06E-20]
1.00E-17	1.00E-17	Has2	15117 hyaluronan synthase 2 [Source:MGI Symbol;Acc:MGI:107821]
1.61E-17	1.61E-17	Nupr1	56312 nuclear protein transcription regulator 1 [Source:MGI Symbol;Acc:1.72E-19]
2.80E-17	2.80E-17	Dlx4	13394 distal-less homeobox 4 [Source:MGI Symbol;Acc:MGI:94904]
3.98E-17	3.98E-17	Gm15675	NA predicted gene 15675 [Source:MGI Symbol;Acc:MGI:3783117]
4.56E-17	4.56E-17	Gm29371	NA predicted gene 29371 [Source:MGI Symbol;Acc:MGI:5580077]
5.13E-17	5.13E-17	Gm15222	1.03E+08 predicted gene 15222 [Source:MGI Symbol;Acc:MGI:3705297]
5.13E-17	5.13E-17	Stk26	70415 serine/threonine kinase 26 [Source:MGI Symbol;Acc:MGI:1917665]
6.74E-17	6.74E-17	Lgr5	14160 leucine rich repeat containing G protein coupled receptor 5 [Source:MGI Symbol;Acc:4.60E-19]
7.13E-17	7.13E-17	Plac8	231507 placenta-specific 8 [Source:MGI Symbol;Acc:MGI:2445289]
8.99E-17	8.99E-17	Oas1g	23960 2'-5' oligoadenylate synthetase 1G [Source:MGI Symbol;Acc:MGI:9.704E-19]
1.08E-16	1.08E-16	Ihfh1	71586 interferon induced with helicase C domain 1 [Source:MGI Symbol;Acc:7.23E-19]
1.10E-16	1.10E-16	Oas3	246727 2'-5' oligoadenylate synthetase 3 [Source:MGI Symbol;Acc:MGI:218.78E-19]
1.31E-16	1.31E-16	Scarb1	20778 scavenger receptor class B, member 1 [Source:MGI Symbol;Acc:MGI:9.06E-19]
1.34E-16	1.34E-16	Plat	18791 plasminogen activator, tissue [Source:MGI Symbol;Acc:MGI:97610]

Downregulated in 50:50*10				
pvalue	padj	mgi_symb	entrezgen	description
3.58E-80	1.53E-76	mt-Te	NA	mitochondrially encoded tRNA glutamic acid [Source:MGI Symbol]
1.30E-60	2.53E-57	Nrcam	319504	neuronal cell adhesion molecule [Source:MGI Symbol;Acc:MGI:10]
1.28E-56	1.96E-53	Lingo1	235402	leucine rich repeat and Ig domain containing 1 [Source:MGI Symbe]
1.39E-55	1.99E-52	Ahrr	11624	aryl-hydrocarbon receptor repressor [Source:MGI Symbol;Acc:MGI]
4.01E-46	3.73E-43	Smad6	17130	SMAD family member 6 [Source:MGI Symbol;Acc:MGI:1336883]
7.19E-46	6.41E-43	Ace	11421	angiotensin I converting enzyme (peptidyl-dipeptidase A) 1 [Sou
6.62E-44	5.66E-41	mt-Nd6	17722	mitochondrially encoded NADH dehydrogenase 6 [Source:MGI Syr
1.73E-37	1.06E-34	Gldn	235379	gliomedin [Source:MGI Symbol;Acc:MGI:2388361]
7.34E-36	4.36E-33	Pkd2	18764	polycystin 2, transient receptor potential cation channel [Source:M
1.62E-35	9.38E-33	Anpep	16790	alanyl (membrane) aminopeptidase [Source:MGI Symbol;Acc:MGI]
9.09E-35	4.86E-32	mt-Nd4	17719	mitochondrially encoded NADH dehydrogenase 4 [Source:MGI Syr
7.61E-33	3.61E-30	Peli2	93834	pellino 2 [Source:MGI Symbol;Acc:MGI:1891445]
7.61E-33	3.61E-30	Peli2	624367	pellino 2 [Source:MGI Symbol;Acc:MGI:1891445]
6.14E-32	2.79E-29	Tbx20	57246	T-box 20 [Source:MGI Symbol;Acc:MGI:1888496]
3.97E-31	1.73E-28	Spp1	20750	secreted phosphoprotein 1 [Source:MGI Symbol;Acc:MGI:98389]
4.90E-31	2.09E-28	Serpine2	20720	serine (or cysteine) peptidase inhibitor, clade E, member 2 [Sou
7.65E-30	2.98E-27	mt-Nd2	17717	mitochondrially encoded NADH dehydrogenase 2 [Source:MGI Syr
3.73E-29	1.31E-26	Xytl1	268880	xyloside xylosyltransferase 1 [Source:MGI Symbol;Acc:MGI:214644]
5.07E-28	1.72E-25	Tmem179	104885	transmembrane protein 179 [Source:MGI Symbol;Acc:MGI:214489]
5.98E-28	2.00E-25	Shisa4	77552	shisa family member 4 [Source:MGI Symbol;Acc:MGI:1924802]
2.72E-27	8.55E-25	Smad7	17131	SMAD family member 7 [Source:MGI Symbol;Acc:MGI:1100518]
1.66E-26	5.13E-24	Nog	18121	noggin [Source:MGI Symbol;Acc:MGI:104327]
2.92E-26	8.93E-24	Smad9	55994	SMAD family member 9 [Source:MGI Symbol;Acc:MGI:1859993]
3.28E-26	9.89E-24	Nqo1	18104	NAD(P)H dehydrogenase, quinone 1 [Source:MGI Symbol;Acc:MGI]
1.60E-24	4.45E-22	Atoh8	71093	atonal bHLH transcription factor 8 [Source:MGI Symbol;Acc:MGI:15]
1.70E-24	4.67E-22	Prrx2	20204	paired related homeobox 2 [Source:MGI Symbol;Acc:MGI:98218]
1.83E-24	4.88E-22	Txnrd1	50493	thioredoxin reductase 1 [Source:MGI Symbol;Acc:MGI:1354175]
3.37E-24	8.80E-22	Id1	15901	inhibitor of DNA binding 1, HLH protein [Source:MGI Symbol;Acc:M
5.73E-24	1.48E-21	Rarres1	109222	retinoic acid receptor responder (tazarotene induced) 1 [Source:M
8.81E-24	2.24E-21	Cdh13	12554	cadherin 13 [Source:MGI Symbol;Acc:MGI:99551]
1.29E-23	3.23E-21	Abhd17c	70178	abhydrolase domain containing 17C [Source:MGI Symbol;Acc:MGI]
7.95E-23	1.83E-20	Pparg	19016	peroxisome proliferator activated receptor gamma [Source:MGI S
8.30E-23	1.87E-20	Slc25a12	78830	solute carrier family 25 (mitochondrial carrier, Aralar), member 12
2.28E-22	5.02E-20	Nr1d2	353187	nuclear receptor subfamily 1, group D, member 2 [Source:MGI Syn
2.96E-22	6.47E-20	Gpc1	14733	glypican 1 [Source:MGI Symbol;Acc:MGI:1194891]
6.63E-22	1.40E-19	Mfap3l	71306	microfibrillar-associated protein 3-like [Source:MGI Symbol;Acc:M
1.18E-21	2.38E-19	Pgrmc1	53328	progesterone receptor membrane component 1 [Source:MGI Sym
2.02E-21	3.99E-19	Dpt	56429	dermatopontin [Source:MGI Symbol;Acc:MGI:1928392]
2.74E-21	5.23E-19	Csf2rb	12983	colony stimulating factor 2 receptor, beta, low-affinity (granuloc
3.25E-21	6.10E-19	Kif2a	16563	kinesin family member 2A [Source:MGI Symbol;Acc:MGI:108390]
3.28E-21	6.10E-19	Slc2a13	239606	solute carrier family 2 (facilitated glucose transporter), member 1
3.78E-20	6.52E-18	Ngef	53972	neuronal guanine nucleotide exchange factor [Source:MGI Symbo
5.35E-20	8.94E-18	Bean1	65115	brain expressed, associated with Nedd4, 1 [Source:MGI Symbol;A
1.73E-19	2.80E-17	Itgbl1	223272	integrin, beta-like 1 [Source:MGI Symbol;Acc:MGI:2443439]
7.28E-19	1.10E-16	Cited2	17684	Cbp/p300-interacting transactivator, with Glu/Asp-rich carboxy-te
1.85E-18	2.63E-16	Tspan17	74257	tetraspanin 17 [Source:MGI Symbol;Acc:MGI:1921507]
2.65E-18	3.70E-16	Syndig1	433485	synapse differentiation inducing 1 [Source:MGI Symbol;Acc:MGI:3
3.49E-18	4.79E-16	Rcn2	26611	reticulocalbin 2 [Source:MGI Symbol;Acc:MGI:1349765]
4.88E-18	6.60E-16	Ndrgr4	234593	N-myc downstream regulated gene 4 [Source:MGI Symbol;Acc:MG
6.95E-18	9.23E-16	Sgms2	74442	sphingomyelin synthase 2 [Source:MGI Symbol;Acc:MGI:1921692]
1.20E-17	1.58E-15	Col6a3	12835	collagen, type VI, alpha 3 [Source:MGI Symbol;Acc:MGI:88461]
1.52E-17	1.96E-15	Cobl1	319876	Cobl-like 1 [Source:MGI Symbol;Acc:MGI:2442894]
1.53E-17	1.97E-15	Clec4d	17474	C-type lectin domain family 4, member d [Source:MGI Symbol;Acc
1.69E-17	2.16E-15	Id3	15903	inhibitor of DNA binding 3 [Source:MGI Symbol;Acc:MGI:96398]
2.35E-17	2.97E-15	mt-Cytb	17711	mitochondrially encoded cytochrome b [Source:MGI Symbol;Acc:M
4.10E-17	5.13E-15	Nanos1	332397	nanos C2HC-type zinc finger 1 [Source:MGI Symbol;Acc:MGI:26692]
7.42E-17	9.01E-15	Plexd1	72324	plexin domain containing 1 [Source:MGI Symbol;Acc:MGI:1919574]
7.75E-17	9.31E-15	Lrp12	239393	low density lipoprotein-related protein 12 [Source:MGI Symbol;A
7.71E-17	9.31E-15	Alcam	11658	activated leukocyte cell adhesion molecule [Source:MGI Symbol;A
7.94E-17	9.48E-15	Tmem267	633640	transmembrane protein 267 [Source:MGI Symbol;Acc:MGI:364854]
9.24E-17	1.10E-14	Reep3	28193	receptor accessory protein 3 [Source:MGI Symbol;Acc:MGI:88990]
1.29E-16	1.49E-14	Cobl	12808	cordons-bleu WH2 repeat [Source:MGI Symbol;Acc:MGI:105056]
1.95E-16	2.23E-14	Kazald1	107250	Kazal-type serine peptidase inhibitor domain 1 [Source:MGI Symb
2.14E-16	2.41E-14	Spire1	68166	spire type actin nucleation factor 1 [Source:MGI Symbol;Acc:MGI:1
2.20E-16	2.46E-14	Ece2	107522	endothelin converting enzyme 2 [Source:MGI Symbol;Acc:MGI:111
5.04E-16	5.44E-14	Clstn1	65945	calsyntenin 1 [Source:MGI Symbol;Acc:MGI:1929895]
5.30E-16	5.70E-14	Gm28439	NA	predicted gene 28439 [Source:MGI Symbol;Acc:MGI:5579145]
1.78E-15	1.79E-13	E2f1	13555	E2F transcription factor 1 [Source:MGI Symbol;Acc:MGI:101941]
2.06E-15	2.05E-13	Gm9780	NA	NA
2.27E-15	2.25E-13	Ogfr1	70155	opioid growth factor receptor-like 1 [Source:MGI Symbol;Acc:MGI]
2.81E-15	2.76E-13	Crtf1	12931	cytokine receptor-like factor 1 [Source:MGI Symbol;Acc:MGI:13400]
4.04E-15	3.89E-13	Sh3bp5	24056	SH3-domain binding protein 5 (BTK-associated) [Source:MGI Symb
4.21E-15	4.02E-13	Golm4	73124	golgi integral membrane protein 4 [Source:MGI Symbol;Acc:MGI:1
4.68E-15	4.42E-13	Inhbb	16324	inhibin beta-B [Source:MGI Symbol;Acc:MGI:96571]
4.83E-15	4.53E-13	4930447F2	76873	RIKEN cDNA 4930447F2 gene [Source:MGI Symbol;Acc:MGI:19241]
4.90E-15	4.56E-13	Dlx2	13392	distal-less homeobox 2 [Source:MGI Symbol;Acc:MGI:94902]
6.90E-15	6.36E-13	Cst6	73720	cystatin E/M [Source:MGI Symbol;Acc:MGI:1920970]
7.27E-15	6.65E-13	Tent4b	214627	terminal nucleotidyltransferase 4B [Source:MGI Symbol;Acc:MGI:1
7.71E-15	6.99E-13	Akr1c18	105349	aldo-keto reductase family 1, member C18 [Source:MGI Symbol;A
9.03E-15	8.04E-13	Cped1	214642	cadherin-like and PC-esterase domain containing 1 [Source:MGI S
9.28E-15	8.24E-13	Gnaq	14682	guanine nucleotide binding protein, alpha q polypeptide [Source:
9.96E-15	8.80E-13	Sp6	83395	trans-acting transcription factor 6 [Source:MGI Symbol;Acc:MGI:19
1.01E-14	8.92E-13	Gm42517	1.15E+08	predicted gene 42517 [Source:MGI Symbol;Acc:MGI:5662654]
1.09E-14	9.52E-13	Ank	11732	progressive ankylosis [Source:MGI Symbol;Acc:MGI:3045421]
1.21E-14	1.06E-12	Eef1a2	13628	eukaryotic translation elongation factor 1 alpha 2 [Source:MGI Syn
1.32E-14	1.14E-12	Mmp12	17381	matrix metalloproteinase 12 [Source:MGI Symbol;Acc:MGI:97005]
1.74E-14	1.50E-12	Satb2	212712	special AT-rich sequence binding protein 2 [Source:MGI Symbol;A
1.78E-14	1.51E-12	Arf6ip5	65106	ADP-ribosylation factor-like 6 interacting protein 5 [Source:MGI S
3.05E-14	2.56E-12	Oncut2	225631	one cut domain, family member 2 [Source:MGI Symbol;Acc:MGI:11]
3.19E-14	2.64E-12	Gja3	14611	gap junction protein, alpha 3 [Source:MGI Symbol;Acc:MGI:95714]
3.19E-14	2.64E-12	mt-Nd5	17721	mitochondrially encoded NADH dehydrogenase 5 [Source:MGI Syr
4.45E-14	3.66E-12	Id4	15904	inhibitor of DNA binding 4 [Source:MGI Symbol;Acc:MGI:99414]
4.81E-14	3.92E-12	Nbl1	17965	NBL1, DAN family BMP antagonist [Source:MGI Symbol;Acc:MGI:11
4.88E-14	3.97E-12	Olfm1	56177	olfactomedin 1 [Source:MGI Symbol;Acc:MGI:1860437]
6.54E-14	5.28E-12	Cd53	12508	CD53 antigen [Source:MGI Symbol;Acc:MGI:88341]
7.43E-14	5.97E-12	Plexnc1	54712	plexin C1 [Source:MGI Symbol;Acc:MGI:1890127]
1.22E-13	9.52E-12	Nectin3	58998	nectin cell adhesion molecule 3 [Source:MGI Symbol;Acc:MGI:193
1.63E-13	1.27E-11	Bhlhe41	79362	basic helix-loop-helix family, member e41 [Source:MGI Symbol;A
1.67E-13	1.30E-11	Dlk1	13386	delta like non-canonical Notch ligand 1 [Source:MGI Symbol;Acc:N
1.97E-13	1.52E-11	Grin3a	242443	glutamate receptor ionotropic, NMDA3A [Source:MGI Symbol;Acc

APPENDIX B: PROTOCOLS

ANTIBODY PRODUCTION

Day 1

1. Pick a colony from the H5 plate (with a pipette tip), add it to a flask containing 100 mL of LB media (no agar) with kanamycin media. Reseal the plate with parafilm, leave it in the cold room.
2. Let the colony grow at 37 C overnight shaking at 250 rpm (the default).

If you can start in the morning and come back between 6 and 7 hours afterwards, you can just grow the colony in 1 L volume. The culture will reach the right OD600 by then (check with Nanodrop anyway). This lets you consolidate Day 1 and Day 2 in one work day!

Day 2

1. Using the 2xYT media as a blank, measure the OD600 of the overnight culture. Dilute it with fresh media to obtain one liter (put it in a 2 L glass flask) at OD600 between 0.9 and 1. OD600 is linear, so if you had a stock at about 10, a 1:10 dilution would yield the desired concentration.
2. Add 1 mL of 1M IPTG stock In the -20 freezer. Change the incubator setting to 30 C, let it cool as well.
3. Close the lid and let it shake for 20 to 26 hours. Any shorter incubation may significantly lower your yield.

Day 3

The most labor intensive day

1. Spin down the cultures after balancing four 250 mL bottles at 8000 xg for 10 minutes. Put 50 mL of DI water in the fridge.
2. Filter all the supernatant through the .45 uM large filter bottles, add 1 mL of protease inhibitor and set that bottle aside.

Buffers

Binding buffer for protein L

Make 2 L since you will need to dilute the sample 1:1 and it's the most used buffer every run.

20mM sodium phosphate, 150mM NaCl, correct to pH 7.2

Elution buffer

1 L is fine, just 0.1 M sodium citrate

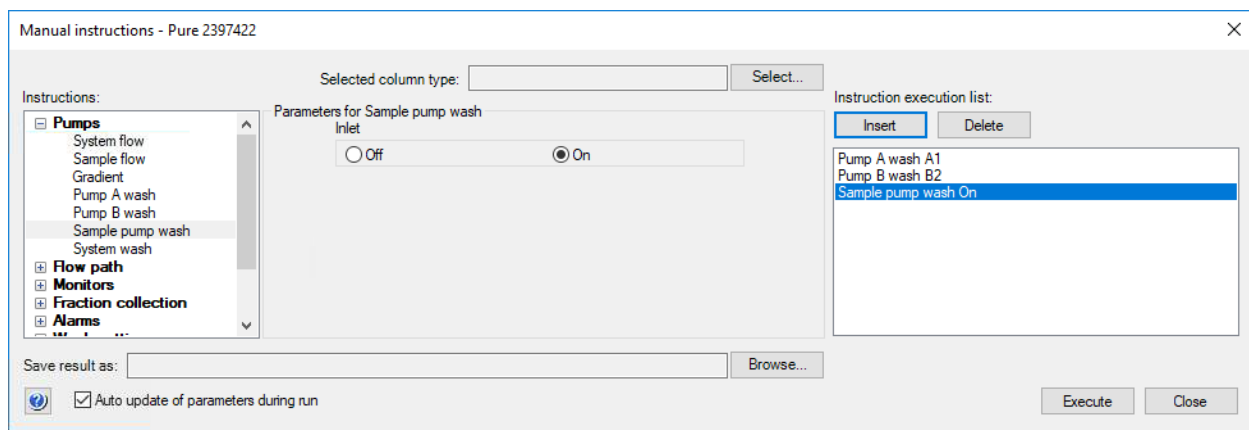
Cleaning-in-place buffer:

Protein L requires binding buffer alternated with 0.15 M NaOH. The program takes care of these switches.

Setting up the HPLC

Log in with TightVNC and the pw. It's a good idea to close out of all the programs if it's your first run for the week. Make sure all the inlets are fishing in 20% Ethanol everytime you start a run.

Double click on UNICORN 7.3, say "OK", go to the System Control panel. Manual > Execute Manual Instructions... > Pumps. Click on each of these options on the left panel, click Insert for each on the right side. Execute.



Press the stop button once it's over and go to the machine to prime the pump heads (4 on main unit, 2 on sample pump, 6 in all). Turn one of the butterfly valves counterclockwise to loosen them. Insert the big syringe and start drawing. When you get buffer flowing with little resistance into the syringe, pull out and tighten the valve. Move on to the next one.

IF you are using a different column from the one inset, do the following via manual instructions.

The image displays a chromatography system interface. At the top, system parameters are shown: System flow 0.000 ml/min, 0.0 %B, and Sample flow 1.000. Below this is a schematic diagram of the system components, including pumps (A1, B1, S), valves (A, B, P, M), a sample pump (SyP), a column (W1 Col), a detector (1), UV, Cond, Restrictor, and Waste. A red arrow points to the column position '1'. Below the diagram is a 'Manual instructions - Pure 2397422' window. The window has a left sidebar with categories: Pumps, Flow path, Monitors, Fraction collection, and Alarms. The 'Pumps' category is expanded, showing sub-items like System flow, Sample flow, Gradient, Pump A wash, Pump B wash, Sample pump wash, and System wash. The 'Sample flow' item is selected. The main area shows 'Parameters for Sample flow' with a 'Flow rate' of 1.000 ml/min and 'Pressure control' set to 'Off'. There are 'Insert' and 'Delete' buttons for the 'Instruction execution list', which currently contains 'Sample flow 1.000, Off'. At the bottom of the window, there is a 'Save result as:' field, a 'Browse...' button, and 'Execute' and 'Close' buttons. A checkbox for 'Auto update of parameters during run' is checked.

Settings: column position “1”; Injection valve set to “Sample pump load”. You can change these from the manual settings screen or by clicking on the corresponding parts on the cartoon above and picking from the options that appear.

This enables a slow dip of ethanol through the column holder position, all the way into the waste tubes. Unscrew it to screw the column in (bottom first) tightly as the 20% ethanol keeps flowing (drop-to-drop method). Screw the top and notice if the fluid now makes it all the way to the waste. If not, try again after removing the column, drying the ethanol and making sure there are no obstructions in those tubes. Otherwise, much closer ready to start.

As you load ~12 collection tubes in the fractionator and align #1 to the dosing arm (lower it gently, like a platter arm), for Protein L purification add 900 uL of 1 M Tris base in order to neutralize the pH of the eluted antibody and preserve it.

For H5 Protein L affinity purification, put the inlets in the following buffers.

A1: into the sodium phosphate buffer (binding buffer)

A2: can stay in 20% ethanol

B1: elution buffer citric acid

B2 cleaning buffer, NaOH

Make sure there is still plenty (100 mL) of Ethanol in those bottles, otherwise refill them before the next run.

Start the 4 hour work with Open -> H5 protein L. Make sure to input a sample volume larger than what you have, the Air Sensor will avoid air intake while you get all of the sample in. Pick a meaningful name for the run and Start it.

NAÏVE MOUSE LUNG FIBROBLASTS

Harvesting mouse lungs

1. Perform primary and secondary euthanasia as described in protocol – e.g. ketamine anesthesia followed by cervical dislocation.
2. Minimize time between animal death and cells placed on ice, which may mean only euthanizing one animal at a time

Digestion Solution (for two whole lungs, from one mouse, multiply as needed)

Final Volume 2mL

Liberase @ 3.9-4.2 units/mL - 300µL of 26u/mL aliquot

DNase @ 750-1000 units/mL – 300µL of 5000u/mL aliquot

Add Sterile PBS to 2 mL

3. Dissect away heart/fat and primary bronchioles from the lung lobes, minimizing non-lobe tissue.
4. Place lung lobes/large chunks into a 1.5ml microfuge tube and insert sterile scissors, chop liberally into tiny chunks.
5. Place tube at 37C for up to 30', shaking every 5 minutes or on a gentle shaker if possible.
6. Place a 100 µm filter into a 50mL tube and pour the Digestion Solution + Lungs onto the filter.

Using a sterile syringe plunger, work the chunks of tissue through the filter.

FOR THE FOLLOWING STEPS, USE THIS MEDIUM: Corning 10-013-CV DMEM [+] 4.5 g/L glucose, L-glutamine, sodium pyruvate. You need to add 20% FBS, 1% PenStrep (both by volume) and most importantly, HEPES at final concentration of 25 µM.

HEPES is not stable long term, so aliquot 50 mL of the above medium and add 1.25 µL of 1M HEPES (you can round up to 2).

7. Flush the filter with warm media, ~7 mL per 3 sets of lungs.
8. Centrifuge at 1200 rpm for 4.5'. Resuspend the pellet in fresh medium, centrifuge again.
9. After last wash, plate cells in T25 or smaller
10. Incubate at 37 C, 5% CO₂ for 1h
11. Remove supernatant, replace with fresh medium. Place supernatant in another vessel, T25 or smaller.

Preparation of cell stocks:

1. Isolate fibroblasts from murine lung using appropriate protocols
2. Plate isolated cells in a T-25 flask (TCPS) in 20% FBS DMEM (see above, no need for HEPES)
3. Change media every other day and check for confluency. The cells will grow fast, so split and passage them as necessary.
4. Expand cells to ~3 confluent T-175 flasks in 20% FBS DMEM (~1 week following isolation)
 - a. Note: **Cells must be cultured and de-primed within 2 weeks of plating on TCPS.** After this point mechanical memory has been permanently attained.
 - b. At this stage cell stocks can be frozen (950 μ L FBS and 50 μ L DMSO) or moved into the “naivete” protocol outlined below.

Excellness Plate preparation

1. Create a 10mg/mL gelatin stock solution in PBS
 - a. Solubilize at 37C with occasional mixing/rocking until no solid gelatin particulates can be seen in the tube.
 - b. Stock solution can be made at larger volumes and aliquoted into 1.5mL microcentrifuge tubes
 - c. Store stocks at 4C and use within 4 months
2. When you are ready to prepare plates:
 - a. Warm 10mg/mL stock tube at RT (or 37C) until viscosity becomes similar to PBS (ensure the solution is clear)
 - b. Dilute the stock solution to 20ug/mL in PBS (use 2uL stock solution per mL)
3. In a 5kPa 10cm Excellness tissue culture plate, add 16 mL diluted stock solution to reach desired coating concentration (~2 μ g gelatin/cm²)
4. Incubate plate(s) at 37C overnight in TC incubator
5. Remove the gelatin coating solution and replace with pre-warmed serum-containing culture media (WITHOUT cells)
6. Incubate plate(s) for at least 3h at 37C prior to seeding cells.

Making cells naïve again

1. Trypsinize the cells like usual. For large vessels like a T175 or 150 mm dish I use 2 mL straight from the stock, after a couple of washes with warm PBS.
2. Resuspend in 20% medium, collect them and count them with Trypan blue (not mandatory)
3. Remove the media you left for 3h on the hydrogel dishes (see above)
4. Add fresh 20% medium, then add enough cells, usually 3 millions per 10 cm dish.

5. Change media every other day. **NOTE: using the aspirator will likely rip cells and suck them away.** Pour the old media into a temporary container, then **SLOWLY** add the fresh medium with the automated pipettor, 13 mL per dish will suffice.
6. Keep this going for two weeks since the seeding date. We might be able to get away with 1 week only, but we haven't performed any experiments to check.
7. For this experiment, on the last day serum starve the cells by changing the media to 1% FBS DMEM. After learning the hard way, it greatly benefits to reinclude HEPES at 25 μ M.

Functionalizing glass (or silica) with fibronectin fragments

Materials:

- Fn fragments (4G, 9*10, Cit-9*) in PBS. They come engineered with a N-terminal Cys
- Sulfo-SMCC crosslinker
- Clean glass substrate
- APTES (3-aminopropyltriethoxysilane)
- Acetone
- Cysteine HCl
- Binding buffer (0.1M sodium phosphate, 0.15M sodium chloride, 10mM EDTA, pH 7.2)
- Wash buffer (0.1M sodium phosphate, 0.15M sodium chloride, 0.05% Tween20, pH 7.2)
- TCEP reducing gel
(<https://www.thermofisher.com/order/catalog/product/77712>)

Functionalizing the glass (inside a chemical hood)

1. Wash well and dry the glass to be coated
2. Make a 2% solution of APTES into acetone (i.e., 1 ml into 49)
3. Immerse (if coverslip) or add enough solution on top of the glass container for 30 seconds
4. Rise with acetone (used APTES+acetone should be collected into its own chemical waste)
5. Allow surfaces to air dry. The dried surfaces can be stored for later use

Reducing dimers in Fn fragments (start along with the next section to try and sync the incubations)

1. You will need 20 µg/ml of fragments and enough volume to coat your glass properly. For example, 2 ml is plenty for something the size of a 6 well-plate well. This calculation will let you know how much mass, thus the volume of fragments stock you will need. There is a small sample loss in this procedure, so draw 25% extra to be safe.

2. Add a volume of TCEP reducing gel slurry equal to one to two times the volume of sample to a microcentrifuge (1.5 mL) tube. For example, use 25-50 μ L of mixed slurry for a 25 μ L protein/peptide sample. You can use a blue spatula if pipetting it is too difficult.
3. Centrifuge the tube at $\sim 1000 \times g$ for 1 minute. Remove and discard the supernatant. If desired, the gel may be washed several times with **binding buffer** before adding sample to the tube. For example, add buffer, vortex briefly to resuspend the gel, briefly centrifuge the tube and remove the supernatant.
4. Add the fragment solution to the washed gel. Vortex the tube and incubate the solution for 1 h at room temperature. It may be helpful to place the tube on a rotating wheel or rocker platform to keep the gel in suspension or flick/flip it by hand at regular intervals.
5. Centrifuge the tube at the same speed for 1 minute. Recover the supernatant containing the reduced protein/peptide.

Maleimide activation of the modified surface

1. Weigh 2 mg of Sufo-SMCC for each 1 mL of **binding buffer** you will need to properly cover the glass. This solution must be made fresh and used right away to avoid hydrolysis. Dissolve the dry mass of Sulfo-SMCC into pure water with 10mM EDTA at pH 7.2 (solubility of at least 12 mg per ml), vortex then dilute into **binding buffer** for the final 2 mg/ml concentration.
2. Coat silylated surface with the crosslinker solution.
3. Incubate for 1h at room temperature.
4. Rinse the modified surface with **binding buffer**. If you dry and store desiccated at 4 C they can last for a week and be ready to go. I personally haven't tried it.

Crosslink fragments to activated surface

1. Cover the maleimide-activated glass with the fragment solution.
2. Incubate for at least 2 hours at room temperature gently shaking. Alternatively, incubate at 4 C overnight.
3. Wash with **wash buffer** three times
4. Prepare a cysteine solution at 10 μ g/ml right before use, with a total volume of **binding buffer** similar to the fragment solution you used. Incubate gently shaking for 1h at room temperature.
5. Wash with **wash buffer** three times

6. Block with 1% BSA for 1h at room temperature, gently shaking. (Here BSA is just what I use in my ELISA tests, I believe it is best to use a truly inert protein or control that you have worked with before).
7. Wash with **wash buffer** three times

CHAPTER 5

REFERENCES

1. Hogan, J., Smith, P., Heath, D. & Harris, P. The thickness of the alveolar capillary wall in the human lung at high and low altitude. *Br. J. Dis. Chest* **80**, 13–18 (1986).
2. Raghu, G. *et al.* An Official ATS/ERS/JRS/ALAT Statement: Idiopathic Pulmonary Fibrosis: Evidence-based Guidelines for Diagnosis and Management. *Am. J. Respir. Crit. Care Med.* **183**, 788–824 (2011).
3. Swigris, J. & Brown, K. K. *Idiopathic Pulmonary Fibrosis*. (Elsevier, 2018).
4. King Jr, T. E., Pardo, A. & Selman, M. Idiopathic pulmonary fibrosis. *The Lancet* **378**, 1949–1961 (2011).
5. Kreuter, M. *et al.* Pharmacological Treatment of Idiopathic Pulmonary Fibrosis: Current Approaches, Unsolved Issues, and Future Perspectives, Pharmacological Treatment of Idiopathic Pulmonary Fibrosis: Current Approaches, Unsolved Issues, and Future Perspectives. *BioMed Res. Int. BioMed Res. Int.* **2015**, **2015**, e329481 (2015).
6. Meltzer, E. B. & Noble, P. W. Idiopathic pulmonary fibrosis. *Orphanet J. Rare Dis.* **3**, 8 (2008).
7. Raghu, G. *et al.* Diagnosis of Idiopathic Pulmonary Fibrosis. An Official ATS/ERS/JRS/ALAT Clinical Practice Guideline. *Am. J. Respir. Crit. Care Med.* **198**, e44–e68 (2018).
8. Frantz, C., Stewart, K. M. & Weaver, V. M. The extracellular matrix at a glance. *J Cell Sci* **123**, 4195–4200 (2010).
9. George, E. L., Georges-Labouesse, E. N., Patel-King, R. S., Rayburn, H. & Hynes, R. O. Defects in mesoderm, neural tube and vascular development in mouse embryos lacking fibronectin. *Dev. Camb. Engl.* **119**, 1079–1091 (1993).
10. Li, S., Edgar, D., Fässler, R., Wadsworth, W. & Yurchenco, P. D. The role of laminin in embryonic cell polarization and tissue organization. *Dev. Cell* **4**, 613–624 (2003).
11. Bonnans, C., Chou, J. & Werb, Z. Remodelling the extracellular matrix in development and disease. *Nat. Rev. Mol. Cell Biol.* **15**, 786–801 (2014).

12. Bissell, M. J., Hall, H. G. & Parry, G. How does the extracellular matrix direct gene expression? *J. Theor. Biol.* **99**, 31–68 (1982).
13. van Helvert, S., Storm, C. & Friedl, P. Mechanoreciprocity in cell migration. *Nat. Cell Biol.* **20**, 8–20 (2018).
14. Oberhauser, A. F., Badilla-Fernandez, C., Carrion-Vazquez, M. & Fernandez, J. M. The Mechanical Hierarchies of Fibronectin Observed with Single-molecule AFM. *J. Mol. Biol.* **319**, 433–447 (2002).
15. Krammer, A., Lu, H., Isralewitz, B., Schulten, K. & Vogel, V. Forced unfolding of the fibronectin type III module reveals a tensile molecular recognition switch. *Proc. Natl. Acad. Sci.* **96**, 1351–1356 (1999).
16. Lemmon, C. A., Ohashi, T. & Erickson, H. P. Probing the Folded State of Fibronectin Type III Domains in Stretched Fibrils by Measuring Buried Cysteine Accessibility. *J. Biol. Chem.* **286**, 26375–26382 (2011).
17. D’Aur aux, B. & Toledano, M. B. ROS as signalling molecules: mechanisms that generate specificity in ROS homeostasis. *Nat. Rev. Mol. Cell Biol.* **8**, 813–824 (2007).
18. Furukawa, S. *et al.* Increased oxidative stress in obesity and its impact on metabolic syndrome. *J. Clin. Invest.* **114**, 1752–1761 (2017).
19. Rees, M. D., Kennett, E. C., Whitelock, J. M. & Davies, M. J. Oxidative damage to extracellular matrix and its role in human pathologies. *Free Radic. Biol. Med.* **44**, 1973–2001 (2008).
20. Lai, C.-H. *et al.* Protein oxidation and degradation caused by particulate matter. *Sci. Rep.* **6**, 33727 (2016).
21. Cantin, A. M. & B egin, R. Glutathione and inflammatory disorders of the lung. *Lung* **169**, 123–138 (1991).
22. van der Reest, J., Lilla, S., Zheng, L., Zanivan, S. & Gottlieb, E. Proteome-wide analysis of cysteine oxidation reveals metabolic sensitivity to redox stress. *Nat. Commun.* **9**, 1581 (2018).
23. Dalle-Donne, I., Rossi, R., Colombo, G., Giustarini, D. & Milzani, A. Protein S-glutathionylation: a regulatory device from bacteria to humans. *Trends Biochem. Sci.* **34**, 85–96 (2009).

24. Anathy, V. *et al.* Reducing protein oxidation reverses lung fibrosis. *Nat. Med.* **24**, 1128–1135 (2018).
25. Leeming, D. J. *et al.* Post-translational modifications of the extracellular matrix are key events in cancer progression: Opportunities for biochemical marker development. *Biomarkers* **16**, 193–205 (2011).
26. Brown, A. C., Fiore, V. F., Sulchek, T. A. & Barker, T. H. Physical and chemical microenvironmental cues orthogonally control the degree and duration of fibrosis-associated epithelial-to-mesenchymal transitions. *J. Pathol.* **229**, 25–35 (2013).
27. Fiore, V. F. *et al.* $\alpha\beta$ 3 Integrin drives fibroblast contraction and strain stiffening of soft provisional matrix during progressive fibrosis. *JCI Insight* **3**,.
28. Bachman, H., Nicosia, J., Dysart, M. & Barker, T. H. Utilizing Fibronectin Integrin-Binding Specificity to Control Cellular Responses. *Adv. Wound Care* **4**, 501–511 (2015).
29. Gao, M. *et al.* Structure and functional significance of mechanically unfolded fibronectin type III intermediates. *Proc. Natl. Acad. Sci.* **100**, 14784–14789 (2003).
30. Main, A. L., Harvey, T. S., Baron, M., Boyd, J. & Campbell, I. D. The three-dimensional structure of the tenth type III module of fibronectin: An insight into RGD-mediated interactions. *Cell* **71**, 671–678 (1992).
31. Krammer, A., Craig, D., Thomas, W. E., Schulten, K. & Vogel, V. A structural model for force regulated integrin binding to fibronectin's RGD-synergy site. *Matrix Biol.* **21**, 139–147 (2002).
32. Dufour, S. *et al.* Attachment, spreading and locomotion of avian neural crest cells are mediated by multiple adhesion sites on fibronectin molecules. *EMBO J.* **7**, 2661–2671 (1988).
33. Pierschbacher, M. D. & Ruoslahti, E. Cell attachment activity of fibronectin can be duplicated by small synthetic fragments of the molecule. *Nature* **309**, 30–33 (1984).
34. Mardon, H. J. & Grant, K. E. The role of the ninth and tenth type III domains of human fibronectin in cell adhesion. *FEBS Lett.* **340**, 197–201 (1994).
35. Stabenfeldt, S. E., Brown, A. C. & Barker, T. H. Engineering ECM Complexity into Biomaterials for Directing Cell Fate. in *Biomaterials as Stem Cell Niche* (ed. Roy, K.) 1–18 (Springer Berlin Heidelberg, 2010). doi:10.1007/8415_2010_1.

36. Brown, A. C., Rowe, J. A. & Barker, T. H. Guiding Epithelial Cell Phenotypes with Engineered Integrin-Specific Recombinant Fibronectin Fragments. *Tissue Eng. Part A* **17**, 139–150 (2010).
37. Georges-Labouesse, E. N., George, E. L., Rayburn, H. & Hynes, R. O. Mesodermal development in mouse embryos mutant for fibronectin. *Dev. Dyn.* **207**, 145–156 (1996).
38. Astrof, S., Crowley, D. & Hynes, R. O. Multiple cardiovascular defects caused by the absence of alternatively spliced segments of fibronectin. *Dev. Biol.* **311**, 11–24 (2007).
39. Fukuda, T. *et al.* Mice Lacking the EDB Segment of Fibronectin Develop Normally but Exhibit Reduced Cell Growth and Fibronectin Matrix Assembly in Vitro. *Cancer Res.* **62**, 5603–5610 (2002).
40. Tan, M. H. *et al.* Deletion of the alternatively spliced fibronectin EIIIA domain in mice reduces atherosclerosis. *Blood* **104**, 11–18 (2004).
41. Magnuson, V. L. *et al.* The alternative splicing of fibronectin pre-mRNA is altered during aging and in response to growth factors. *J. Biol. Chem.* **266**, 14654–14662 (1991).
42. Pagani, F. *et al.* Tissue-specific splicing pattern of fibronectin messenger RNA precursor during development and aging in rat. *J. Cell Biol.* **113**, 1223–1229 (1991).
43. Schiefner, A., Gebauer, M. & Skerra, A. Extra-domain B in Oncofetal Fibronectin Structurally Promotes Fibrillar Head-to-tail Dimerization of Extracellular Matrix Protein. *J. Biol. Chem.* **287**, 17578–17588 (2012).
44. Chauhan, A. K. *et al.* Prothrombotic Effects of Fibronectin Isoforms Containing the EDA Domain. *Arterioscler. Thromb. Vasc. Biol.* **28**, 296–301 (2008).
45. Fontana, L. *et al.* Fibronectin is required for integrin $\alpha\text{v}\beta\text{6}$ -mediated activation of latent TGF- β complexes containing LTBP-1. *FASEB J.* **19**, 1798–1808 (2005).
46. Muro, A. F. *et al.* An Essential Role for Fibronectin Extra Type III Domain A in Pulmonary Fibrosis. *Am. J. Respir. Crit. Care Med.* **177**, 638–645 (2008).
47. White Eric S. & Muro Andrés F. Fibronectin splice variants: Understanding their multiple roles in health and disease using engineered mouse models. *IUBMB Life* **63**, 538–546 (2011).

48. Pankov, R. & Yamada, K. M. Fibronectin at a glance. *J. Cell Sci.* **115**, 3861–3863 (2002).
49. Roy, D. C. & Hocking, D. C. Recombinant Fibronectin Matrix Mimetics Specify Integrin Adhesion and Extracellular Matrix Assembly. *Tissue Eng. Part A* **19**, 558–570 (2012).
50. Zhang, Z. *et al.* The alpha v beta 1 integrin functions as a fibronectin receptor but does not support fibronectin matrix assembly and cell migration on fibronectin. *J. Cell Biol.* **122**, 235–242 (1993).
51. Grant, R. P., Spitzfaden, C., Altroff, H., Campbell, I. D. & Mardon, H. J. Structural requirements for biological activity of the ninth and tenth FIII domains of human fibronectin. *J. Biol. Chem.* **272**, 6159–6166 (1997).
52. Cao, L. *et al.* Detection of an Integrin-Binding Mechanoswitch within Fibronectin during Tissue Formation and Fibrosis. *ACS Nano* **11**, 7110–7117 (2017).
53. Tan, J. L. *et al.* Cells lying on a bed of microneedles: An approach to isolate mechanical force. *Proc. Natl. Acad. Sci.* **100**, 1484–1489 (2003).
54. Bharadwaj, M. *et al.* α V-class integrins exert dual roles on α 5 β 1 integrins to strengthen adhesion to fibronectin. *Nat. Commun.* **8**, ncomms14348 (2017).
55. Arias-Salgado, E. G. *et al.* Src Kinase Activation by Direct Interaction with the Integrin β Cytoplasmic Domain. *Proc. Natl. Acad. Sci. U. S. A.* **100**, 13298–13302 (2003).
56. Zeller, K. S. Integrin Signaling in Cell Adhesion and Mechanotransduction : Regulation of PI3K, AKT, and ROS. (2012).
57. Du, T. *et al.* Maternal embryonic leucine zipper kinase enhances gastric cancer progression via the FAK/Paxillin pathway. *Mol. Cancer* **13**, 100 (2014).
58. Franco-Barraza, J. *et al.* Matrix-regulated integrin α v β 5 maintains α 5 β 1-dependent desmoplastic traits prognostic of neoplastic recurrence. *eLife* **6**, (2017).
59. Shinde, A. V. *et al.* Identification of the Peptide Sequences within the EIIIA (EDA) Segment of Fibronectin That Mediate Integrin α 9 β 1-dependent Cellular Activities. *J. Biol. Chem.* **283**, 2858–2870 (2008).

60. Wong, S., Guo, W.-H. & Wang, Y.-L. Fibroblasts probe substrate rigidity with filopodia extensions before occupying an area. *Proc. Natl. Acad. Sci.* **111**, 17176–17181 (2014).
61. Nakayama, Y. *et al.* Blockade of interaction of $\alpha 9$ integrin with its ligands hinders the formation of granulation in cutaneous wound healing. *Lab. Invest.* **90**, 881–894 (2010).
62. Schnittert, J., Bansal, R., Storm, G. & Prakash, J. Integrins in wound healing, fibrosis and tumor stroma: High potential targets for therapeutics and drug delivery. *Adv. Drug Deliv. Rev.* (2018) doi:10.1016/j.addr.2018.01.020.
63. Palmer, E. L., Rüegg, C., Ferrando, R., Pytela, R. & Sheppard, D. Sequence and tissue distribution of the integrin alpha 9 subunit, a novel partner of beta 1 that is widely distributed in epithelia and muscle. *J. Cell Biol.* **123**, 1289–1297 (1993).
64. Shinde, A. V. *et al.* The $\alpha 4\beta 1$ integrin and the EDA domain of fibronectin regulate a profibrotic phenotype in dermal fibroblasts. *Matrix Biol.* **41**, 26–35 (2015).
65. Sun, K.-H., Chang, Y., Reed, N. I. & Sheppard, D. α -Smooth muscle actin is an inconsistent marker of fibroblasts responsible for force-dependent TGF β activation or collagen production across multiple models of organ fibrosis. *Am. J. Physiol. - Lung Cell. Mol. Physiol.* **310**, L824–L836 (2016).
66. Moulin Véronique *et al.* Fetal and adult human skin fibroblasts display intrinsic differences in contractile capacity. *J. Cell. Physiol.* **188**, 211–222 (2001).
67. Louka, M. L. & Ramzy, M. M. Involvement of fibroblast-specific protein 1 (S100A4) and matrix metalloproteinase-13 (MMP-13) in CCl₄-induced reversible liver fibrosis. *Gene* **579**, 29–33 (2016).
68. Österreicher, C. H. *et al.* Fibroblast-specific protein 1 identifies an inflammatory subpopulation of macrophages in the liver. *Proc. Natl. Acad. Sci. U. S. A.* **108**, 308–313 (2011).
69. Zhang, R. *et al.* FSP1-positive fibroblasts are adipogenic niche and regulate adipose homeostasis. *PLOS Biol.* **16**, e2001493 (2018).
70. Li, R. *et al.* Pdgfra marks a cellular lineage with distinct contributions to myofibroblasts in lung maturation and injury response. *eLife* **7**, e36865 (2018).
71. Hagood, J. S. *et al.* Loss of Fibroblast Thy-1 Expression Correlates with Lung Fibrogenesis. *Am. J. Pathol.* **167**, 365–379 (2005).

72. Huang, X. *et al.* Matrix Stiffness–Induced Myofibroblast Differentiation Is Mediated by Intrinsic Mechanotransduction. *Am. J. Respir. Cell Mol. Biol.* **47**, 340–348 (2012).
73. Chen, H. *et al.* Mechanosensing by the α_6 -integrin confers an invasive fibroblast phenotype and mediates lung fibrosis. *Nat. Commun.* **7**, ncomms12564 (2016).
74. Roca-Cusachs, P., Gauthier, N. C., del Rio, A. & Sheetz, M. P. Clustering of $\alpha_5\beta_1$ integrins determines adhesion strength whereas $\alpha\nu\beta_3$ and talin enable mechanotransduction. *Proc. Natl. Acad. Sci. U. S. A.* **106**, 16245–16250 (2009).
75. Zeltz, C. & Gullberg, D. The integrin–collagen connection – a glue for tissue repair? *J Cell Sci* **129**, 653–664 (2016).
76. Knight, C. G. *et al.* The Collagen-binding A-domains of Integrins $\alpha_1\beta_1$ and $\alpha_2\beta_1$ Recognize the Same Specific Amino Acid Sequence, GFOGER, in Native (Triple-helical) Collagens. *J. Biol. Chem.* **275**, 35–40 (2000).
77. Zhang, W.-M. *et al.* $\alpha_1\beta_1$ Integrin Recognizes the GFOGER Sequence in Interstitial Collagens. *J. Biol. Chem.* **278**, 7270–7277 (2003).
78. Hamaia, S. W. *et al.* Mapping of Potent and Specific Binding Motifs, GLOGEN and GVOGEA, for Integrin $\alpha_1\beta_1$ Using Collagen Toolkits II and III. *J. Biol. Chem.* **287**, 26019–26028 (2012).
79. Langholz, O. *et al.* Collagen and collagenase gene expression in three-dimensional collagen lattices are differentially regulated by alpha 1 beta 1 and alpha 2 beta 1 integrins. *J. Cell Biol.* **131**, 1903–1915 (1995).
80. Merkel, J. R., DiPaolo, B. R., Hallock, G. G. & Rice, D. C. Type I and Type III Collagen Content of Healing Wounds in Fetal and Adult Rats. *Proc. Soc. Exp. Biol. Med.* **187**, 493–497 (1988).
81. Cuttle, L. *et al.* Collagen in the scarless fetal skin wound: Detection with Picrosirius-polarization. *Wound Repair Regen.* **13**, 198–204 (2005).
82. Ravanti, L., Heino, J., López-Otín, C. & Kähäri, V.-M. Induction of Collagenase-3 (MMP-13) Expression in Human Skin Fibroblasts by Three-dimensional Collagen Is Mediated by p38 Mitogen-activated Protein Kinase. *J. Biol. Chem.* **274**, 2446–2455 (1999).

83. Xu, J. & Clark, R. A. F. A Three-dimensional Collagen Lattice Induces Protein Kinase C- ζ Activity: Role in $\alpha 2$ Integrin and Collagenase mRNA Expression. *J. Cell Biol.* **136**, 473–483 (1997).
84. Ivaska, J. *et al.* Integrin $\alpha 2\beta 1$ Mediates Isoform-Specific Activation of p38 and Upregulation of Collagen Gene Transcription by a Mechanism Involving the $\alpha 2$ Cytoplasmic Tail. *J. Cell Biol.* **147**, 401–416 (1999).
85. Xia, H. *et al.* Low $\alpha 2\beta 1$ Integrin Function Enhances the Proliferation of Fibroblasts from Patients with Idiopathic Pulmonary Fibrosis by Activation of the β -Catenin Pathway. *Am. J. Pathol.* **181**, 222–233 (2012).
86. Schulz, J.-N. *et al.* Reduced granulation tissue and wound strength in the absence of $\alpha 11\beta 1$ integrin. *J. Invest. Dermatol.* **135**, 1435–1444 (2015).
87. Lu, L. *et al.* Role of SMAD and Non-SMAD Signals in the Development of Th17 and Regulatory T Cells. *J. Immunol.* **184**, 4295–4306 (2010).
88. Gullberg, D., Kletsas, D. & Pihlajaniemi, T. Editorial: Wound healing and fibrosis—two sides of the same coin. *Cell Tissue Res.* **365**, 449–451 (2016).
89. Romaine, A. *et al.* Overexpression of integrin $\alpha 11$ induces cardiac fibrosis in mice. *Acta Physiol.* **222**, e12932 (2018).
90. Pelham, R. J. & Wang, Y. Cell locomotion and focal adhesions are regulated by substrate flexibility. *Proc. Natl. Acad. Sci.* **94**, 13661–13665 (1997).
91. Paszek, M. J. & Weaver, V. M. The Tension Mounts: Mechanics Meets Morphogenesis and Malignancy. *J. Mammary Gland Biol. Neoplasia* **9**, 325–342 (2004).
92. Solon, J., Levental, I., Sengupta, K., Georges, P. C. & Janmey, P. A. Fibroblast Adaptation and Stiffness Matching to Soft Elastic Substrates. *Biophys. J.* **93**, 4453–4461 (2007).
93. Cao, L. *et al.* Phage-based molecular probes that discriminate force-induced structural states of fibronectin in vivo. *Proc. Natl. Acad. Sci.* **109**, 7251–7256 (2012).
94. Kuhn, C. & McDonald, J. A. The roles of the myofibroblast in idiopathic pulmonary fibrosis. Ultrastructural and immunohistochemical features of sites of active extracellular matrix synthesis. *Am. J. Pathol.* **138**, 1257–1265 (1991).

95. Tomasek, J. J., Gabbiani, G., Hinz, B., Chaponnier, C. & Brown, R. A. Myofibroblasts and mechano-regulation of connective tissue remodelling. *Nat. Rev. Mol. Cell Biol.* **3**, 349–363 (2002).
96. Serini, G. *et al.* The Fibronectin Domain ED-A Is Crucial for Myofibroblastic Phenotype Induction by Transforming Growth Factor- β 1. *J. Cell Biol.* **142**, 873–881 (1998).
97. Kohan, M., Muro, A. F., White, E. S. & Berkman, N. EDA-containing cellular fibronectin induces fibroblast differentiation through binding to α 4 β 7 integrin receptor and MAPK/Erk 1/2-dependent signaling. *FASEB J.* **24**, 4503–4512 (2010).
98. Sottile, J. & Hocking, D. C. Fibronectin Polymerization Regulates the Composition and Stability of Extracellular Matrix Fibrils and Cell-Matrix Adhesions. *Mol. Biol. Cell* **13**, 3546–3559 (2002).
99. Mao, Y. & Schwarzbauer, J. E. Fibronectin fibrillogenesis, a cell-mediated matrix assembly process. *Matrix Biol.* **24**, 389–399 (2005).
100. Booth, A. J. *et al.* Acellular normal and fibrotic human lung matrices as a culture system for in vitro investigation. *Am. J. Respir. Crit. Care Med.* **186**, 866–876 (2012).
101. Parker, M. W. *et al.* Fibrotic extracellular matrix activates a profibrotic positive feedback loop. *J. Clin. Invest.* **124**, (2014).
102. Thannickal, V. J. *et al.* Matrix Biology of Idiopathic Pulmonary Fibrosis: A Workshop Report of the National Heart, Lung, and Blood Institute. *Am. J. Pathol.* **184**, 1643–1651 (2014).
103. Gee, E. P. S., Ingber, D. E. & Stultz, C. M. Fibronectin Unfolding Revisited: Modeling Cell Traction-Mediated Unfolding of the Tenth Type-III Repeat. *PLOS ONE* **3**, e2373 (2008).
104. Li, L., Huang, H. H.-L., Badilla, C. L. & Fernandez, J. M. Mechanical Unfolding Intermediates Observed by Single-molecule Force Spectroscopy in a Fibronectin Type III Module. *J. Mol. Biol.* **345**, 817–826 (2005).
105. Craig, D., Krammer, A., Schulten, K. & Vogel, V. Comparison of the early stages of forced unfolding for fibronectin type III modules. *Proc. Natl. Acad. Sci.* **98**, 5590–5595 (2001).

106. Martino, M. M. *et al.* Controlling integrin specificity and stem cell differentiation in 2D and 3D environments through regulation of fibronectin domain stability. *Biomaterials* **30**, 1089–1097 (2009).
107. Ruoslahti, E. Rgd and Other Recognition Sequences for Integrins. *Annu. Rev. Cell Dev. Biol.* **12**, 697–715 (1996).
108. der Walle, C. F. van, Altroff, H. & J.Mardon, H. Novel mutant human fibronectin FIII9–10 domain pair with increased conformational stability and biological activity. *Protein Eng.* **15**, 1021–1024 (2002).
109. Shroff, K., Pearce, T. R. & Kokkoli, E. Enhanced Integrin Mediated Signaling and Cell Cycle Progression on Fibronectin Mimetic Peptide Amphiphile Monolayers. *Langmuir* **28**, 1858–1865 (2012).
110. Altroff, H., Choulier, L. & Mardon, H. J. Synergistic Activity of the Ninth and Tenth FIII Domains of Human Fibronectin Depends upon Structural Stability *. *J. Biol. Chem.* **278**, 491–497 (2003).
111. Altroff, H. *et al.* Interdomain Tilt Angle Determines Integrin-dependent Function of the Ninth and Tenth FIII Domains of Human Fibronectin *. *J. Biol. Chem.* **279**, 55995–56003 (2004).
112. Cao, L. *et al.* Detection of an Integrin-Binding Mechanoswitch within Fibronectin during Tissue Formation and Fibrosis. *ACS Nano* **11**, 7110–7117 (2017).
113. Nilson, B. H., Solomon, A., Björck, L. & Akerström, B. Protein L from *Peptostreptococcus magnus* binds to the kappa light chain variable domain. *J. Biol. Chem.* **267**, 2234–2239 (1992).
114. Lock, J. G. *et al.* Reticular adhesions are a distinct class of cell-matrix adhesions that mediate attachment during mitosis. *Nat. Cell Biol.* **20**, 1290–1302 (2018).
115. B. Moore, B. *et al.* Animal Models of Fibrotic Lung Disease. *Am. J. Respir. Cell Mol. Biol.* **49**, 167–179 (2013).
116. Desogere, P. *et al.* Type I collagen-targeted PET probe for pulmonary fibrosis detection and staging in preclinical models. *Sci. Transl. Med.* **9**, (2017).
117. Shea, B. S. *et al.* Prolonged Exposure to Sphingosine 1-Phosphate Receptor-1 Agonists Exacerbates Vascular Leak, Fibrosis, and Mortality after Lung Injury. *Am. J. Respir. Cell Mol. Biol.* **43**, 662–673 (2010).

118. Reyfman, P. A. *et al.* Single-Cell Transcriptomic Analysis of Human Lung Provides Insights into the Pathobiology of Pulmonary Fibrosis. *Am. J. Respir. Crit. Care Med.* **199**, 1517–1536 (2019).
119. Schiller, H. B. *et al.* β 1- and α v-class integrins cooperate to regulate myosin II during rigidity sensing of fibronectin-based microenvironments. *Nat. Cell Biol.* **15**, 625–636 (2013).
120. Massia, S. P. & Hubbell, J. A. An RGD spacing of 440 nm is sufficient for integrin alpha V beta 3-mediated fibroblast spreading and 140 nm for focal contact and stress fiber formation. *J. Cell Biol.* **114**, 1089–1100 (1991).
121. Strohmeyer, N., Bharadwaj, M., Costell, M., Fässler, R. & Müller, D. J. Fibronectin-bound α 5 β 1 integrins sense load and signal to reinforce adhesion in less than a second. *Nat. Mater.* **16**, 1262–1270 (2017).
122. Kong, F., García, A. J., Mould, A. P., Humphries, M. J. & Zhu, C. Demonstration of catch bonds between an integrin and its ligand. *J. Cell Biol.* **185**, 1275–1284 (2009).
123. Benito-Jardón, M. *et al.* The fibronectin synergy site re-enforces cell adhesion and mediates a crosstalk between integrin classes. *eLife* **6**, (2017).
124. Weston, C. R. & Davis, R. J. The JNK signal transduction pathway. *Curr. Opin. Cell Biol.* **19**, 142–149 (2007).
125. Ventura, J.-J. *et al.* Chemical Genetic Analysis of the Time Course of Signal Transduction by JNK. *Mol. Cell* **21**, 701–710 (2006).
126. Grynberg, K., Ma, F. Y. & Nikolic-Paterson, D. J. The JNK Signaling Pathway in Renal Fibrosis. *Front. Physiol.* **8**, (2017).
127. Ma, Q. & Devarajan, P. Induction of proapoptotic Daxx following ischemic acute kidney injury. *Kidney Int.* **74**, 310–318 (2008).
128. Velden, J. L. J. van der, Alcorn, J. F., Guala, A. S., Badura, E. C. H. L. & Janssen-Heininger, Y. M. W. c-Jun N-Terminal Kinase 1 Promotes Transforming Growth Factor- β 1-Induced Epithelial-to-Mesenchymal Transition via Control of Linker Phosphorylation and Transcriptional Activity of Smad3. *Am. J. Respir. Cell Mol. Biol.* **44**, 571–581 (2011).
129. Kim, S. J. *et al.* Autoinduction of transforming growth factor beta 1 is mediated by the AP-1 complex. *Mol. Cell. Biol.* **10**, 1492–1497 (1990).

130. Naito, T. *et al.* Angiotensin II induces thrombospondin-1 production in human mesangial cells via p38 MAPK and JNK: a mechanism for activation of latent TGF- β 1. *Am. J. Physiol.-Ren. Physiol.* **286**, F278–F287 (2004).
131. Lee, K.-Y. *et al.* NF- κ B and Activator Protein 1 Response Elements and the Role of Histone Modifications in IL-1 β -Induced TGF- β 1 Gene Transcription. *J. Immunol.* **176**, 603–615 (2006).
132. Rui, H., Wang, Y., Cheng, H. & Chen, Y. JNK-dependent AP-1 activation is required for aristolochic acid-induced TGF- β 1 synthesis in human renal proximal epithelial cells. *Am. J. Physiol.-Ren. Physiol.* **302**, F1569–F1575 (2012).
133. Yamaguchi, K. *et al.* Identification of a Member of the MAPKKK Family as a Potential Mediator of TGF- β Signal Transduction. *Science* **270**, 2008–2011 (1995).
134. Sun, Y. B. Y., Qu, X., Li, X., Nikolic-Paterson, D. J. & Li, J. Endothelial Dysfunction Exacerbates Renal Interstitial Fibrosis through Enhancing Fibroblast Smad3 Linker Phosphorylation in the Mouse Obstructed Kidney. *PLOS ONE* **8**, e84063 (2013).
135. McKenzie, A. J., Svec, K. V., Williams, T. F. & Howe, A. K. Protein kinase A activity is regulated by actomyosin contractility during cell migration and is required for durotaxis. *Mol. Biol. Cell* **31**, 45–58 (2020).
136. Montminy, M. R. & Bilezikjian, L. M. Binding of a nuclear protein to the cyclic-AMP response element of the somatostatin gene. *Nature* **328**, 175–178 (1987).
137. Hai, T. W., Liu, F., Allegretto, E. A., Karin, M. & Green, M. R. A family of immunologically related transcription factors that includes multiple forms of ATF and AP-1. *Genes Dev.* **2**, 1216–1226 (1988).
138. Foulkes, N. S., Borrelli, E. & Sassone-Corsi, P. CREM gene: Use of alternative DNA-binding domains generates multiple antagonists of cAMP-induced transcription. *Cell* **64**, 739–749 (1991).
139. Tonucci, F. M. *et al.* Identification of a CIP4 PKA phosphorylation site involved in the regulation of cancer cell invasiveness and metastasis. *Cancer Lett.* **461**, 65–77 (2019).
140. Liu, Z. *et al.* MAPK-Mediated YAP Activation Controls Mechanical-Tension-Induced Pulmonary Alveolar Regeneration. *Cell Rep.* **16**, 1810–1819 (2016).

141. Freund, A., Patil, C. K. & Campisi, J. p38MAPK is a novel DNA damage response-independent regulator of the senescence-associated secretory phenotype. *EMBO J.* **30**, 1536–1548 (2011).
142. Alspach, E. *et al.* p38MAPK plays a crucial role in stromal mediated tumorigenesis. *Cancer Discov.* **4**, 716–729 (2014).
143. Brichkina, A. *et al.* p38MAPK builds a hyaluronan cancer niche to drive lung tumorigenesis. *Genes Dev.* **30**, 2623–2636 (2016).
144. Mandal, K. *et al.* Soft Hyaluronic Gels Promote Cell Spreading, Stress Fibers, Focal Adhesion, and Membrane Tension by Phosphoinositide Signaling, Not Traction Force. *ACS Nano* **13**, 203–214 (2019).
145. Hui, E., Moretti, L., Barker, T. H. & Caliri, S. R. The combined influence of viscoelasticity and adhesive cues on fibroblast spreading and focal adhesion formation. *bioRxiv* 2021.02.17.430924 (2021) doi:10.1101/2021.02.17.430924.
146. Kulkarni, A. A. *et al.* PPAR- γ Ligands Repress TGF β -Induced Myofibroblast Differentiation by Targeting the PI3K/Akt Pathway: Implications for Therapy of Fibrosis. *PLOS ONE* **6**, e15909 (2011).
147. Li, Y. *et al.* Inhibition of Integrin-Linked Kinase Attenuates Renal Interstitial Fibrosis. *J. Am. Soc. Nephrol.* **20**, 1907–1918 (2009).
148. Kavvadas, P. *et al.* Integrin-linked kinase (ILK) in pulmonary fibrosis. *Virchows Arch.* **457**, 563–575 (2010).
149. Schulz, J.-N. *et al.* COMP-assisted collagen secretion – a novel intracellular function required for fibrosis. *J. Cell Sci.* **129**, 706–716 (2016).
150. Wu, Y. & Xu, Y. Integrated bioinformatics analysis of expression and gene regulation network of COL12A1 in colorectal cancer. *Cancer Med.* **9**, 4743–4755 (2020).
151. Li, Y., Liu, Y., Shi, F., Cheng, L. & She, J. Knockdown of Rap1b Enhances Apoptosis and Autophagy in Gastric Cancer Cells via the PI3K/Akt/mTOR Pathway. *Oncol. Res.* **24**, 287–293 (2016).
152. Chen, X.-W. *et al.* A Ral GAP complex links PI 3-kinase/Akt signaling to RalA activation in insulin action. *Mol. Biol. Cell* **22**, 141–152 (2011).

153. Stefanelli, V. L. *et al.* Citrullination of fibronectin alters integrin clustering and focal adhesion stability promoting stromal cell invasion. *Matrix Biol.* **82**, 86–104 (2019).
154. Ojo, A. S., Balogun, S. A., Williams, O. T. & Ojo, O. S. Pulmonary Fibrosis in COVID-19 Survivors: Predictive Factors and Risk Reduction Strategies. *Pulm. Med.* **2020**, e6175964 (2020).
155. Hayashi, H. *et al.* The MAD-Related Protein Smad7 Associates with the TGF β Receptor and Functions as an Antagonist of TGF β Signaling. *Cell* **89**, 1165–1173 (1997).
156. García, A. J., Vega, M. D. & Boettiger, D. Modulation of Cell Proliferation and Differentiation through Substrate-dependent Changes in Fibronectin Conformation. *Mol. Biol. Cell* **10**, 785–798 (1999).
157. Wang, Z. *et al.* BART: a transcription factor prediction tool with query gene sets or epigenomic profiles. *Bioinformatics* **34**, 2867–2869 (2018).
158. Ma, W. *et al.* BARTweb: a web server for transcriptional regulator association analysis. *NAR Genomics Bioinforma.* **3**, (2021).
159. Farhang-Fallah, J. *et al.* The Pleckstrin Homology (PH) Domain-Interacting Protein Couples the Insulin Receptor Substrate 1 PH Domain to Insulin Signaling Pathways Leading to Mitogenesis and GLUT4 Translocation. *Mol. Cell. Biol.* **22**, 7325–7336 (2002).
160. Zha, L. *et al.* Genome-wide analysis of HMGA2 transcription factor binding sites by ChIP on chip in gastric carcinoma cells. *Mol. Cell. Biochem.* **364**, 243–251 (2012).
161. Translating MicroRNAs to the Clinic - 1st Edition.
<https://www.elsevier.com/books/T/A/9780128005538>.
162. Liefke, R., Karwacki-Neisius, V. & Shi, Y. EPOP Interacts with Elongin BC and USP7 to Modulate the Chromatin Landscape. *Mol. Cell* **64**, 659–672 (2016).
163. Biddlestone, J., Batie, M., Bandarra, D., Munoz, I. & Rocha, S. SINHCAF/FAM60A and SIN3A specifically repress HIF-2 α expression. *Biochem. J.* **475**, 2073–2090 (2018).
164. Icardi, L. *et al.* The Sin3a repressor complex is a master regulator of STAT transcriptional activity. *Proc. Natl. Acad. Sci.* **109**, 12058–12063 (2012).

165. Chastney, M. R. *et al.* Topological features of integrin adhesion complexes revealed by multiplexed proximity biotinylation. *J. Cell Biol.* **219**, (2020).
166. Ly, K. T. & Casanova, J. E. Mechanisms of Salmonella entry into host cells. *Cell. Microbiol.* **9**, 2103–2111 (2007).
167. Cossart, P. & Sansonetti, P. J. Bacterial Invasion: The Paradigms of Enteroinvasive Pathogens. *Science* **304**, 242–248 (2004).
168. Peyser, R. *et al.* Defining the Activated Fibroblast Population in Lung Fibrosis Using Single-Cell Sequencing. *Am. J. Respir. Cell Mol. Biol.* **61**, 74–85 (2019).
169. Alegre-Cebollada, J. *et al.* S-Glutathionylation of Cryptic Cysteines Enhances Titin Elasticity by Blocking Protein Folding. *Cell* **156**, 1235–1246 (2014).
170. Yang, Y., Jin, X. & Jiang, C. S-Glutathionylation of Ion Channels: Insights into the Regulation of Channel Functions, Thiol Modification Crosstalk, and Mechanosensing. *Antioxid. Redox Signal.* **20**, 937–951 (2013).
171. Ejim, O. S., Blunn, G. W. & Brown, R. A. Production of artificial-orientated mats and strands from plasma fibronectin: a morphological study. *Biomaterials* **14**, 743–748 (1993).
172. Cao, L. *et al.* Phage-based molecular probes that discriminate force-induced structural states of fibronectin in vivo. *Proc. Natl. Acad. Sci. U. S. A.* **109**, 7251–7256 (2012).
173. Liu, W. *et al.* Fibrin fibers have extraordinary extensibility and elasticity. *Science* **313**, 634 (2006).
174. Alegre-Cebollada, J. *et al.* S-glutathionylation of cryptic cysteines enhances titin elasticity by blocking protein folding. *Cell* **156**, 1235–1246 (2014).
175. Mailloux, R. J. & Willmore, W. G. S-glutathionylation reactions in mitochondrial function and disease. *Front. Cell Dev. Biol.* **2**, (2014).
176. Zhang, J. *et al.* S-Glutathionylation of estrogen receptor α affects dendritic cell function. *J. Biol. Chem.* **293**, 4366–4380 (2018).
177. Yang, Y., Jin, X. & Jiang, C. S-glutathionylation of ion channels: Insights into the regulation of channel functions, thiol modification crosstalk, and mechanosensing. *Antioxidants and Redox Signaling* vol. 20 937–951 (2014).

178. Xiong, Y., Uys, J. D., Tew, K. D. & Townsend, D. M. S-Glutathionylation: From molecular mechanisms to health outcomes. *Antioxid. Redox Signal.* **15**, 233–270 (2011).
179. Chittiboyina, S. *et al.* Gradient-on-a-Chip with Reactive Oxygen Species Reveals Thresholds in the Nucleus Response of Cancer Cells Depending on the Matrix Environment. *ACS Biomater. Sci. Eng.* **4**, 432–445 (2018).
180. Mullen, L. *et al.* Development of ‘Redox Arrays’ for identifying novel glutathionylated proteins in the secretome. *Sci. Rep.* **5**, 1–14 (2015).
181. Checconi, P. *et al.* Redox proteomics of the inflammatory secretome identifies a common set of redoxins and other glutathionylated proteins released in inflammation, influenza virus infection and oxidative stress. *PLoS ONE* **10**, 1–21 (2015).
182. Zhang, X. *et al.* Positive Regulation of Interleukin-1 β Bioactivity by Physiological ROS-Mediated Cysteine S-Glutathionylation. *Cell Rep.* **20**, 224–235 (2017).
183. Klotzsch, E. *et al.* Fibronectin forms the most extensible biological fibers displaying switchable force-exposed cryptic binding sites. *Proc. Natl. Acad. Sci. U. S. A.* **106**, 18267–18272 (2009).
184. Krammer, A., Lu, H., Isralewitz, B., Schulten, K. & Vogel, V. Forced unfolding of the fibronectin type III module reveals a tensile molecular recognition switch. *Biophysics* **96**, 1351–1356 (1999).
185. Vogel, V. Unraveling the Mechanobiology of Extracellular Matrix. *Annu. Rev. Physiol.* **80**, 353–387 (2018).
186. Hynes, R. O. The extracellular matrix: Not just pretty fibrils. *Science* vol. 326 1216–1219 (2009).
187. Singh, P., Carraher, C. & Schwarzbauer, J. E. Assembly of Fibronectin Extracellular Matrix. *Annu. Rev. Cell Dev. Biol.* **26**, 397–419 (2010).
188. Brown, A. C., Dysart, M. M., Clarke, K. C., Stabenfeldt, S. E. & Barker, T. H. Integrin $\alpha 3\beta 1$ binding to fibronectin is dependent on the ninth type III repeat. *J. Biol. Chem.* **290**, 25534–25547 (2015).
189. Li, S. *et al.* Hydrogels with precisely controlled integrin activation dictate vascular patterning and permeability. *Nat. Mater.* **16**, 953–961 (2017).

190. Brown, A. C., Fiore, V. F., Sulchek, T. A. & Barker, T. H. Physical and chemical microenvironmental cues orthogonally control the degree and duration of fibrosis-associated epithelial-to-mesenchymal transitions. *J. Pathol.* **229**, 25–35 (2013).
191. Fiore, V. F. *et al.* $\alpha v\beta 3$ Integrin drives fibroblast contraction and strain stiffening of soft provisional matrix during progressive fibrosis. *JCI Insight* **3**, 1–15 (2018).
192. Fiore, V. F. *et al.* Conformational coupling of integrin and Thy-1 regulates Fyn priming and fibroblast mechanotransduction. *J. Cell Biol.* **211**, 173–190 (2015).
193. Hu, K. *et al.* Suppression of the SLC7A11/glutathione axis causes synthetic lethality in KRAS-mutant lung adenocarcinoma. *J. Clin. Invest.* **130**, 1752–1766 (2020).
194. Korotkina, R. N. *et al.* Activity of glutathione-metabolizing and antioxidant enzymes in malignant and benign tumors of human lungs. *Bull. Exp. Biol. Med.* **133**, 606–608 (2002).
195. Korotkina, R. N. *et al.* Study of total lipid peroxidation and antioxidant activity in pulmonary and mediastinal malignant and benign tumor tissue. *Bull. Exp. Biol. Med.* **136**, 283–285 (2003).
196. Gamcsik, M. P., Kasibhatla, M. S., Teeter, S. D. & Colvin, O. M. Glutathione levels in human tumors. *Biomarkers* vol. 17 671–691 (2012).
197. Cantin, A. M., Larivée, P. & Begin, R. O. Extracellular Glutathione Suppresses Human Lung Fibroblast Proliferation. *Am. J. Respir. Cell Mol. Biol.* **3**, 79–85 (1990).
198. Beeh, K. M. *et al.* Glutathione deficiency of the lower respiratory tract in patients with idiopathic pulmonary fibrosis. *Eur. Respir. J.* **19**, 1119–1123 (2002).
199. Kliment, C. R. & Oury, T. D. Oxidative stress, extracellular matrix targets, and idiopathic pulmonary fibrosis. *Free Radical Biology and Medicine* vol. 49 707–717 (2010).
200. Cantin, A. M., Hubbard, R. C. & Crystal, R. G. Glutathione Deficiency in the Epithelial Lining Fluid of the Lower Respiratory Tract in Idiopathic Pulmonary Fibrosis. *Am. Rev. Respir. Dis.* **139**, 370–372 (1989).
201. Singh, S. Cytoprotective and regulatory functions of glutathione S-transferases in cancer cell proliferation and cell death. *Cancer Chemotherapy and Pharmacology* vol. 75 1–15 (2015).

202. McMillan, D. H. *et al.* Attenuation of lung fibrosis in mice with a clinically relevant inhibitor of glutathione-S-transferase π . *JCI Insight* **1**, 85717 (2016).
203. Stefanelli, V. L. *et al.* Citrullination of fibronectin alters integrin clustering and focal adhesion stability promoting stromal cell invasion. *Matrix Biol.* **82**, 86–104 (2019).
204. Keselowsky, B. G., Collard, D. M. & García, A. J. Surface chemistry modulates fibronectin conformation and directs integrin binding and specificity to control cell adhesion. *J. Biomed. Mater. Res. A* **66A**, 247–259 (2003).
205. Klotzsch, E. *et al.* Fibronectin forms the most extensible biological fibers displaying switchable force-exposed cryptic binding sites. *Proc. Natl. Acad. Sci.* **106**, 18267–18272 (2009).
206. Li, C. X. *et al.* MicroRNA-21 preserves the fibrotic mechanical memory of mesenchymal stem cells. *Nat. Mater.* **16**, 379–389 (2017).
207. Day, E. K., Zhong, Q., Purow, B. & Lazzara, M. J. Data-Driven Computational Modeling Identifies Determinants of Glioblastoma Response to SHP2 Inhibition. *Cancer Res.* **81**, 2056–2070 (2021).
208. Friedensohn, S. *et al.* Convergent selection in antibody repertoires is revealed by deep learning. *bioRxiv* 2020.02.25.965673 (2020) doi:10.1101/2020.02.25.965673.
209. Mason, D. M. *et al.* Optimization of therapeutic antibodies by predicting antigen specificity from antibody sequence via deep learning. *Nat. Biomed. Eng.* 1–13 (2021) doi:10.1038/s41551-021-00699-9.
210. Tiwari, P. M. *et al.* Engineered mRNA-expressed antibodies prevent respiratory syncytial virus infection. *Nat. Commun.* **9**, 3999 (2018).
211. Kormann, M. S. D. *et al.* Expression of therapeutic proteins after delivery of chemically modified mRNA in mice. *Nat. Biotechnol.* **29**, 154–157 (2011).
212. Mahiny, A. J. *et al.* In vivo genome editing using nuclease-encoding mRNA corrects SP-B deficiency. *Nat. Biotechnol.* **33**, 584–586 (2015).
213. Mays, L. E. *et al.* Modified *Foxp3* mRNA protects against asthma through an IL-10-dependent mechanism. *J. Clin. Invest.* **123**, 1216–1228 (2013).

214. Probst, J. *et al.* Spontaneous cellular uptake of exogenous messenger RNA *in vivo* is nucleic acid-specific, saturable and ion dependent. *Gene Ther.* **14**, 1175–1180 (2007).
215. Tan, C. *et al.* Soluble Thy-1 reverses lung fibrosis via its integrin-binding motif. *JCI Insight* **4**,.